

**CHARACTERIZATION OF CARBON NANOTUBES AND NANOWIRES
AND THEIR APPLICATIONS**

by

KI CHUL KIM

B.S., YEUNGNAM UNIVERSITY, KOREA, 1999

M.S., UNIVERSITY OF COLORADO AT BOULDER, 2009

A thesis submitted to the

Faculty of the Graduate School of the
University of Colorado in partial fulfillment
of the requirements for the degree of

Doctor of Philosophy

Department of Electrical, Computer, and Energy Engineering

2011

This thesis entitled:
Characterization of Carbon Nanotubes and Nanowires and Their Applications
written by Ki Chul Kim
has been approved for the
Department of Electrical, Computer, and Energy Engineering

Prof. Dejan S. Filipovic

Dr. Thomas M. Wallis

Date _____

The final copy of this thesis has been examined by the signatories, and we find that both
the content and the form meet acceptable presentation standards of scholarly work in
the above-mentioned discipline.

Ki Chul Kim (Ph.D., Electrical Engineering)

Characterization of Carbon Nanotubes and Nanowires and Their Applications

Thesis directed by Associate Professor Dejan S. Filipovic

This thesis establishes comprehensive methodology for characterization of metallic nanowires (NWs) and carbon nanotubes (CNTs), and evaluation of their performance for interconnect applications at microwave/ mm-wave/THz frequencies. The research focus is on the development of modeling and measurement methods to determine constitutive material parameters, i.e. conductivity, and contact resistance of platinum (Pt) NWs, as well as on the development of modeling approaches to evaluate characteristic parameters for antennas, nano-coaxial lines, and single wire transmission lines composed of CNTs. Applicability of traditional two-port measurements is investigated for accurate determination of material parameters for Pt NWs over a broad frequency range. Two test-setups are developed. First, several configurations with directly contacted Pt NWs to a host coplanar waveguide (CPW) structure are designed and realized to determine the conductivity and contact resistance. Full-wave finite element and circuit models are used to determine the two parameters by fitting simulations to measurements. It is found that the single measurement setup with direct contacts cannot determine the two parameters simultaneously. To solve this problem, two approaches based on transmission line and lumped element models for Pt NWs are developed. Both approaches employ a set of two NWs with different lengths. The feasibility of both approaches is thoroughly studied and relevant conclusions are made.

An approach based on lumped element models is validated experimentally, and it is shown that the contact resistance and conductivity of 300 nm diameter Pt NWs are about 50Ω and $0.013\sigma_{bulk}$, respectively. In the second setup, the capacitive coupling contact between the Pt NWs and the CPW structure is exploited to determine the NW's conductivity. Two variations of this setup, specifically in-slot and on-dielectric configurations, are developed. Full-wave finite-element models are utilized to demonstrate suitability of the two configurations and to determine the conductivity of Pt NWs by fitting to measurements. Structural and elemental analyses of fabricated devices are conducted to assess fabrication and measurement issues.

Full-wave modeling for individual CNTs and CNT bundles is performed by the use of method of moments and finite element method codes in order to CNTs as antennas, nano-coaxial lines, and single wire transmission lines. Characteristic parameters, such as impedance, gain, efficiency, and line loss for each interconnect are evaluated and compared to those of their copper-based counterparts. Results show better performance of CNTs over conventional metals at microwave frequencies. The extension of modeling and metrology for semiconducting NWs and CNTs, and the study of graphene at microwave frequencies are proposed as directions for future work.

DEDICATION

to my father Jeonhwan Kim who passed away two years ago

ACKNOWLEDGEMENTS

I am grateful to my academic advisor, Prof. Dejan S. Filipovic, for his support and guidance throughout my Ph.D. program. He provided me with lots of opportunities for a variety of research topics which include carbon nanotubes, nanowires, microwave applications of nanotechnology, broadband spiral antennas, patch antennas, broadband filters, waveguides, and modeling methods for numerical analysis. Particularly, I am deeply thankful for his understanding and concerns over my father's disease and death during the third and forth years of my studies. I also thank him for introducing me to Dr. Pavel Kabos who has been my supervisor at NIST-Boulder for about two and half years. I have learned many things in metrology from him. I would also like to thank Prof. Edward Kuester, Prof. Zoya Popovic, Prof. Yung-Cheng Lee, and Dr. T. Mitch Wallis for serving as my thesis committee members.

This work has been partly supported by DARPA (Defense Advanced Research Projects Agency) Center on Nanoscale Science and Technology for Integrated Micro/Nano-Electromechanical Transducers (iMINT) funded by DARPA N/NEMS S&T Fundamentals Program (HR0011-06-1-0048) of which the program manager is Dr. D. L. Polla. I would like to thank the iMINT sponsors their interests on this research. I am also very thankful to Dr. Dazhen Gu who is with NIST-Boulder, Paul Rice who is with the ME department of CU-Boulder, Dr. Chin-Jen Chiang who used to work for Dr. Kabos and is now with the National Changhua University of Education, for fabrication of devices and discussions for this research. I would also like to thank Dr. Atif Imtiaz

and Dr. Sang-hyun Lim from NIST-Boulder for valuable discussions regarding this research.

I would also like to thank my colleagues and friends; Prof. Filipovic's group: Neil Kefauver, Joseph Mruk, Matthew Radway, Hongyu Zhou, Nathan Sutton, Mohamed Elmansouri, Rohit Sammeta; Prof. Filipovic's alumni: Dr. Yongjae Lee, Dr. Kenneth Vanhille, Dr. Michael Buck, Dr. Milan Lukic, Dr. Yuya Saito, Dr. James McDonanld, Arian Lalezari, Lars Grimsrud; Prof. Filipovic's visiting scholars: Prof. Bongsik Jeong of Dong-A University and Dr. Manseok Uhm of ETRI, Korea; Prof. Kuester's alumni: Dr. Sung Kim and Dr. Yao Wen Hsu; Prof. Popovic's students, and Dr. Sebastien Rondineau for their help and support.

I also appreciate the support of my brother and his wife, Kijoon and Kebang, and my sister, Kisoon. I would like to thank my old friends, Wongeun Lee and Kunwoo Park. I appreciate the encouragement of my old professors, Prof. Ki-Chai Kim, Prof. Taehong Yi, Prof. Youngsuk Seo, and Prof. Changhui Ahn of Yeungnam University, and my old middle school teacher Ms. Kyeongja Lee. Finally, my greatest thanks go to my parents, and aunt and her husband for their love and support.

TABLE OF CONTENTS

1. Introduction	1
1.1 Nanowires	5
1.2 Carbon Nanotubes.....	9
1.3 Dissertation Organization.....	16
2. Characterization of Platinum Nanowires (I) - Contact Impedance and Conductivity	19
2.1 Fabrication and Measurements.....	22
2.1.1 Coplanar Waveguides and Calibration Standards	22
2.1.2 Platinum Nanowire Deposition.....	24
2.1.3 Two-port Measurements.....	25
2.2 Modeling Methods and Validation	26
2.2.1 Finite Element Method.....	26
2.2.2 Circuit and Method of Moments Models	29
2.3 Fitting Methods	33
2.3.1 Initial Setup for the Full-Wave Models.....	33
2.3.2 Initial Setup for Circuit Models	36
2.3.3 Approaches	38

2.3.4 Results.....	39
2.4 Model-Based Methods	44
2.4.1 Approach Based on Transmission Line Models.....	45
2.4.1.1 Algorithm Description	45
2.4.1.2 Validation.....	52
2.4.2 Lumped Element Based Approach	55
2.4.2.1 Algorithm Description	55
2.4.2.2 Validation.....	59
2.4.3 Experimental Results.....	60
3. Characterization of Platinum Nanowires (II) – Contactless Approach.....	67
3.1 Modeling	69
3.1.1 Validation.....	70
3.1.2 Parametric Study.....	74
3.2 Prototypes	79
3.2.1 Fabrication and Measurements.....	80
3.2.2 In-slot Configuration Prototype.....	82
3.2.3 On-dielectric Configuration Prototype.....	85
3.3 Discussion	91
4. Characterization of Individual Carbon Nanotubes and Applications	93
4.1 Modeling Individual CNTs	95
4.1.1 Modeling Approaches and Validation.....	95
4.1.2 Evaluation Parameters	101

4.2 Interconnect Applications.....	102
4.2.1 Wireless Interconnect with CNT Antennas.....	102
4.2.2 Nano-Coaxial Lines	105
4.2.3 Single Wire Transmission Lines	108
4.3 Discussion	110
5. Characterization of Carbon Nanotube Bundles and Applications	113
5.1 Carbon Nanotube Bundle Modeling.....	115
5.2 Wireless Interconnects.....	117
5.2.1 Modeling Validation.....	118
5.2.2 CNT Bundle Monopole Antennas	118
5.3 Nano Coaxial Lines.....	126
5.3.1 Modeling Validation.....	126
5.3.2 Identical Bundle and Mixed Bundle	128
5.4 Single Wire Transmission Lines.....	133
6. Summary, Contributions, and Future Work	134
6.1 Characterization of Platinum Nanowires (I) – Contact Impedance and Conductivity	134
6.2 Characterization of Platinum Nanowires (II) – Contactless Approach	135
6.3 Characterization of Individual Carbon Nanotubes and Applications.....	136
6.4 Characterization of Carbon Nanotube Bundles and Applications.....	137
6.5 Original Contributions	138
6.6 Future Work	139

Bibliography	142
Appendix A: Additional Modeling Validations.....	153
A.1 ABCD Matrix Calculation.....	153
A.2 Method of Moments Modeling	156
Appendix B: Gap Capacitance in Circuit Models.....	159
B.1 Comparison Between Gap Capacitance and CPW Gap Component.....	159
B.2 Verification with Devices Having Pt NWs	161
Appendix C: Elemental Analysis Results	164
References	168

LIST OF TABLES

Table 1.1 Input impedances and efficiencies of solid cylindrical metal wires made from perfectly electric conductor and bulk Cu. The wire length is 0.47λ	2
Table 1.2 Overview of measured resistivities and contact resistances of various NWs.....	8
Table 1.3 Physical properties of CNTs from available literature [31, 32, 34].....	14
Table 2.1 Comparison between calculated and measured DC resistance. DC resistance of the NW is calculated from the formula, (DC resistance) = (wire length) / (conductivity \times cross sectional area). Comparisons are made with the solutions from the two approaches	44
Table 2.2 Measured lengths of Pt NWs with overlapping distance between the NW and CPW signal lines ignored	64
Table 2.3 Measured DC resistances including NW's resistance, two contact resistances, and resistance of CPW signal lines.....	66
Table 4.1 Characteristic impedance (Z_c) and line losses per μm of single wire CNT lines and Cu lines. Radius of the nanotubes is 2.712 nm.....	110
Table 5.1 Validation of MoM modeling for CNT bundle dipole antennas with results from [105]	119
Table 5.2 Performance comparison between CNT dipole, CNT monopoles, and Cu monopole.....	125
Table 5.3 Line loss per 200 nm of the coax with CNT bundle versus the number of CNTs at 30 GHz. The inner conductor attached to the bundle is assumed to be Cu.....	128
Table 5.4 Performance comparison between the coaxial lines with CNT bundles and solid Cu. The solution frequency is 30 GHz.....	130

Table 5.5 Performance of the coaxial line with the mixed CNT bundle. The solution frequency is 30 GHz.....	132
Table 5.6 Performance comparison between the Cu Goubau line and the CNT bundle Goubau line. The solution frequency is 30 GHz.....	133
Table C.1 Elemental analysis result for FIB SiO ₂ at 20 kV.....	165
Table C.2 Elemental analysis result for FIB SiO ₂ at 15 kV.....	166
Table C.3 Elemental analysis result for FIB SiO ₂ at 10 kV.....	167
Table C.4 Elemental analysis result for FIB SiO ₂ at 5 kV.....	168

LIST OF FIGURES

Fig. 1.1 SEM images of (a) an individual Pt NW deposited on Au electrodes, and (b) an array of Si NWs (SEM image from www.scienceprog.com)	5
Fig. 1.2 Examples of NW applications: (a) Si NW field effect transistor, (b) a Pt NW biosensor that enables monitoring of individual brain cells (image from http://www.nanotech-now.com/), (c) Pt-bonded electroless etched Si NW for thermoelectric devices, and (d) flexible artificial skin based on arrays of Ge/Si NWs.....	7
Fig. 1.3 Wideband and high frequency characterization of CNTs. (a) Two-port measurement setup for a single-walled CNT bundle, and measured S-parameters (circuit model in inset), and (b) measurement setup and SEM images for individual multi-walled CNT. The circuit model from (a) is used for the studies in (b).....	10
Fig. 1.4 Artistic representation of SWCNT and MWCNT. A SWCNT bundle is composed of many SWCNTs. Figure is reproduced from [27]	11
Fig. 1.5 Graphene sheet of SWCNTs. A SWCNT is formed by rolling up graphene along a chiral vector (composed of \mathbf{a}_1 and \mathbf{a}_2) to form a cylinder. Red lines are particular cases of the chiral vector for armchair and zigzag CNTs.....	11
Fig. 1.6 Example of three different CNT chiralities: zigzag (16, 0), chiral (12, 4), and armchair (8,8). Each CNT starts rolling at a different slope (image from www.flickr.com/photos/l2xy2/).....	13
Fig. 2.1 Schematic of a CPW-based measurement setup.....	23
Fig. 2.2 Chip layout of two different ground configurations for modeling validation	23
Fig. 2.3 SEM photographs of devices under test: (a) empty device, (b) device with 100 nm diameter Pt NW, and (c) device with 250 nm diameter Pt NW	25
Fig. 2.4 Simulated and measured S-parameters without (a) and with (b) Au short. SEM pictures of the devices are shown as insets	28

Fig. 2.5 Power analysis of the CPW devices with 2 μm -wide Au short. The first 5 higher order modes and the fundamental mode are included in both ground configurations. $M_{\alpha\beta}$ represents a mode of which α is the port number and β is the mode number. Pgnd is the loss power from ground layers, Pau_in is from CPW signal lines of Au layers, and Pt _i _in is from CPW signal lines of Ti layers. Prad is the radiated power.....	30
Fig. 2.6 AWR circuit model for the empty device under test	31
Fig. 2.7 Simulated and measured S-parameters for (a) the empty device, and (b) the device with Au short of 2 μm . Simulations are conducted from AWR MoM and circuit models, and ANSYS Designer circuit model	32
Fig. 2.8 Initial FEM modeling setup for the device with an individual Pt NW of a 250 nm diameter. The NW is placed in the middle of the CPW structure, and directly contacted to CPW signal lines. The SiO ₂ dielectric layer supports the NW in the gap of CPW signal lines. The associated SEM image of the NW is shown at bottom right side	34
Fig. 2.9 Simulated and measured S-parameters for devices with Pt NW of 250 nm diameter. Contact resistance is assumed to be 0 Ω for simulations. Conductivity of Pt NW varies from σ_{bulk} to $0.05\sigma_{\text{bulk}}$. Reducing the conductivity results in less difference between simulations and measurements	35
Fig. 2.10 Modeling setup for validation of the lumped impedance boundary condition from full-wave FEM models, and their computed results. Resistance is assumed to be 315 Ω	37
Fig. 2.11 Schematic of AWR model for the device with a Pt NW under test. Sections of CPW and taper are modeled with MoM, while the gap and the NW are modeled with circuit elements.....	37
Fig. 2.12 Flow chart for the analysis approaches used to determine the interdependence between contact resistance and NW conductivity	39
Fig. 2.13 Measured and simulated S-parameters for the devices with Pt NWs. full-wave FEM modeling is used for the simulations. Insets: SEM images of measured device with Pt NW	41
Fig. 2.14 Measured and simulated S-parameters for the devices with Pt NWs. Circuit modeling is used for the simulations. Insets: SEM images of measured devices with Pt NW	42

Fig. 2.15 Ranges for the conductivity of Pt NWs and the contact resistance. With one of the two parameters fix, the other can be obtained. Literature A: [19], Literature B: [6], Literature C: [20]	44
Fig. 2.16 SEM image of Pt NW and its equivalent model based on transmission line theory. The NW is modeled with a transmission line having characteristic impedance Z_c and propagation constant γ . Contact resistance, R_c , is connected at both ends of the NW	46
Fig. 2.17 Theoretical current distribution in a solid round wire, reproduced from [79]. J : current density in a wire, J_s : surface current density, r : radius within the wire, r_0 : outer radius of the wire, and δ : skin depth. Note that, when $\sqrt{2} r_0 / \delta = 0.1$, current distribution is uniform throughout the cross section of the wire	52
Fig. 2.18 Computed R_c and σ from the transmission line model-based approach and (a) circuit and (b) full-wave FEM simulations. Preset contact resistance and conductivity are $R_c = 100 \Omega$ and $\sigma = 9.3 \times 10^5 \text{ S/m}$, respectively	54
Fig. 2.19 Simulated electric field distribution around Pt NW using HFSS. The gap distance is $4 \mu\text{m}$. Note that the field distribution is not that of a TEM mode in the gap	55
Fig. 2.20 SEM image of Pt NW and equivalent two-port T-network for Pt NWs with length l_1 . Series impedances Z_{11} and Z_{12} represent impedance of the Pt NW. Shunt impedance Z_{13} is impedance between the Pt NW and ground	56
Fig. 2.21 Circuit model representing lumped element-based approach for the device with Pt NW. The Pt NW is modeled as a round wire component from the AWR library	59
Fig. 2.22 Computed R_c and σ from the lumped element-based algorithm using (a) circuit and (b) full-wave FEM models. Preset contact resistance and conductivity are $R_c = 100 \Omega$ and $\sigma = 9.3 \times 10^5 \text{ S/m}$, respectively	61
Fig. 2.23 Chip layout for measurements of Pt NWs with different lengths	62
Fig. 2.24 Measured mean values and standard deviations for R_c and σ of Au short devices. Values are obtained using lumped element-based algorithm. Total of 36 different sets of the devices are used to obtain these statistics	63
Fig. 2.25 SEM images of Pt NWs embedded in the 4 and 8 μm gaps of devices	64

Fig. 2.26 Measured mean values and standard deviations for R_c and σ of 300 nm diameter Pt NWs. Values are obtained using lumped element-based algorithm. Total of 100 different sets of the devices are used to obtain these statistics	65
Fig. 3.1 CPW device with individual Pt NWs and details for the two considered approaches. Top right is the in-slot configuration, and bottom right is the on-dielectric configuration	70
Fig. 3.2 SEM for fabricated devices of the in-slot configuration with a Au line in the slot. (b) is zoomed-in square in (a). (c) and (d) are zoomed-in square in (b).....	72
Fig. 3.3 Measured and simulated S-parameters for the devices using an in-slot configuration for modeling validation. The Au line width and the slot width for device A (a) are 1.35 μm and 146 nm, and those for device B (b) are 1.68 μm and 83 nm, respectively	73
Fig. 3.4 Pt NW of the in-slot and on-dielectric configurations, and their related parameters.....	74
Fig. 3.5 Simulated S-parameters for parametric studies with dielectric thickness t_{Die} varied from 1 nm to 20 nm. L_{gap} is 4 μm and L_{cont} is 20 μm . The frequency is 40 GHz.....	76
Fig. 3.6 Simulated S-parameters for parametric studies with gap distance, L_{gap} . t_{Die} is 10 nm and L_{cont} is 20 μm . The frequency is 40 GHz.....	76
Fig. 3.7 Simulated S-parameters for parametric studies with contact length L_{cont} . t_{Die} is 10 nm and L_{gap} is 4 μm . The frequency is 40 GHz	77
Fig. 3.8 Simulated S-parameters for in-slot configurations with three different conductivities of σ_{bulk} , $0.1\sigma_{bulk}$, and $0.014\sigma_{bulk}$	78
Fig. 3.9 Simulated S-parameters for on-dielectric configurations with three different conductivities of σ_{bulk} , $0.1\sigma_{bulk}$, and $0.014\sigma_{bulk}$	79
Fig. 3.10 SEM of fabricated prototypes with Pt NWs. (a) In-slot configuration, (b) on-dielectric configuration with thick SiO_2 , and (c) on-dielectric configuration with thin SiO_2	82
Fig. 3.11 SEM of fabricated prototypes of the in-slot configuration. (a) Pt NW in slot, (b) detailed slot and Pt NW, and their dimensions. The NW width is estimated at about 177 nm. The slot is asymmetric with respect to the NW	83

Fig. 3.12 Measured magnitude of S-parameters for the prototype with an in-slot configuration.....	84
Fig. 3.13 SEM of the two ends of the Pt NW in the prototype with an in-slot configuration. It seems that there are short connections between the Pt NW and the signal lines at both ends. Because the contact points are very small, DC resistance is measured at about $1.72\text{ k}\Omega$	85
Fig. 3.14 Measured S-parameters for two prototypes of the on-dielectric configuration	86
Fig. 3.15 SEM of destructive analysis for prototypes of the on-dielectric configuration. One end of the Pt NW and SiO_2 layer is cross-sectional cut to estimate dimensions. Dimensions of the Pt NW and the thickness of the SiO_2 dielectric are measured from these cross-sectional images	88
Fig. 3.16 Measured and simulated S-parameters for the prototype of the on-dielectric configuration of thick SiO_2 . FEM modeling fits are conducted with effective dielectric constant $\epsilon_{r,\text{eff}}$ and conductivity σ . The best fit is of $\epsilon_{r,\text{eff}} = 12$ and of $\sigma = 0.014\sigma_{\text{bulk}}$	89
Fig. 4.1 Modeling approach and three step validation flow chart. The paper referred in the chart is reference [8]	98
Fig. 4.2 Computed input impedances from MoM models and comparison with literature [8]. (a) Wire model of a Cu dipole, and (b) surface model of a CNT dipole	99
Fig. 4.3 Computed characteristic impedances from the FEM and MoM models of the nano-coaxial line having a CNT inner conductor. For x-axis, the radius of inner conductor is fixed but the inner radius of the outer conductor varies to give an impedance $Z_{c,\text{conv}}$ from the conventional formula (4.5)	100
Fig. 4.4 Modeling setup used to evaluate wireless interconnecting scheme.....	103
Fig. 4.5 Computed reflection coefficients of CNT-PEC dipole antennas used in studied wireless interconnects. Port 1 (S_{11}) is the CNT dipole and port 2 (S_{22}) is the PEC dipole	104
Fig. 4.6 Computed transmissions (S_{21}) for three cases: the CNT-CNT dipole pair separated by $1\text{ }\mu\text{m}$ and $100\text{ }\mu\text{m}$, and the CNT-PEC dipole pair separated by $100\text{ }\mu\text{m}$..	105
Fig. 4.7 Cross section of ALD CNT coated with Al_2O_3 and tungsten (W) (a), and its computational model (b).....	106

Fig. 4.8 Effect of dielectric loading on (a) the characteristic impedance and (b) the attenuation constant of CNT coaxial lines, and performance comparison between CNT and Cu at 25 GHz.....	107
Fig. 4.9 Characteristic impedance and attenuation constant of coaxial lines with a CNT or Cu nanotube inner conductor at 25 GHz. The radius of both CNT and Cu nanotube is fixed at 2.712 nm or 10 nm. Note that the impedance and attenuation constant for the two radii of CNTs are the same	108
Fig. 4.10 Validation of FEM modeling for Sommerfeld lines with results in literature [92]	109
Fig. 4.11 Computed transmission for studied interconnect schemes: wireless interconnects with CNT dipole antennas, single wire CNT lines, and CNT coaxial lines	112
Fig. 5.1 Lattice constant of a CNT bundle, $D_{\text{CNT}} + 0.34 \text{ nm}$. R_{cnt} is CNT's radius.....	116
Fig. 5.2 Top view of various CNT bundle dipoles of (a) 7 CNTs, (b) 19 CNTs, and (c) 55 CNTs	119
Fig. 5.3 CNT bundle monopoles of (a) two CNTs and (b) four CNTs over a ground plane. R_{CNT} is the radius of the CNTs. The CNTs are connected at their base by a PEC wire..	120
Fig. 5.4 Simulated input impedance of two-CNT monopoles shown in Fig. 5.3 (a) for different separations: $D = 3R_{\text{CNT}}$, $10R_{\text{CNT}}$, and $50R_{\text{CNT}}$. The radius of the CNTs, R_{CNT} , is 2.712 nm, and their length is 10 μm at which a single CNT monopole resonates at 160 GHz	120
Fig. 5.5 Various CNT bundle monopole configurations with 7 CNTs. (a) Dense bundle with $D = D_{\text{CNT}} + 0.34 \text{ nm}$, (b) sparse bundle with $D = 10(D_{\text{CNT}} + 0.34 \text{ nm})$, (c) cone-shaped A with $D_{\text{Bottom}} = D_{\text{CNT}} + 0.34 \text{ nm}$ $D_{\text{CNT}} + 0.34 \text{ nm}$ and $D_{\text{Top}} = 10(D_{\text{CNT}} + 0.34 \text{ nm})$, and (d) cone-shaped B with $D_{\text{Bottom}} = 10(D_{\text{CNT}} + 0.34 \text{ nm})$ and $D_{\text{Top}} = D_{\text{CNT}} + 0.34 \text{ nm}$..	122
Fig. 5.6 Simulated input impedance of various shaped monopoles with 7 CNTs shown in Fig. 5.5	122
Fig. 5.7 Simulated input impedance of CNT bundle monopoles with (a) two CNTs and (b) four CNTs shown in Fig. 5.3.....	124
Fig. 5.8 Top view of two CNT bundle monopoles with (a) 61 and (b) 85 CNTs	124

Fig. 5.9 Isometric view (left) and side view (right) of a nano-coaxial line with a CNT bundle as the center section of the inner conductor. Twelve CNTs are used in this setup to connect the two disjoint solid parts	127
Fig. 5.10 Validation of FEM models for nano-coaxial lines with CNT bundles with different numbers of CNTs. The outer conductor is assumed to be PEC.....	128
Fig. 5.11 Nano-coaxial line with a CNT bundle and solid Cu as the inner conductor (left), and the arrangement of CNTs in the bundle (right). The bundle is composed of 61 identical CNTs of 2.712 nm radius. The radius of the Cu inner conductor is 26 nm. CNTs are densely packed, therefore 61 CNTs are the maximum within the given cross-section of Cu.....	129
Fig. 5.12 Top view of nano-coaxial line with the CNT bundle and solid Cu as the inner conductor (left), and the arrangement of CNTs in the bundle (right). The bundle is mixed with 37 larger CNTs of 2.712 nm radius and 96 smaller CNTs of 0.687 nm radius. The radius of the Cu inner conductor is 26 nm	131
Fig. 5.13 Cross-sections of the three CNT bundles.....	132
Fig. 5.14 Goubau line with a 61-CNT bundle and 10 nm-thick Al_2O_3 coating.....	133
Fig. A.1 CPW line with Pt NW and PEC wire as its signal line. Characteristic impedance and propagation constant of the section b can be obtained from the S-parameters of a , a' , and W using ABCD matrix calculation.....	154
Fig. A.2 Comparison between results from ABCD matrix calculation (ABCD in the legend) and direct FEM modeling (FEM in the legend). (a) characteristic impedance, Z_c and (b) propagation constant, γ	155
Fig. A.3 Five geometries evaluated for modeling of a tapered CPW. (a) model #1 with a 25 μm line at port 2, (b) model #2 with a 325 μm line at port 2, (c) model #3 with a 25 μm line at both ports, (d) model #4 with a 25 μm line at port 2, and (e) model #5 with a 25 μm line at both ports. A line width is the same as the width of either end of the taper	156
Fig. A.4 CPW structure with two back-to-back tapered CPW lines.....	157
Fig. A.5 Comparison between simulated S-parameters of the CPW configuration in Fig. A.4 (Back-to-Back) and the CPW configurations where the back-to-back CPW lines are replaced by the geometries from in Fig. A.3	158

Fig. B.1 Circuit modes for empty devices (neither NW nor Au-bridge).....	160
Fig. B.2 Measured and simulated S-parameters for empty devices. The devices are modeled with CPW gap component (CPW Gap in legend) and gap capacitance of 0.6 fF (Cgap = 0.6 fF in legend)	161
Fig. B.3 Circuit models for the device with 100 nm diameter Pt NWs	162
Fig. B.4 Measured and simulated S-parameters for the device with 100 nm diameter Pt NWs. The model without the gap capacitance (wo/ Cgap in legend) and that with the gap capacitance (w/ Cgap in legend) shown in Fig. B.3. are compared to verify effects of the gap capacitance for high impedance devices	163
Fig. C.1 Elemental analysis spectrum for FIB SiO ₂ at 20 kV	165
Fig. C.2 Elemental analysis spectrum for FIB SiO ₂ at 15 kV	166
Fig. C.3 Elemental analysis spectrum for FIB SiO ₂ at 10 kV	167
Fig. C.4 Elemental analysis spectrum for FIB SiO ₂ at 5 kV	168

CHAPTER 1

INTRODUCTION

The demands for small electronic devices with many integrated functionalities are growing at a rapid pace. This requires smaller feature sizes and advanced manufacturing technologies for denser integrated circuits and nanoscale systems. However, reducing an interconnect feature size into the nanometer scale leads to the variation of current behavior in metallic wires [1] and causes several issues from an electrical point of view. First, material properties, particularly the conductivity of metals, change from their bulk properties due to the decreased mean free path of conduction electrons [2, 3]. Recent research on Cu nanowires (NWs) shows that the resistivity of the 50 nm-wide NW increases about 1.6 times compared to the bulk value [4]. Thus, the conductivity of metals at this small scale needs to be determined in order to design various components and ICs. Chapters 2 and 3 of this thesis further discuss this issue with emphasis on Pt NWs.

Second, a contact impedance between the nanometer size component and macroscopic world has to be measured and analyzed because its value is not negligible at nanoscale. It is reported that the contact resistance is dependent on the size of NWs

[5] and fabrication conditions [6]. The modeling and metrology of nanometer scale Pt NWs deposited on Au electrodes is discussed in Chapter 2.

Third, conduction loss in nanometer scale metals increases significantly because of the increased resistivity. As reported in [7], resistivity of 60 nm-wide Cu NWs is about ten times their bulk resistivity. This causes a temperature increase on the lines with potential for lines to break and lower efficiency for nanoscale antennas. As an example, Table 1.1 compares the input impedance and efficiency of solid cylindrical metal wires with length of 0.47λ and different radii [8]. Perfectly conducting and solid Cu conductivities are used in the models. For the solid Cu wire of 2 nm and 20 nm radii, the antenna's first resonance disappears and efficiency is very low. When the radius is smaller than several tens of nm, quantum effects need to be included. At this scale, finding new materials which work better than conventional metals is necessary. Carbon nanotubes (CNTs) are known to have higher conductivity than other metals when the feature size is on the nanometer scale. Thus CNTs are seriously considered for nanoscale components. CNTs are discussed in Chapters 4 and 5.

Table 1.1 Input impedances and efficiencies of solid cylindrical metal wires made from perfectly electric conductor and bulk Cu [8]. The wire length is 0.47λ .

Radius	Material	Input Impedance (Ω)	$e_r = P_r / P_{in}$
$3.75 \mu\text{m}$	Perfectly conducting	$69.84 - j7.36$	1.00
	Bulk	$69.84 - j7.36$	0.97
20 nm	Perfectly conducting	$62.78 - j76.96$	1.00
	Bulk	$1,960.13 - j1,917.14$	5.53×10^{-3}
2 nm	Perfectly conducting	$62.08 - j106.85$	1.00
	Bulk	$19,788.96 - j19,539.85$	4.82×10^{-6}

Lastly, nanoscale fabrication, measurement, and modeling accuracy are difficult and repeatability thereof is a big concern. Rice *et al.* provide good examples of this issue in [9] where a 100 nm-diameter multi-walled CNT is welded on a coplanar waveguide (CPW) structure and Y-parameters are measured up to 25 GHz. They observed huge difference in measurements when the room light was ‘on’ and ‘off’. The difference was reduced with more careful welding, however, Y_{11} and Y_{22} were still unequal. Accurate modeling of nanometer scale devices is impossible if the material properties are not properly found. Additionally, as mentioned earlier, effects of contact impedance and quantum physics have to be included in modeling. This issue is covered in Chapters 2 through 5.

This thesis establishes comprehensive methodology for characterization of metallic NWs and CNTs, and evaluation of their performance for interconnect applications at microwave/mm-wave/THz frequencies. The research focus is on the development of modeling and measurement methods to determine constitutive material parameters, conductivity, and contact resistance of Pt NWs, and on the development of modeling approaches to evaluate characteristic parameters for antennas, nano-coaxial lines, and single wire transmission lines composed of CNTs. Applicability of traditional two-port measurements is investigated for accurate determination of material parameters for Pt NWs over a broad frequency range. Two test-setups are developed. First, configurations with directly contacted Pt NWs to a host CPW structure are developed to determine both the conductivity and the contact resistance. Full-wave finite-element and circuit models are utilized to determine the two parameters by fitting

simulations with measurements. It is found that the single measurement setup with direct contacts cannot determine the two parameters simultaneously. To solve this problem, two approaches based on transmission line and lumped element models for Pt NWs are developed. Both approaches employ a set of two NWs with different lengths. The feasibility of both approaches is thoroughly studied and relevant conclusions are made. An approach based on the lumped element models is validated experimentally, and it is shown that the contact resistance and conductivity of 300 nm diameter Pt NWs are about 50Ω and $0.013\sigma_{bulk}$, respectively. In the second setup, the capacitive coupling contact between the Pt NWs and the CPW structure is exploited to determine the NW's conductivity. Two variations of this setup, specifically in-slot and on-dielectric configurations, are developed. Full-wave finite-element models are utilized to demonstrate suitability of the two configurations and to determine the conductivity of Pt NWs by fitting with measurement. Structural and elemental analysis for fabricated devices are conducted to assess fabrication and measurement issues.

Full-wave modeling for individual CNTs and CNT bundles is performed by the use of method of moments (MoM) and finite element method (FEM) codes when simulating CNTs as antennas, nano-coaxial lines, and single wire transmission lines. Characteristic parameters, such as impedance, gain, efficiency, and line loss, for each interconnect are evaluated and compared to those of their Cu-based counterparts. Results show better performance of CNTs over conventional metals at microwave frequencies. The extension of modeling and metrology for semiconducting NWs and

CNTs, and the study of graphene at microwave frequencies are proposed as directions for future work.

1.1. Nanowires

Nanowires are structures with diameter or thickness on a nanometer scale. Many types of NWs have been demonstrated so far. Their electrical properties depend mainly on a baseline material, i.e. they are metallic (e.g. Au, Cu, Ni, Pt, etc.), semiconducting (e.g. GaN, InP, Si, etc.), or insulating (e.g. SiO₂, TiO₂). Fig. 1.1 shows scanning electron microscope (SEM) images of NW examples: (a) an individual Pt NW deposited on a Au line, and (b) an array of silicon NWs.

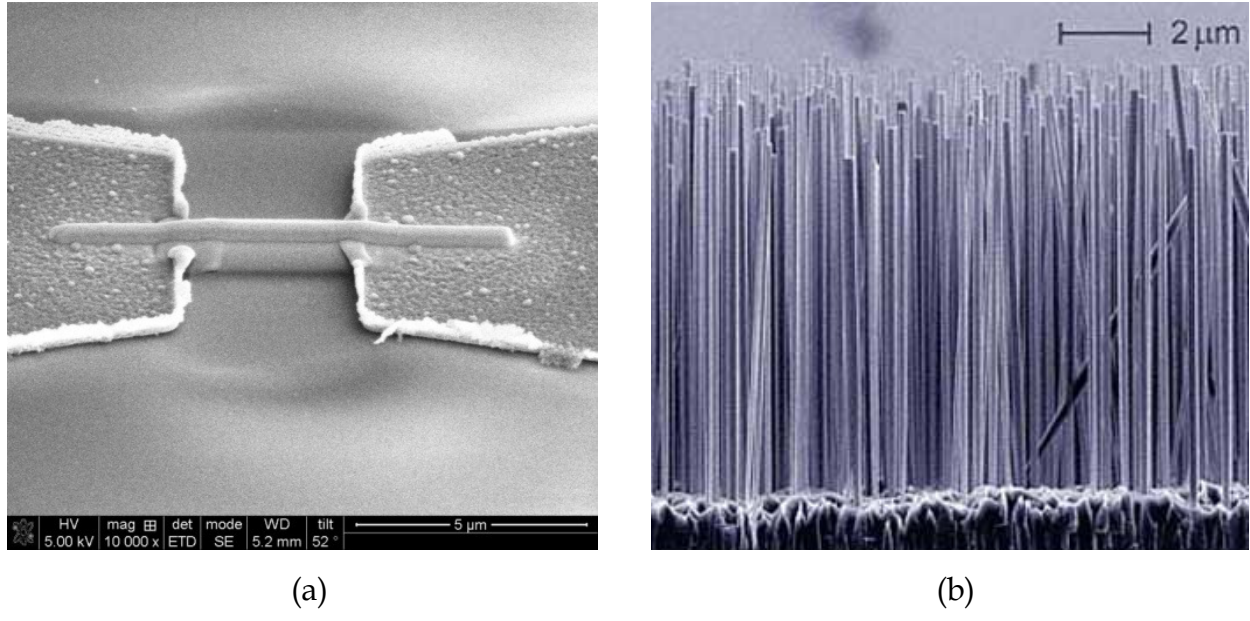


Fig. 1.1 SEM images of (a) an individual Pt NW deposited on Au electrodes [10], and (b) an array of Si NWs (SEM image from www.scienceprog.com).

NWs are considered a fundamental building block for current and future nanoscale and microscale systems, and their potential application range is very broad. For example, the use for electrochemical sensors and biosensors, and packaging for nano-electronics are summarized in [11] and [12], respectively. Cu NWs are proposed to be used for low-cost flexible displays, light emitting diodes, and thin film solar cells [13]. Other examples of NW applications are illustrated in Fig. 1.2: (a) Si NW field effect transistors (FETs) developed by NIST scientists [14], (b) biosensors using Pt NWs guided by blood vessels as conduits, allowing monitoring of individual brain cells [15], (c) Pt-bonded electroless etching Si NW for thermoelectric devices [16], and (d) flexible artificial skin based on arrays of Ge/Si NWs [17].

At the nanoscale, quantum mechanical effects are reinforced as the size of the NW shrinks from hundreds of nanometers to an atomic level, and material properties of metals are different than those of their macroscopic counterparts. Research for determining electrical conductivity of thin metallic films or wires at the nanoscale has been carried out since the 1930's [2] and 1940's [3]. Decrease of the metal conductivity was associated with the reduced mean free path of the conduction electrons due to scattering from surface boundaries of the thin metals. Later, it was found that the conductivity of very thin metals is decreased by not only scattering from surface boundaries, phonons, and defects, but also due to scattering from grain boundaries [18]. Recently, direct current (DC) or low frequency experimental results for the conductivity of Au, Cu, and Pt NWs have been reported. It is interesting that the consistent or same results between different research groups are difficult to obtain. This is a testament that

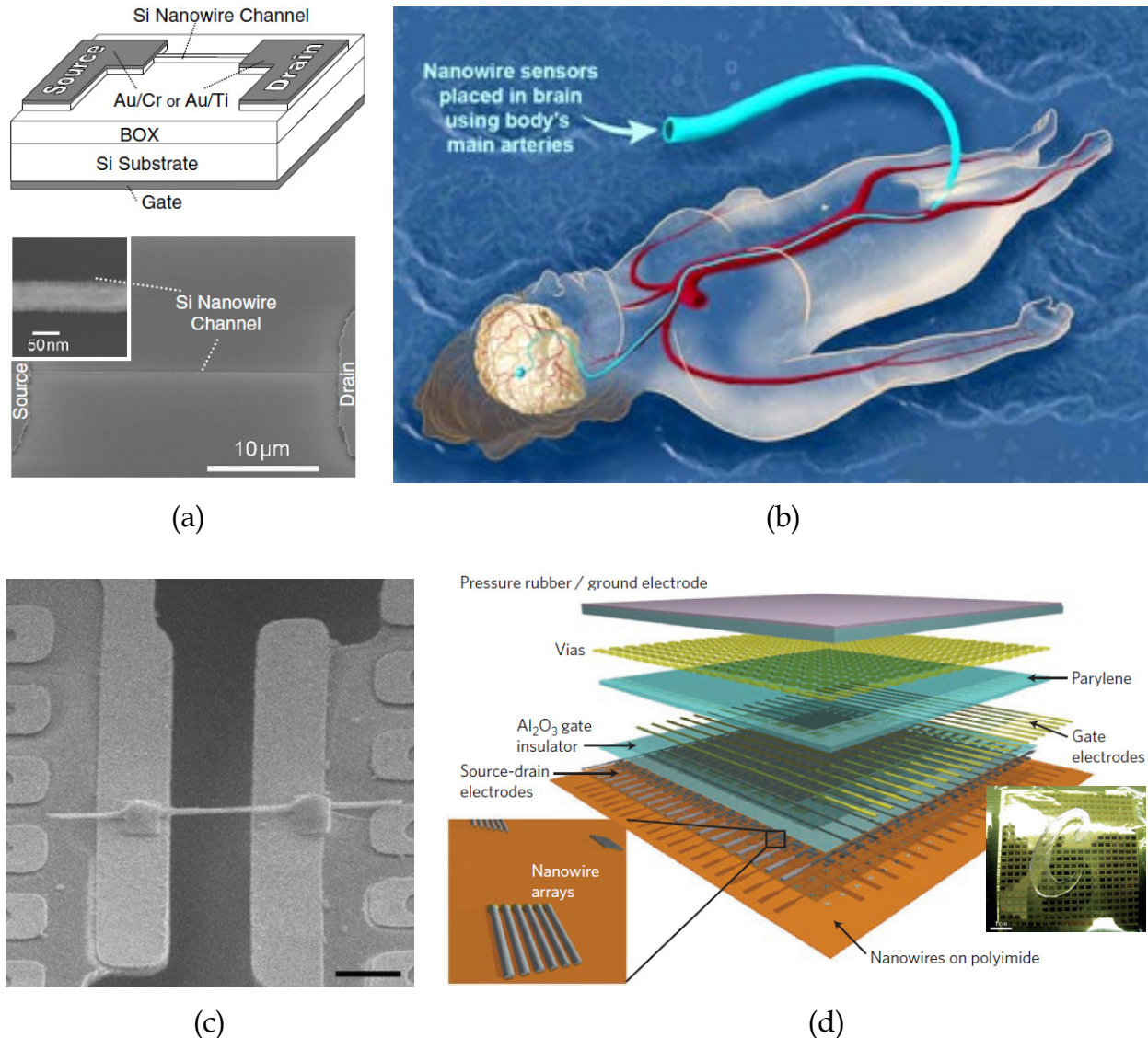


Fig. 1.2 Examples of NW applications: (a) Si NW field effect transistor [14], (b) a Pt NW biosensor that enables monitoring of individual brain cells (image from <http://www.nanotech-now.com/>), (c) Pt-bonded electroless etched Si NW for thermo-electric devices [16], and (d) flexible artificial skin based on arrays of Ge/Si NWs [17].

the field is still in infancy. For example, the resistivity of 50 nm-wide Cu NWs is measured to be 1.6 times the bulk resistivity in [4], while the resistivity of a 60 nm width is reported to be about ten times the bulk in [7]. Moreover, literature [6, 19, 20] reports that Pt NWs with a width of 60-360 nm have a conductivity of about 3 to 285 times

lower than their bulk conductivity. The above discussed results and 70 nm-wide Au NW measurements [21] are summarized in Table 1.2. The measured/estimated contact resistances for Pt NWs are also included. As seen, determining contact resistance between the NW and host structures is another issue. The contact resistance of 70 nm Pt NWs deposited on Au electrodes is 138 Ω [6], while that of 80-150 nm diameter Pt NWs attached to Pt electrodes is 700-800 kΩ [22]. All these results were obtained by DC or low frequency measurements, and values for apparently similar configurations vary significantly.

Table 1.2 Overview of measured resistivities and contact resistances of various NWs

Material	Literature	Diameter (nm)	Resistivity ($\mu\Omega$ cm)	Contact Resistance
Au	[21]	70	4.5 (bulk: 2.5)	N/A
Cu	[4]	50	3.25 (bulk: 1.7)	N/A
	[7]	60	17.1	N/A
Pt	[6]	70 ± 5	33 ± 5 (bulk: 10.8)	138 Ω
	[19]	60	61.5 (5.9 μm / 56 ± 14 nm)	N/A
			482 (13 μm / 60 ± 7 nm)	
			545 (20 μm / 45 ± 8 nm) (Length / Width)	
	[20]	60-360	860-3078	Max. 100 Ω
	[22]	80-150	N/A	700-800 kΩ

The fundamental understanding of nanometer size interconnects over a broad frequency spectrum is of great importance. Knowledge of constitutive parameters and contact impedance of NWs are necessary for the design and analysis of systems with embedded NWs. The characterization of metallic NWs at high frequencies is necessary when NWs are considered for RF interconnects. Interestingly, only a few studies deal

with high frequency characterization of individual metallic NWs; a striking difference when compared to the field of CNTs. References [23-25] show that the impedance of CNTs and corresponding contact impedance, composed of the contact resistance and contact capacitance in parallel, can be characterized by fitting equivalent circuit models to microwave measurements (typical measurement setup and circuit model are shown in Fig. 1.3). However, as pointed out in [24], the problem is that the obtained results correspond to only one set of many possible combinations of all parameters.

1.2. Carbon Nanotubes

Carbon nanotubes (CNTs) are an allotrope of carbon with a cylindrical structure having a nanometer scale diameter. Two kinds of CNTs are demonstrated, i.e., single walled CNTs (SWCNTs) and multi-walled CNTs (MWCNTs), as shown in Fig. 1.4. A SWCNT bundle, also shown in the figure, is composed of many SWCNTs. Since their discovery in the early 1990's [26], CNTs have attracted strong interest from many researchers worldwide. It is found that CNTs have superior properties from electrical, mechanical, and thermal engineering point of view over other conventional materials. This has led to CNTs being considered as a replacement for conventional materials in nanoscale devices. One focus of this thesis are metallic SWCNTs and respective bundles.

CNTs may be metallic or semiconducting, as determined by their azimuthal rolling direction. Fig. 1.5 shows a typical structure of SWCNTs with graphene which is a 2-dimensional sheet with a single-atom thickness of carbon [27]. A SWCNT is formed conceptionally by rolling up graphene along a chiral vector to form a cylinder. Any

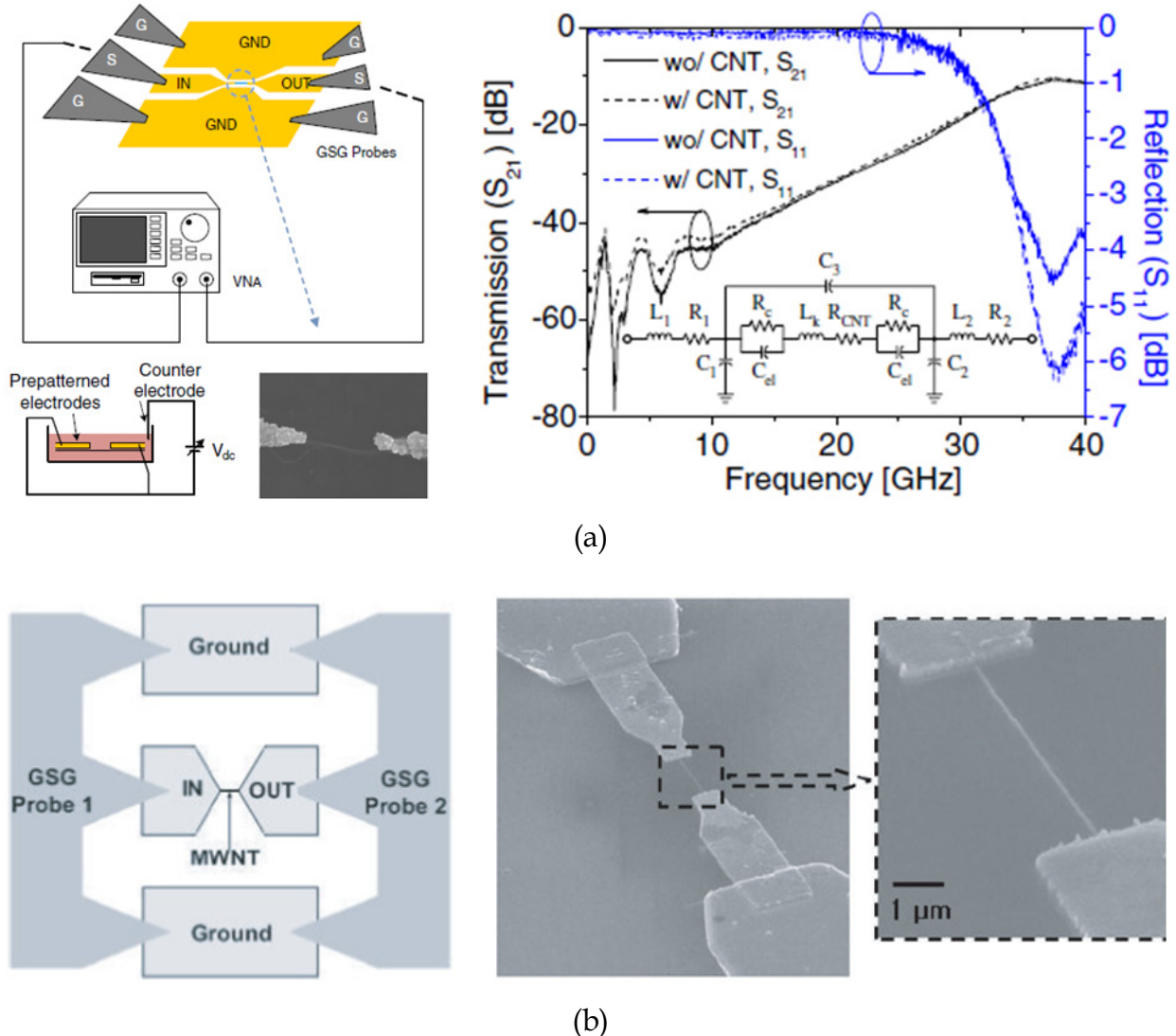


Fig. 1.3 Wideband and high frequency characterization of CNTs. (a) Two-port measurement setup for a single-walled CNT bundle, and measured S-parameters (circuit model in inset) [25], and (b) measurement setup and SEM images for individual multi-walled CNT [24]. The circuit model from (a) is used for the studies in (b)

SWCNT is represented by its chiral vector $\mathbf{C}_n = m\mathbf{a}_1 + n\mathbf{a}_2$, where \mathbf{a}_1 and \mathbf{a}_2 are unit vectors and m and n are integers known as chiral indices, and simply referred to as the (m, n) CNT. CNTs with $m = n$ are armchair CNTs, CNTs with $n = 0$ are zigzag CNTs, and the others are chiral CNTs. All armchair CNTs and CNTs with $m - n = 3i$ ($i = 1, 2$,

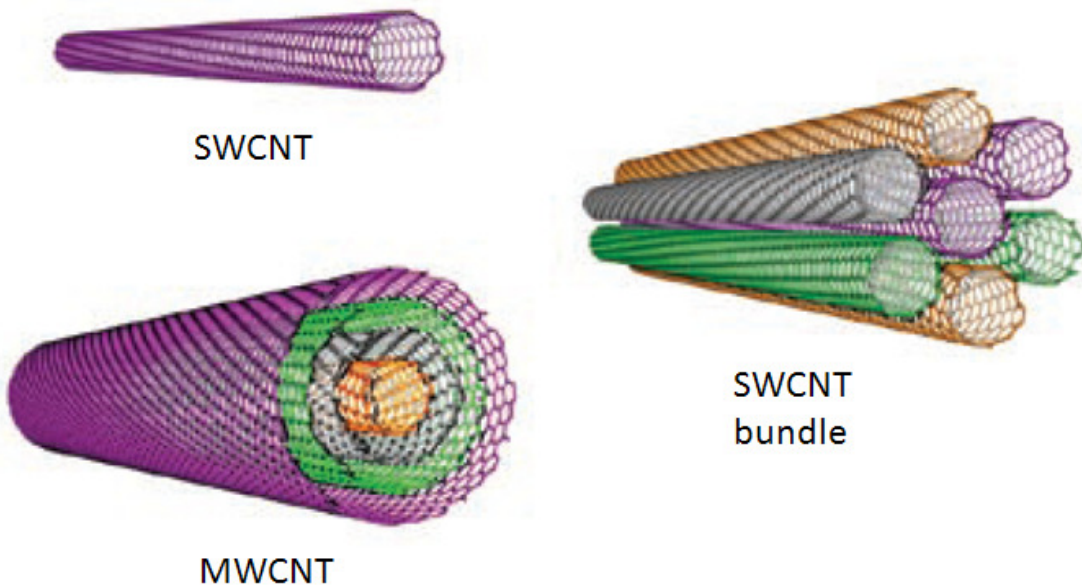


Fig. 1.4 Artistic representation of SWCNT and MWCNT. A SWCNT bundle is composed of many SWCNTs. Figure is reproduced from [27].

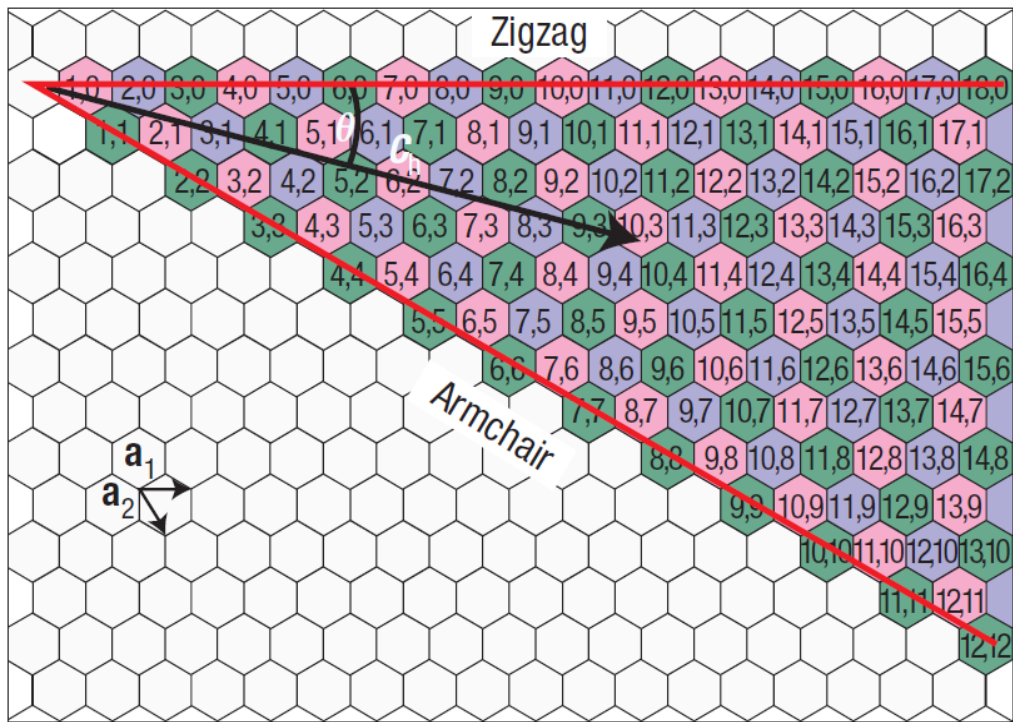


Fig. 1.5 Graphene sheet of SWCNTs [27]. A SWCNT is formed by rolling up graphene along a chiral vector (composed of \mathbf{a}_1 and \mathbf{a}_2) to form a cylinder. Red lines are particular cases of the chiral vector for armchair and zigzag CNTs.

$3, \dots)$ are metallic (green in the figure), and the others ($m - n = 3i - 1$ and $m - n = 3i + 1$) are semiconducting (pink and purple). Red lines in the figure are particular cases of the chiral vector for armchair and zigzag CNTs. Fig. 1.6 shows how three CNTs with different chiralities are formed with different rolling axes.

The physical properties of CNTs are summarized in Table 1.3. CNTs with 0.4 nm diameter were first predicted to be the smallest theoretically possible [28] and then later were synthesized [29]. Interestingly, the smallest CNTs with a 0.27 nm diameter are reported in [30], however they exist inside MWCNTs. In fact, the smallest CNTs that can be isolated and remain stable in free space have 0.4 nm diameter. Unlike larger CNTs, these 0.4 nm diameter CNTs are always metallic regardless of helicity [29]. The length of the longest SWCNTs by 2009 has been reported to be 18.5 cm [31]. Current density on a single SWCNT has been measured to be three orders of magnitude larger than that of Cu due to ballistic transport [32]. The mean free path in metallic CNTs is 1000-3000 nm, which is much larger than that in Cu (~ 40 nm). Mobility is up to 100,000 $\text{cm}^2/\text{V}\cdot\text{s}$, which is much larger than that of Si (1400 $\text{cm}^2/\text{V}\cdot\text{s}$). The high mobility may enable fabrication of much faster transistors. Intrinsic resistance of SWCNTs is known to be $6.5 \text{ k}\Omega$ (for ballistic transport; a quantum resistance of a 1D wire is about $12.9 \text{ k}\Omega$ for two conducting channels, however the SWCNTs have four channels) [33]. This high resistance is a major bottleneck for CNTs to impedance match to other devices normally designed for $50 \text{ }\Omega$. Thermal conductivity of CNTs is about $5800\text{-}6600 \text{ W/m}\cdot\text{k}$, again much larger than $385 \text{ W/m}\cdot\text{k}$ for Cu. Thus, the heat transfer may be significantly improved. Young's modulus, a measure of the stiffness of an isotropic elastic material,

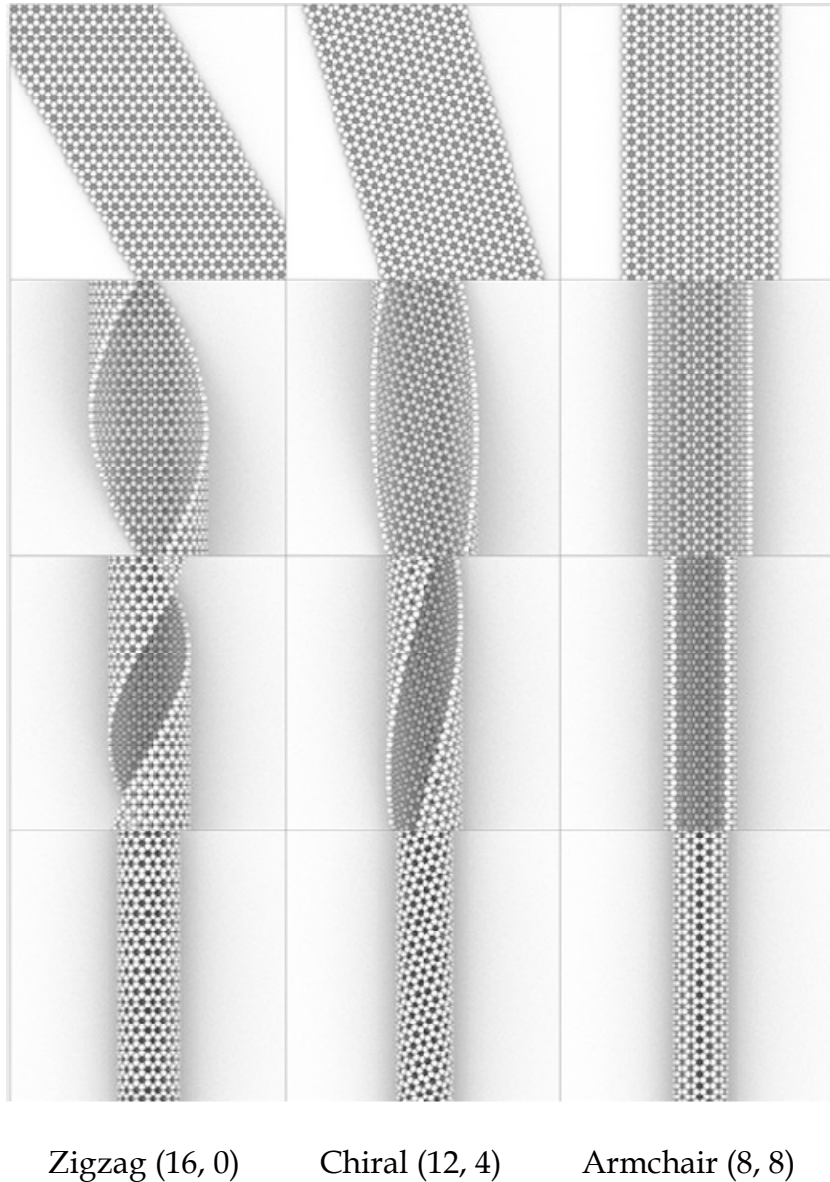


Fig. 1.6 Example of three different CNT chiralities: zigzag (16, 0), chiral (12, 4), and armchair (8,8). Each CNT starts rolling at a different slope (image from www.flickr.com/photos/l2xy2/).

of SWCNTs is 1 TPa which is five times higher than Young's modulus of steel, showing that CNTs are less compressed or stretched by pressure or tensile strain than other materials.

Table 1.3 Physical properties of CNTs from available literature [31, 32, 34].

Parameters	Value and Units
Diameter	0.27 - 100 nm
Length	Up to 18.5 cm (reported in August 2009 [31])
Current density	$> 10^9 \text{ A/cm}^2$ * 1000 times larger than Cu [32]
Mean free path (ballistic transport) @room temp.	300~700 nm for semiconducting CNT 1000~3000 nm for metallic CNT, * ~40 nm for Cu
Mobility	$\sim 100,000 \text{ cm}^2/\text{V}\cdot\text{s}$ (* $1400 \text{ cm}^2/\text{V}\cdot\text{s}$ for Si)
Conductance (ballistic transport)	$G = 4e^2/h = 155 \mu\text{S}$ ($R = 1/G = 6.5 \text{ k}\Omega$)
Thermal conductivity	5800~6600 W/m·K * 385 W/m·K for Cu
Young's modulus	1 TPa * Many orders of magnitude stronger than steel (200 GPa)

Conductivity and electromagnetic properties of CNTs are analyzed theoretically in [35]. Electrical conductivity of individual metallic MWCNTs of several nm radii has been measured by a four-probe method showing similar or an order of magnitude lower conductivity compared to Cu [36] and by a one-probe approach [37]. The results in latter show that defects on CNTs plays a significant role in the electrical transport (decreasing CNT's conductivity). A similar conclusion is found with SWCNTs [38]. The resistivity of CNTs and the contact resistance between CNTs and metal films are also studied [39-41]. The electrical contact between rhodium (Rh) and metallic SWCNTs is reported to be dependent on their diameter [42]. The contact resistances between Au electrodes and a 2.5 nm diameter bundle of metallic SWCNT (two CNTs in the bundle) are measured to be few tens of $\text{k}\Omega$ [43]. Signal propagation along CNTs over a ground plane is analyzed using transmission line theory [44]. High frequency S-parameters are

measured to show power transmission along the SWCNTs [23, 25, 45, 46], and MWCNTs [24, 47-49].

Various microwave applications of CNTs have been proposed. Polarization properties of individual SWCNTs and a bundle of SWCNTs as well as arrays of aligned CNTs are investigated for possible antenna use [50-52]. For the analysis of individual SWCNTs as dipole antennas, the Green's function [8] and transmission line theory [53] are used. References [54, 55] discuss characteristics of an array of CNTs as antennas. Dipole antennas with CNT bundles in circular and rectangular shapes are demonstrated in [56]. Also, CNT-FETs with individual SWCNTs, SWCNT bundles, and MWCNTs have been fabricated and characterized. When compared to corresponding silicon devices, they have shown similar or better performance [57]. CNTs in powder form (91 % SWCNTs) can be used for creating planar transmission lines including enclosed stripline [58]. Microwave absorbing or shielding materials are possible with MWCNT [59] or SWCNT [60]. Arrays of SWCNTs may also be used for flexible, high-performance, high-power electronics [61]. Recently, a nanotube radio achieved successful reception of commercial radio signals from 40-400 MHz [62]. The radio is composed of an antenna, a tunable band-pass filter, an amplifier, and a demodulator, all built with CNTs.

Although CNTs have outstanding properties and various potential applications, fabrication of CNT devices is still in infancy. Generally, CNTs are built in a bundle of mixed CNTs, purity of which is difficult to control. 1.28-1.52 nm diameters SWCNTs with about 40-50 % of the cottonlike carbon soot can be mass-produced by DC arc

discharge [63] and DC arc plasma jet method [64]. However, further improvements are necessary. The separation of CNTs in the bundle is another issue. Several techniques aimed to separate individual CNTs are reported in [65-68]. Reference [69] indicates the possibility for chiral-selective growth of SWCNTs.

1.3. Dissertation Organization

This thesis is organized as follows: Chapter 2 establishes modeling and measurement methodology for characterization of conductivity and contact resistance for individual Pt NWs embedded in coplanar waveguide (CPW) devices. Pt NWs with direct RF contacts to CPW are measured over a wide frequency range by a traditional two-port, probe-based setup. To determine the conductivity and contact resistance of Pt NWs, full-wave models using FEM and circuit models are developed after thorough modeling validations. Computational results are then fitted to measurements. It is seen that the single NW test bed enables determination of the range for NW conductivity and contact resistance. In order to simultaneously determine their values, a two-device measurement setup and associated transmission line and lumped element based algorithms are developed. Feasibility of both algorithm approaches is investigated using full-wave and circuit models. An approach using lumped element models, which provides more accurate results, is validated experimentally for devices with a Au short, and utilized to determine contact resistance and conductivity for 300 nm diameter Pt NWs, resulting in about 50Ω and $0.013\sigma_{bulk}$, respectively. Although developed for Pt

NWs and CPW hosts, the approach and algorithm can be applied to other NWs and host quasi-TEM transmission lines.

Chapter 3 discusses contactless approaches for characterization of Pt NW's conductivity. The aim is to eliminate the uncertainty of the contact impedance between the NWs and CPW, thus significantly simplify the metrology. Two setups with different geometrical configurations for achieving the displacement current coupling are developed. In the first setup, a NW is deposited in a slot that is etched from the CPW signal line. Thus the NW is on the same plane as the signal line and the coupling occurs horizontally. In the second setup, the Pt NW is deposited on a dielectric layer fabricated on the top of the CPW signal line. That way the coupling occurs vertically. To determine the Pt NW conductivity, FEM models for the two configurations are developed and fitted to measurements. Obtained conductivity for a 340 nm Pt NW is $0.014\sigma_{bulk}$, which is well correlated with the result from the direct contact method in Chapter 2. Structural and elemental analysis for the fabricated devices are also provided to complete discussion of fabrication and measurement issues.

Modeling and characterization of individual SWCNTs and their interconnect applications at microwave frequencies are discussed in Chapter 4. CNTs are modeled using MoM and FEM by applying a frequency-dependant conductivity with embedded quantum effects. Three-step validation methodology is established for the MoM wire models with CNT dipole antennas, MoM surface models with CNT dipoles, and FEM models with coaxial lines having CNTs as their inner conductor. Finally, the performances of CNT based dipole antennas, nano-coaxial lines, and single wire

transmission lines are compared to their Cu-based counterparts. Superior performance of SWCNTs to that of a traditional Cu interconnect is demonstrated.

Chapter 5 discusses modeling and characterization of CNT bundles and their microwave interconnect applications. CNT bundles are used to overcome the drawbacks of high impedance and loss of individual CNTs. Modeling and validation approaches follow those from Chapter 4. Considered interconnects include CNT bundle monopole antennas, nano-coaxial lines with CNT bundles as their inner conductor, and single wire transmission lines composed of CNT bundles. Performance of each interconnect is compared to that of respective Cu-based counterpart. Various CNT topologies in the bundles are also examined. It is concluded that CNT bundles represent viable interconnect with better performance than traditional Cu based counterpart.

Finally, Chapter 6 overviews the thesis, summarizes the contributions and outlines several possible directions for future work.

CHAPTER 2

CHARACTERIZATION OF PLATINUM NANOWIRES (I) - CONTACT IMPEDANCE AND CONDUCTIVITY

Over the past decade, metallic nanowires (NWs) have been studied as potential building blocks for various nanoscale electronic systems including broadband interconnects, sensors, and field effect transistors [12]. Characterization thereof, including measurements and modeling, is still in its infancy and needs to be further developed. Understanding contact effects arising from the transition of individual NWs to host device platforms is of great importance for future NW's use. Resistivity of Au [21], Cu [7], and Pt [19] NWs is typically investigated assuming negligible contact resistance. A wide range of resistivity and contact resistance of Pt NWs is reported in [6, 20, 22]. All these studies [6, 7, 19-22] have been performed experimentally at DC or low frequency. Frequency-dependant material parameters and contact impedance for multi-walled CNTs are studied in [24], while frequency-invariant parameters for a SWCNT bundle are discussed in [49]. Common themes in these papers are the use of experiments and circuit modeling and an overall conclusion that the fabrication, measurements, and theoretical characterization of NWs are difficult.

This chapter discusses wideband characterization of individual Pt NWs with two-port measurements, as well as full-wave and circuit modeling. Finite-element full-wave models within ANSYS HFSS [70] and circuit models within AWR Microwave Office [71] are developed to characterize conductivity and contact resistance of Pt NWs with 100 and 250 nm diameters. Both models are validated by comparing to broadband measurements conducted from 50 MHz to 50 GHz with on-wafer multiline thru-reflection line (TRL) calibration [72, 73] for two simple coplanar waveguide (CPW) test-beds. Specifically, CPW devices with and without Au bridges are fabricated, simulated, and measured to show the suitability of on-wafer TRL calibration and demonstrate modeling accuracy for the characterization of nanoscale devices. Then, measurements and simulations are carried out for Pt NWs with 100 and 250 nm diameters. Modeled conductivity and contact resistance are fitted to measurements until the standard deviation between modeling and measurements is minimized. Minimal and maximal values of conductivity and contact resistance are thus determined from a single setup. The study is extended to develop two algorithms that extract the conductivity and contact resistance of each NW. The algorithms are based on a conventional transmission line theory [74] and equivalent lumped element models. Both approaches provide the two unknown parameters from the measurements of two Pt NWs with different lengths.

This chapter is organized as follows:

- Section 2.1 introduces fabrication and measurement methodologies of CPW devices used for calibration, modeling validation, and subsequent characterization of Pt NWs. Geometrical details for the CPW, calibration

standards, and test chips layout are described. Fabrication including the deposition of Pt NWs and the measurement setup are also provided.

- Section 2.2 discusses applied modeling methods and their validation. FEM-based full-wave modeling is chosen and validated first. Next, two circuit-level modeling tools and MoM-based full-wave modeling are used to find an appropriate circuit model for NWs. The evaluation is made by comparing each modeling result to measurements. CPW devices with and without Au bridges are employed for modeling validation.
- Section 2.3 provides modeling and analysis approaches for determining the conductivity and contact resistance of Pt NWs. Full-wave models are modified in order to separate effects of the conductivity and contact resistance. To improve accuracy of circuit models, they are hybridized by combining MoM simulations for CPWs and tapered CPWs and circuit models for the NWs and contact resistance. Both full-wave and circuit models are fitted to measurements to determine ranges of conductivity and contact resistance. Adjusted conductivity and contact resistance are introduced to simplify the analysis. The results are verified by comparing to prior work reported by other groups.
- Section 2.4 describes two algorithms developed herein to simultaneously determine the conductivity and contact resistance of NWs. The first is based on the transmission line models for Pt NWs, and the second utilizes lumped element models. Relevant theory for both methods is provided, and their feasibility is computationally investigated. Then, an approach based on lumped element is

validated experimentally for devices with Au short, and it is used to determine the contact resistance and conductivity of measured Pt NWs.

2.1. Fabrication and Measurements

2.1.1. Coplanar Waveguides and Calibration Standards

The measurement framework is established for devices with and without a Pt NW, as well as devices with a Au short. Note that devices with and without a Au short have extremely low and high impedance, respectively. In order to produce test structures compatible with high-frequency measurements, individual Pt NWs of 100 and 250 nm diameters are incorporated into the middle of the two-port CPW host. A schematic for the measurement setup is shown in Fig. 2.1. Each device includes a 1200 μm -long CPW segment with 4 μm gap in the middle of the signal line. 100 μm of the signal line to either side of the gap is tapered to constrain the area where Pt NWs can bridge the gap and to reduce the physical discontinuity between the signal lines and Pt NWs. The characteristic impedance of the CPW line is approximately 50 Ω . The devices are fabricated using conventional photolithography on a polished quartz substrate. A 120 nm thick Ti layer and a 200 nm thick Al layer are sequentially deposited to create the signal trace of the CPW transmission line. A 300 nm thick Au layer is deposited to form the ground plane.

For the purpose of modeling validation, devices with Au short of either 1 or 2 μm width are fabricated in two different ground configurations, via photolithography on a separate wafer. The first ground configuration has a constant width between both

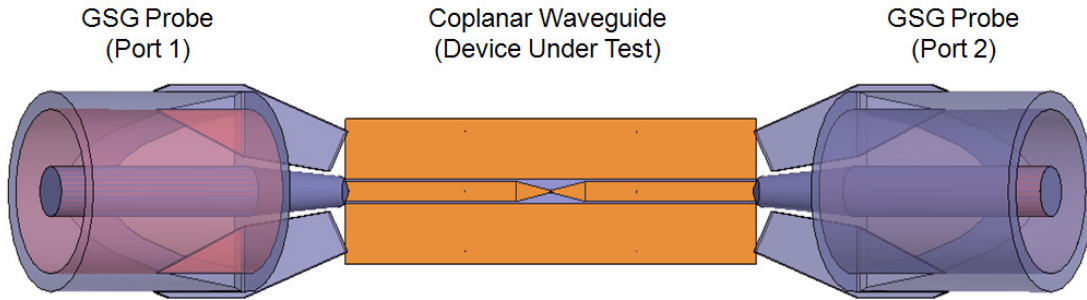


Fig. 2.1 Schematic of a CPW-based measurement setup.

sides of the ground plane, while the second has a constant width between the ground plane and the CPW signal lines. A Au short is fabricated at the center of the gap or offset either to the upper or lower side in the gap. The thickness of signal lines and ground is 200 nm. The length of tapered sections is 75 μm . A chip layout for these devices is shown in Fig. 2.2.

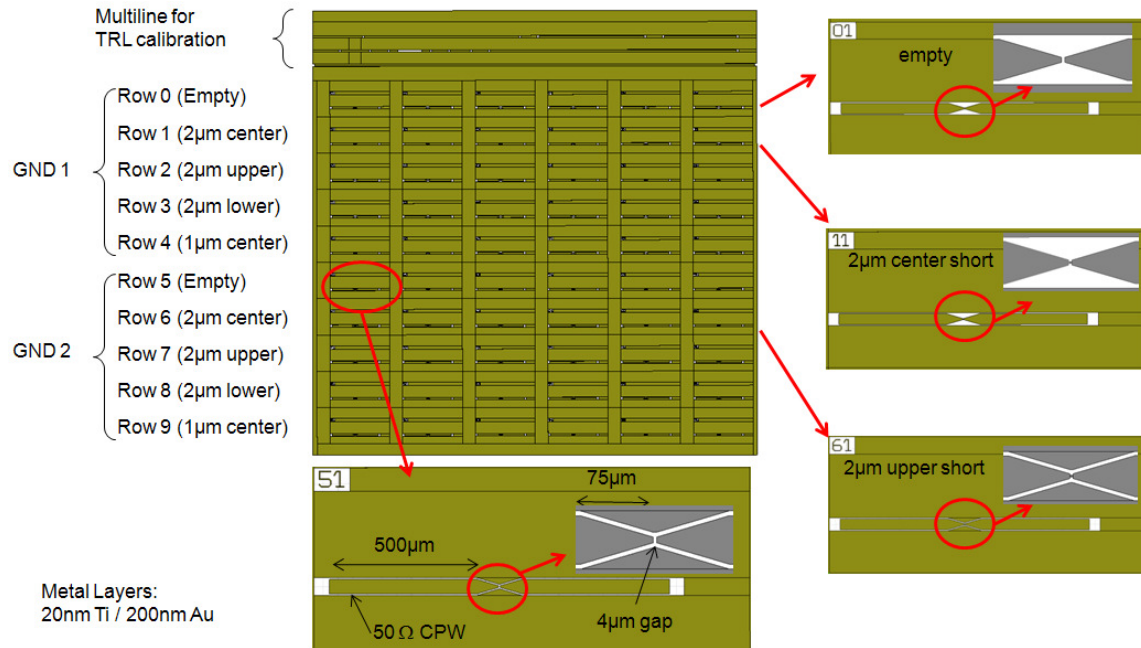


Fig. 2.2 Chip layout of two different ground configurations for modeling validation.

To measure the devices over a wideband frequency range, CPW calibration standards needed for the on-wafer multiline TRL calibration [72] are fabricated on each chip. By producing a full set of calibration lines on each chip, the measurement uncertainty is reduced because the thickness of the metal layer may be nonuniform throughout the wafer, i.e. from chip to chip. The *line* lengths are 1.8 mm, 2.6 mm, 3.83 mm, and 6.1 mm, the *thru* is 0.5 mm, and *reflect* (both open and short) are 0.2 mm, which are the same as in [73].

2.1.2. Platinum Nanowire Deposition

The Pt NWs are deposited by using a dual beam focused ion beam (FIB) system. The FIB uses a Ga ion beam to deposit material by high energy dissociation of a metal bearing gas. A field emission scanning electron microscope (SEM) is focused at the same position as the Ga ion beam allowing viewing of the sample modifications in progress. A SiO₂ insulating support structure is first deposited between the CPW electrodes to allow the Pt NW to be as continuous and uniform as possible. Pt NWs of 10 μm length and 100 nm or 250 nm width are deposited between the electrodes across the insulating structure. SEM photographs for devices with and without Pt NW are shown in Fig. 2.3. During deposition the ion beam energy is kept at 30 kV and the current is held at 20 pA. The vacuum in the specimen chamber is 5×10^{-6} Torr and deposition duration is approximately 30 sec.

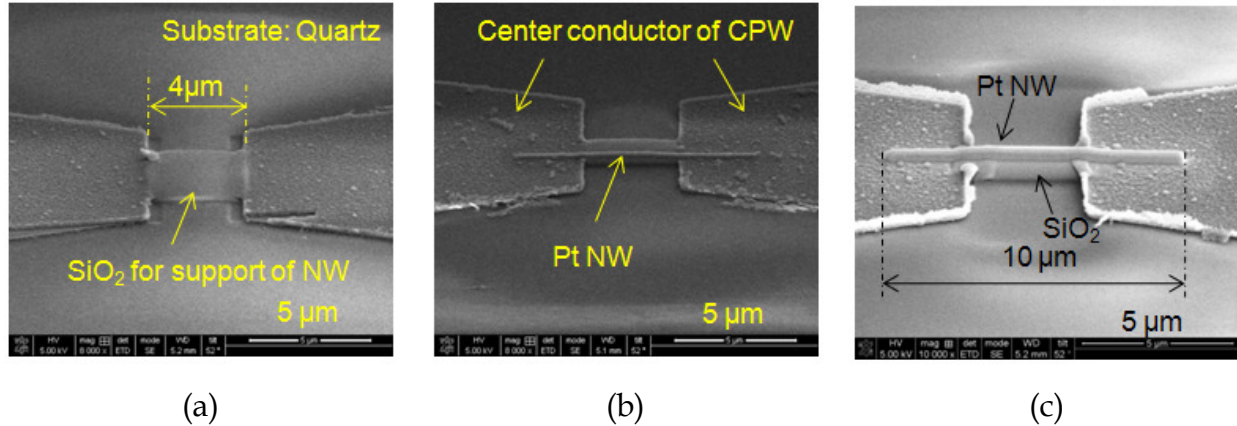


Fig. 2.3 SEM photographs of devices under test: (a) empty device, (b) device with 100 nm diameter Pt NW, and (c) device with 250 nm diameter Pt NW.

2.1.3. Two-port Measurements

Two-port S-parameter measurements are made by a vector network analyzer with an on-wafer measurement system. The system consists of two ground-signal-ground (GS_G) microwave probes, two probe manipulators, and an optical microscope. The measured frequency range is from 100 MHz to 40 GHz or from 50 MHz to 50 GHz for HP 8510C network analyzer or Anritsu Lightning network analyzer, respectively. Multiline TRL calibration is performed by the use of NISTcal [75]. As a sanity check for repeatable contact between probes and devices under test, direct current (DC) resistance from port 1 to port 2 is measured during each measurement by a multimeter connected to both ports of the VNA. In this way, the high frequency S-parameters and the DC resistance are measured simultaneously. These measurements are carried out at low RF powers (< 1mW).

2.2. Modeling Methods and Validation

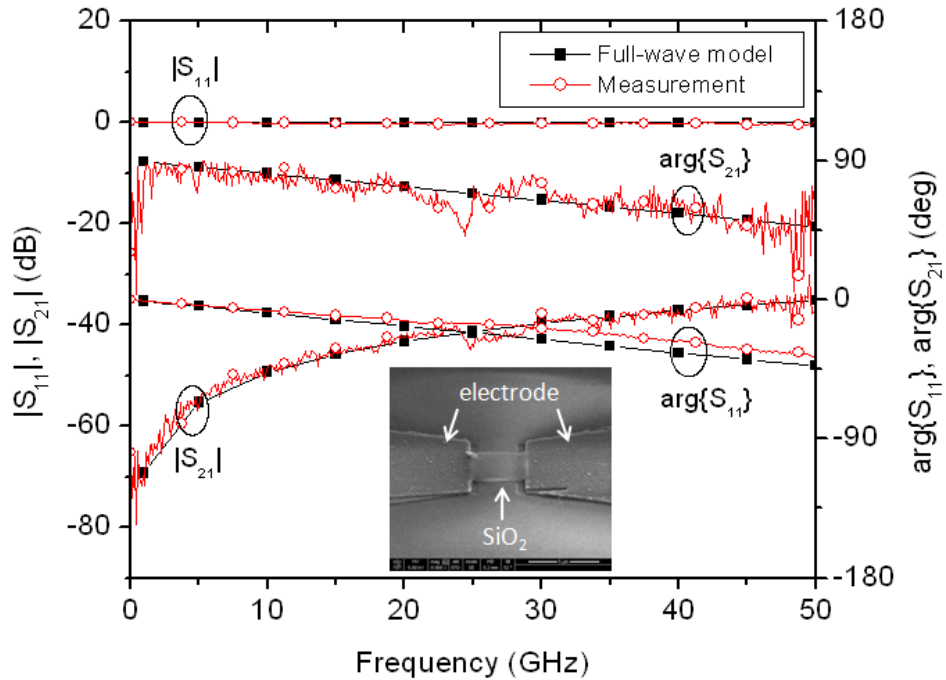
To determine electrical parameters associated with the NWs, specifically conductivity and contact resistance, measured S-parameters for devices with Pt NWs are compared with full-wave and circuit simulations. Full-wave modeling is conducted with FEM-based ANSYS HFSS and MoM-based AWR Microwave Office. For circuit models, AWR Microwave Office and ANSYS Designer [76] are used. Before the Pt NWs are characterized, devices with and without a Au short are modeled first for validation purposes. If this step is successful, then the applied modeling approaches would be valid from extremely low impedance (devices with a Au short) to extremely high impedance devices (devices without a Au short or empty devices). Each method and obtained results are discussed in this section.

2.2.1. Finite Element Method

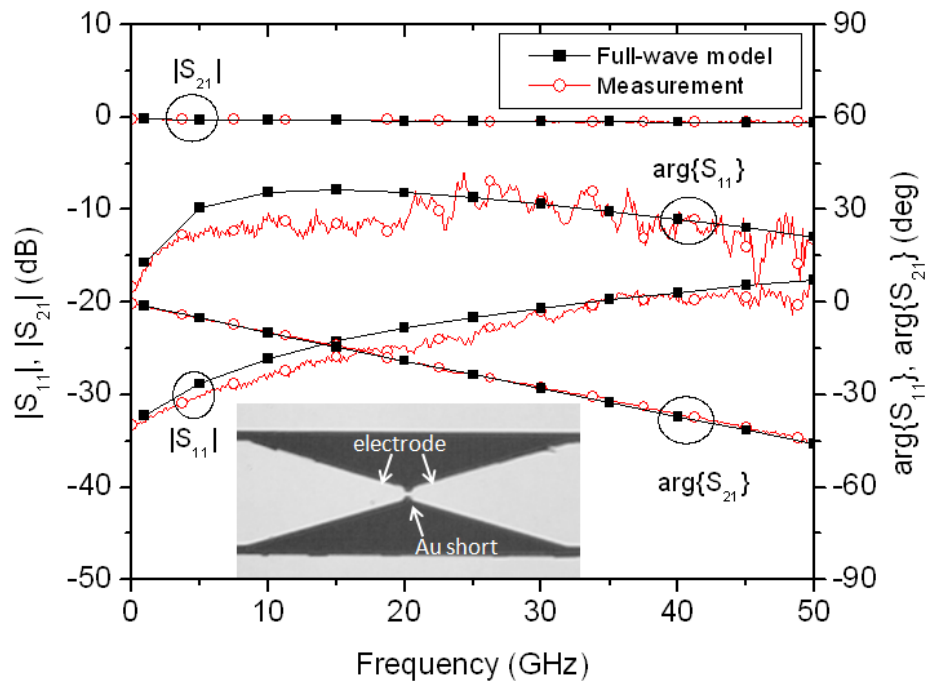
The first modeling method utilized is the FEM as implemented within ANSYS HFSS. This full-wave FEM code is based on the solution of the weak form of the 3-D wave equation and it enables accurate analysis of open and closed domain boundary value problems. The method is inherently flexible to deal with arbitrary inhomogeneous materials and structural shapes. Field expansion is performed in several polynomial orders and the user is allowed great control of various setups and steps in the solution process. However, the full-wave method requires heavier computational resources, computer memory and computation time, than circuit-based modeling methods. To reduce the computational overhead associated with volumetric

meshing, two GSG probes shown in Fig. 2.1 are replaced by ideal wave ports. Devices with and without a Au short are modeled. Several different Au short devices shown in Fig. 2.2 are designed and built including the 2 μm -wide center Au short devices used here. The simulations and measurements have shown that their S-parameter responses are very close to those of the other Au short devices.

Measurements are conducted from 50 MHz to 50 GHz with on-wafer multiline TRL calibration. Measured and simulated results for devices without and with a Au short are compared in Fig. 2.4 (a) and (b), respectively. As seen, an excellent agreement for both devices is obtained. The maximal differences between simulations and measurements are $\pm 7^\circ$ for $\arg\{S_{11}\}$ and ± 0.5 dB for $|S_{21}|$ for the empty device (high-impedance). For the device with a Au short (low-impedance), about 10° difference in $\arg\{S_{11}\}$ is observed from 5 GHz to 20 GHz, however the trends for simulations and measurements are generally well correlated. The maximum difference in $|S_{21}|$ is below 0.1 dB. These results verify suitability of both the on-wafer calibration technique and finite-element simulations for experimental and theoretical study of devices having small size and possibly an extreme range of impedance values. Note that the TRL and other on-wafer calibration techniques assume single mode propagation. When the reference planes are moved by 100 μm , no significant difference in results is recorded, suggesting that the excitation of higher order modes does not play a significant role. Moreover, the three-dimensional FEM analysis that enables the excitation and propagation of higher modes (if the physics of the boundary value problem permits their existence) shows that only the fundamental TEM mode is excited on the line.



(a) S-parameters for devices without Au short



(b) S-parameters for devices with Au short

Fig. 2.4 Simulated and measured S-parameters without (a) and with (b) Au short. SEM pictures of the devices are shown as insets.

Higher order modes that might be caused by a discontinuity along the CPW signal lines have been further investigated using FEM. Models for the device with 2 μm -wide Au short in two ground configurations (GND1 and GND2 shown in Fig. 2.2) are excited by a fundamental mode at port 1. The first five higher order modes at both ports, 1 and 2, are then analyzed. Also, power losses are computed for ground layers, signal lines of Au layers, signal lines of Ti layers, and radiation, separately. Figure 2.5 shows power distribution for all modes and loss powers. Note that the sum of all partial powers shown in the figure is approximately 100% for each ground configuration. A few observations and conclusions can be made from the figure:

- The contributions of higher order modes are negligible in this measurement setup, thus using the fundamental mode is appropriate as mentioned above;
- GND2 produces less reflection and more transmission which causes larger loss from metallic layers;
- GND2 is considered to give rise to less radiation due to a better impedance match in the taper section. Based on these observations, the GND2 configuration is preferred over GND1.

2.2.2. Circuit and Method of Moments Models

In order to verify the feasibility of circuit modeling for the small devices, AWR and ANSYS Designer are used, and their simulated results are compared to measurements. The devices under test are the empty device and the device with a Au short of 2 μm width in the middle of the CPW structure (the same as Section 2.2.1). In an

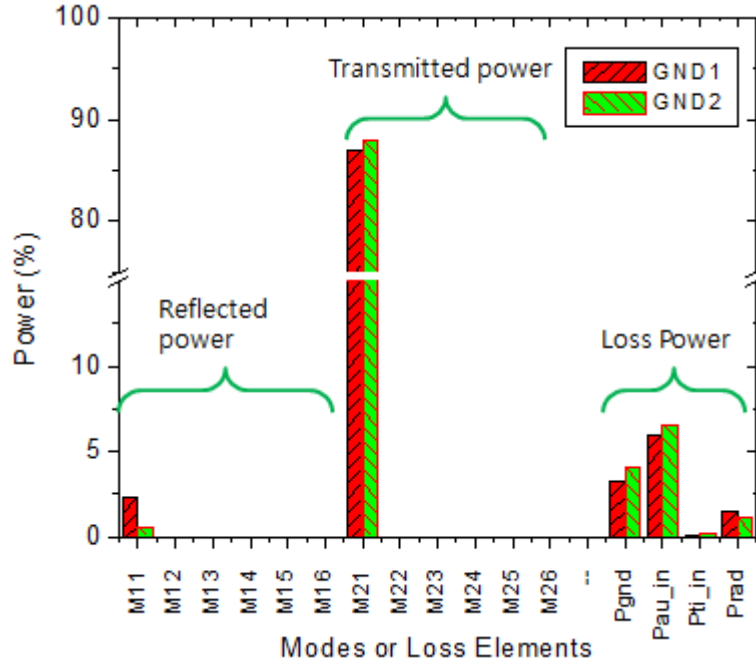


Fig. 2.5 Power analysis of the CPW devices with 2 μm -wide Au short. The first 5 higher order modes and the fundamental mode are included in both ground configurations. $M_{\alpha\beta}$ represents a mode of which α is the port number and β is the mode number. P_{gnd} is the loss power from ground layers, $P_{\text{au_in}}$ is from CPW signal lines of Au layers, and $P_{\text{ti_in}}$ is from CPW signal lines of Ti layers. P_{rad} is the radiated power.

AWR circuit model, a capacitance, C_{gap} , is added to represent the coupling effect between the two tapers as shown in Fig. 2.6. The value of C_{gap} is determined by fitting the AWR model to a FEM full-wave model from ANSYS HFSS, which is validated in the previous section, and found to be 0.6 fF. This value is much larger than 5.3 aF (10^{-18}) calculated from the static capacitance formula because of stray fields from top and bottom surfaces of a tapered signal line to those of the other tapered signal line (The stray field distribution was observed in full-wave simulations). As shown in Appendix B, C_{gap} plays a significant role for high impedance devices. In addition to the circuit models, a full-wave model based on MoM from AWR is utilized for comparison. MoM

simulations solve the problem by the use of the Galerkin method. Modeling procedures and validation on MoM are provided in Appendix A.2.

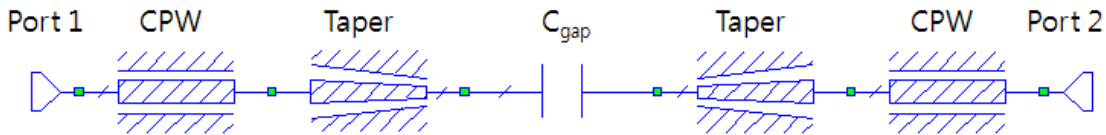
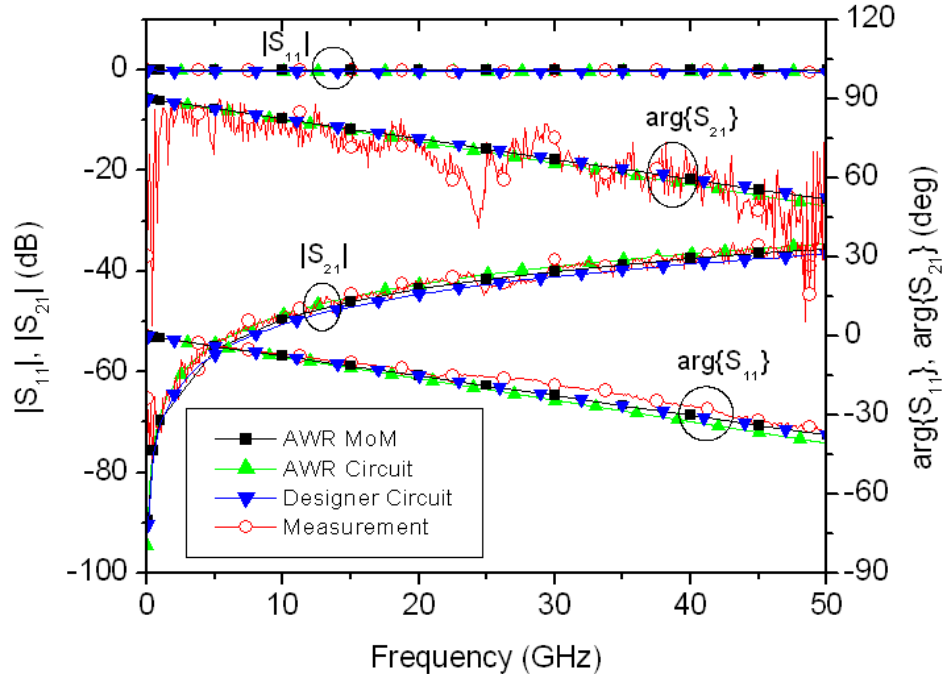
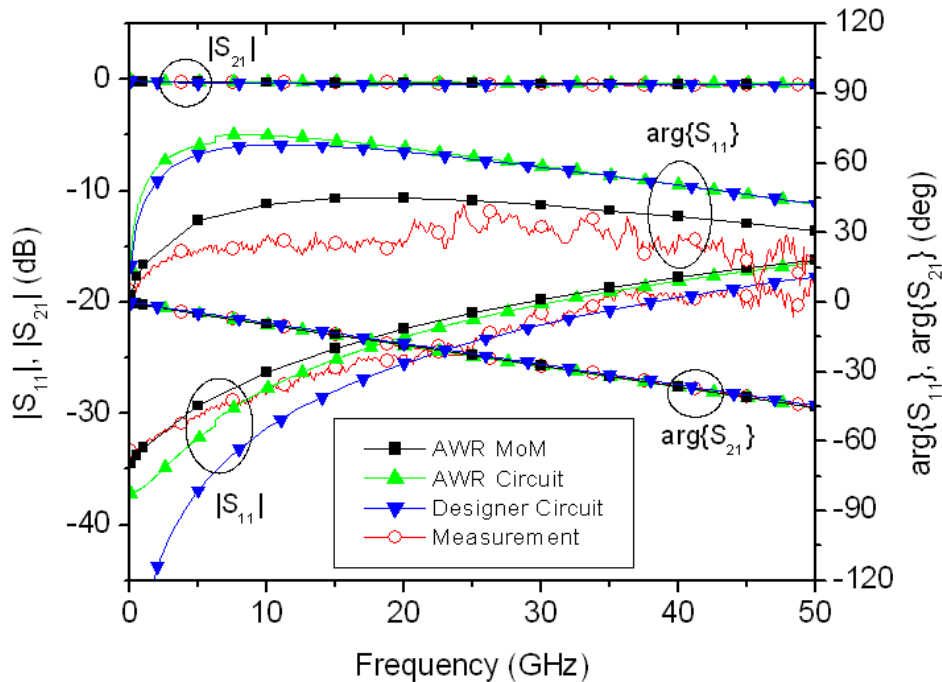


Fig. 2.6 AWR circuit model for the empty device under test.

Simulated and measured S-parameters for both devices are shown in Fig. 2.7. Results from AWR and Designer circuit models, and AWR MoM models are given. The measured data in the figure is the same as in Fig. 2.4. An excellent agreement is observed for the empty device (Fig. 2.7 (a)), while some disagreement for S_{11} is shown for the device with 2 μm -wide Au short (Fig. 2.7 (b)). In contrast to circuit simulations, the MoM results agree well with measurements for S_{11} in Fig. 2.7 (b). In fact, the MoM models have a problem that the tapered CPW cannot be excited directly but needs additional ‘wave-launching line’ (see Appendix A.2). This could introduce some errors and special care must be exercised. The MoM models can be improved by reducing the geometrical errors. Both circuit models result in very similar responses generally, but slight difference is observed for $|S_{21}|$ in Fig. 2.7 (a) and $|S_{11}|$ in Fig. 2.7 (b). Note that results from AWR circuit models are closer to measurements and MoM models than those obtained with the embedded Designer circuit models. The maximal differences between simulations and measurements are 5° in $\arg\{S_{11}\}$ and ± 3 dB in $|S_{21}|$ for the empty device. From the results, it can be concluded that the circuit models for the small



(a) S-parameters for the empty devices without Au short



(b) S-parameters for the devices with Au short

Fig. 2.7 Simulated and measured S-parameters for (a) the empty device, and (b) the device with Au short of 2 μm. Simulations are conducted from AWR MoM and circuit models, and ANSYS Designer circuit model.

devices are appropriate for high impedance devices (i.e. the empty device) but not for very low impedance devices (i.e. the device with Au short). These results suggest that a hybrid model combining MoM models for CPW and taper sections and circuit models for the gap and the NW can improve accuracy. This will be further discussed for devices with Pt NWs in Section 2.3.2.

2.3. Fitting Methods

In this section, the modeling of devices with 100 and 250 nm diameter Pt NWs is conducted to characterize their conductivity and contact resistance. full-wave FEM and circuit modeling results are fitted to measurements and relevant parameters are determined. For this study, reactance is negligible thus allowing the contacts to be treated as purely resistive.

2.3.1. Initial Setup for the Full-Wave Models

A single Pt NW is incorporated in the FEM models, as shown in Fig. 2.8. The NW is placed in the middle of the CPW structure, and it is directly contacted to the CPW signal lines. The SiO_2 dielectric layer is included to support the NW. The corresponding SEM image of the 250 nm diameter NW is shown at the bottom right. Dimensions for the NWs are estimated from the SEM images. A total length of the CPW section is 500 μm . However, the length of the CPW in modeling is set at 150 μm in order to reduce required computational resources. This length is sufficient for the establishment of the TEM mode on the line before approaching the tapered section of the CPW line.

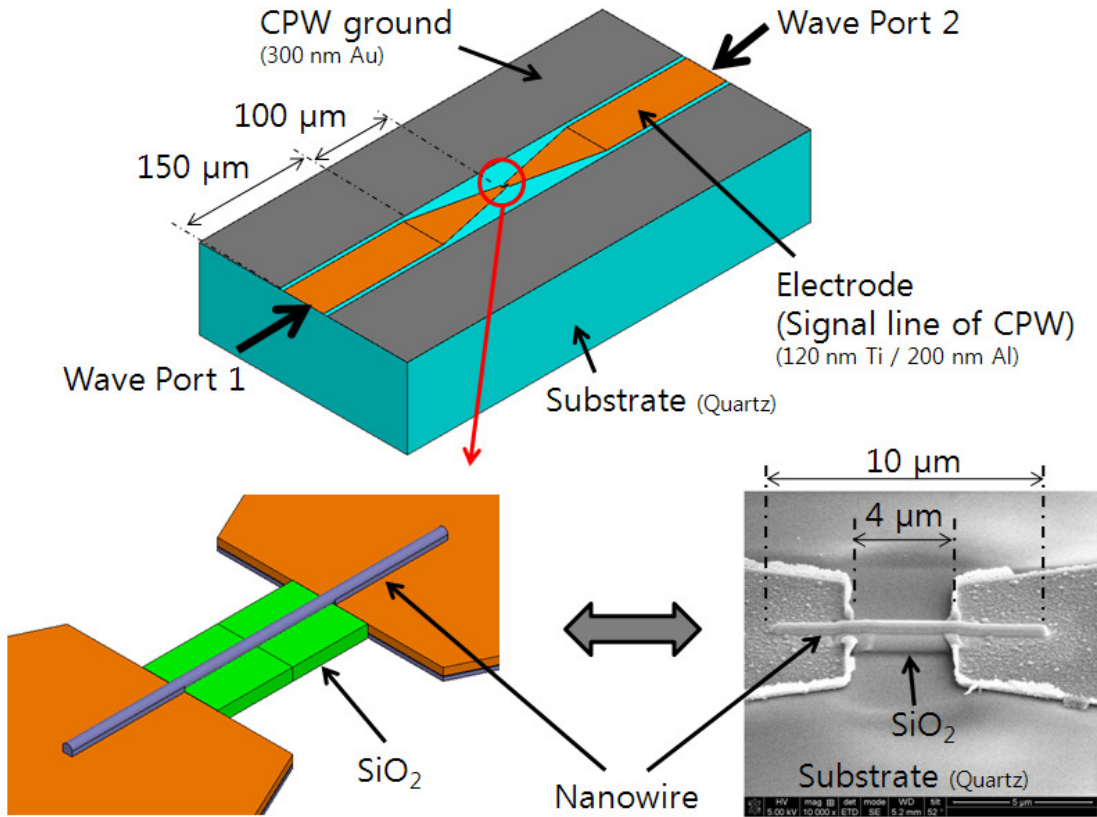


Fig. 2.8 Initial FEM modeling setup for the device with an individual Pt NW of a 250 nm diameter. The NW is placed in the middle of the CPW structure, and directly contacted to CPW signal lines. The SiO_2 dielectric layer supports the NW in the gap of CPW signal lines. The associated SEM image of the NW is shown at bottom right side.

The conductivity of Pt NWs is first set at its macroscopic bulk conductivity of $\sigma_{bulk} = 9.3 \times 10^6 \text{ S/m}$. The contact between Pt NWs and electrodes is initially assumed to be perfect, i.e. $R_c = 0 \Omega$, where R_c denotes the contact resistance. Devices with a 250 nm diameter Pt NW are simulated, and the results are compared to measurements in Fig. 2.9. As seen, the computed S-parameters for $\sigma = \sigma_{bulk}$ and $R_c = 0 \Omega$ are quite different from measurements indicating that the material properties of Pt NWs are different to those of bulk Pt and the contact resistance is finite but non-zero. Also, it is observed that

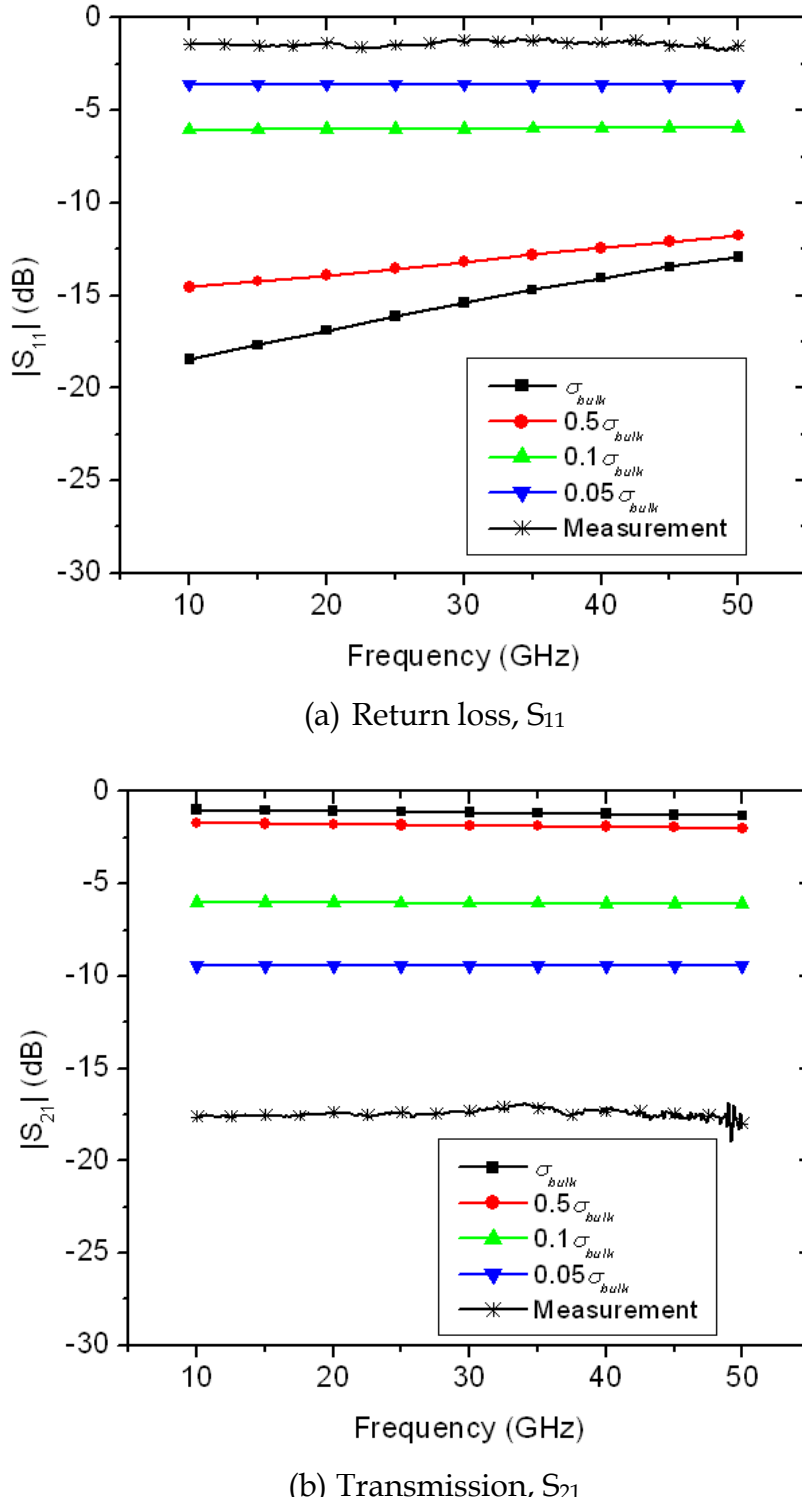


Fig. 2.9 Simulated and measured S-parameters for devices with Pt NW of 250 nm diameter. Contact resistance is assumed to be 0Ω for simulations. Conductivity of Pt NW varies from σ_{bulk} to $0.05\sigma_{bulk}$. Reducing the conductivity results in less difference between simulations and measurements.

by reducing the Pt NW conductivity the simulated results converge to the measured S-parameters.

The contact resistance in FEM is modeled by applying a lumped impedance boundary condition. In order to verify the applicability of this boundary condition, two test devices are assembled. First, the lumped impedance boundary condition is applied between the NW and CPW signal line. Secondly, an auxiliary 3-D block object is used as a substitute for the impedance boundary condition. Its dimensions and resistivity are determined such that its resistance equals to that of the impedance boundary, that is, a surface area of $20 \text{ nm} \times 250 \text{ nm}$, length of 10 nm , and resistivity, ρ , of $157.4 \mu\Omega/\text{m}$ for 315Ω . Schematics for both structures and computed S-parameters are shown in Fig. 2.10. As seen, excellent agreement assures that the impedance boundary condition is appropriate for this study.

2.3.2. Initial Setup for Circuit Models

A schematic of the circuit model for the device with an individual Pt NW is shown in Fig 2.11. As mentioned in Section 2.2.2, segments designed as ‘CPW’ and ‘Taper’ are modeled using MoM for improved accuracy, while other parts of the setup are circuit elements as used in AWR’s library. In this way, the computational cost is significantly reduced. A contact resistance, R_c , between the NW and the taper is included to take into account contact effects. A parallel capacitance C_{gap} represents the coupling capacitance between the two tapers, and its value is the same as in the empty device (see Section 2.2.2).

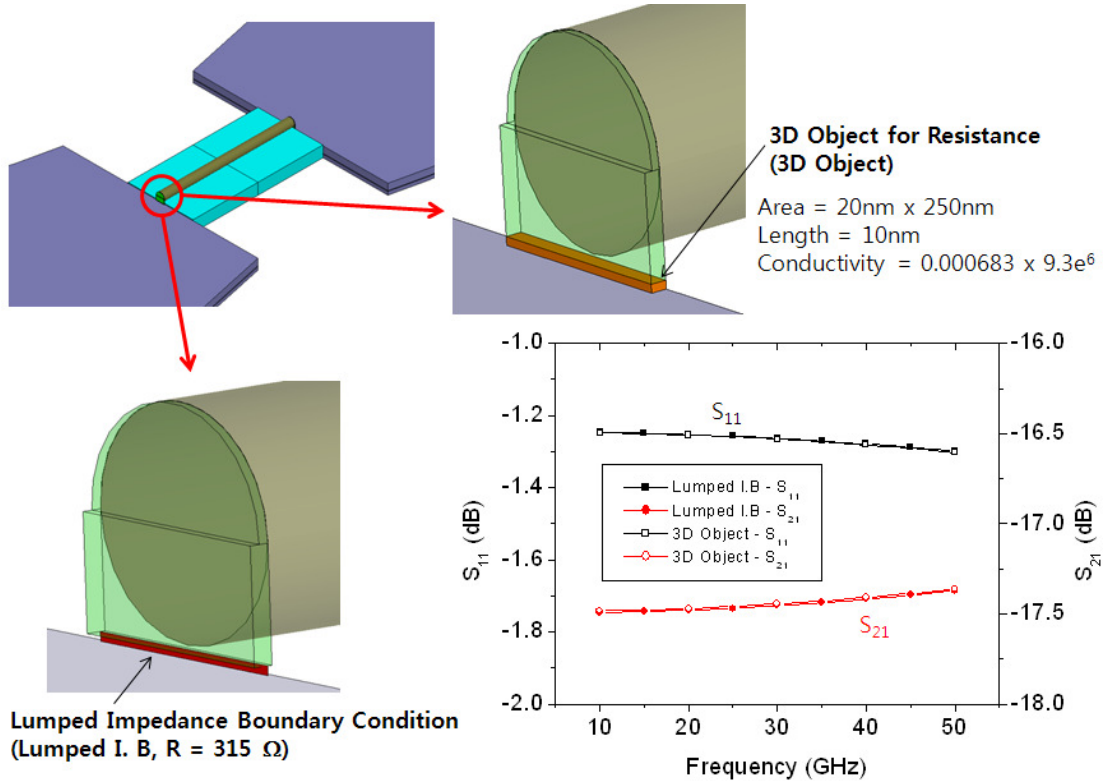


Fig. 2.10 Modeling setup for validation of the lumped impedance boundary condition from full-wave FEM models, and their computed results. Resistance is assumed to be 315Ω .

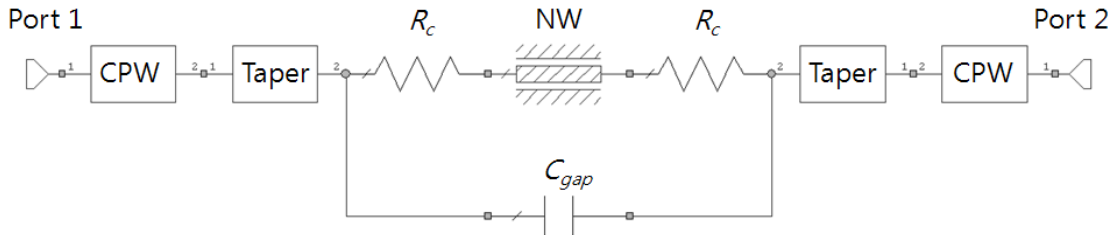


Fig. 2.11 Schematic of AWR model for the device with a Pt NW under test. Sections of CPW and taper are modeled with MoM, while the gap and the NW are modeled with circuit elements.

Pt NWs are assumed to have cylindrical shape with 100 and 250 nm diameters, and they are placed as a signal line in the CPW configuration that is shown as 'NW' in Fig. 2.11. However, the signal line of the CPW segment from AWR is formulated with a

rectangular strip. To convert the shape of a Pt NW from circular cylinder to the rectangular strip (see Table 9.3 in [77]), an FEM model of the CPW is employed. In this case, a perfect contact between the NW and taper ($R_c = 0 \Omega$), and bulk conductivity of Pt, σ_{bulk} , are assumed. As a result, the effective width and thickness of the strip from AWR are determined to be 200 nm and 23 nm for the 100 nm diameter Pt NW, and 500 nm and 57 nm for the 250 nm diameter Pt NW, respectively.

2.3.3. Approaches

Simulations with bulk conductivity and perfect contact for the Pt NWs result in poorly correlated S-parameters to measurements because of the NW's small size. Varying either conductivity of Pt or R_c changes the simulation results, thus allowing for parameter tuning in order to achieve good agreement between simulations and measurements. However, since a single test device is used for two unknown parameters, it is not possible to determine both parameters simultaneously. Instead, the range for contact resistance and conductivity can be found [10].

To determine the ranges for the conductivity and contact resistance, two fitting approaches are carried out. First, an adjusted conductivity of Pt NWs is introduced by setting $R_c = 0 \Omega$, allowing for the minimal possible NW conductivity to be found. Second, an adjusted contact resistance is introduced by setting the conductivity of the Pt NW to $\sigma = \sigma_{bulk}$, thus allowing for the maximal possible contact resistance to be determined. In both cases, the adjusted conductivity and adjusted contact resistance represent an aggregate of the actual conductivity and contact resistance for specific

diameter nanowires. Note that the contact effects may be represented by a complex impedance [24], however results show that for the studied devices the contact reactance has an insignificant effect.

A flow chart for the undertaken analysis approaches is depicted in Fig. 2.12. As seen, these methodologies can be applied for full-wave FEM or circuit models. Note that circuit models require an additional step that is described in Section 2.3.2.

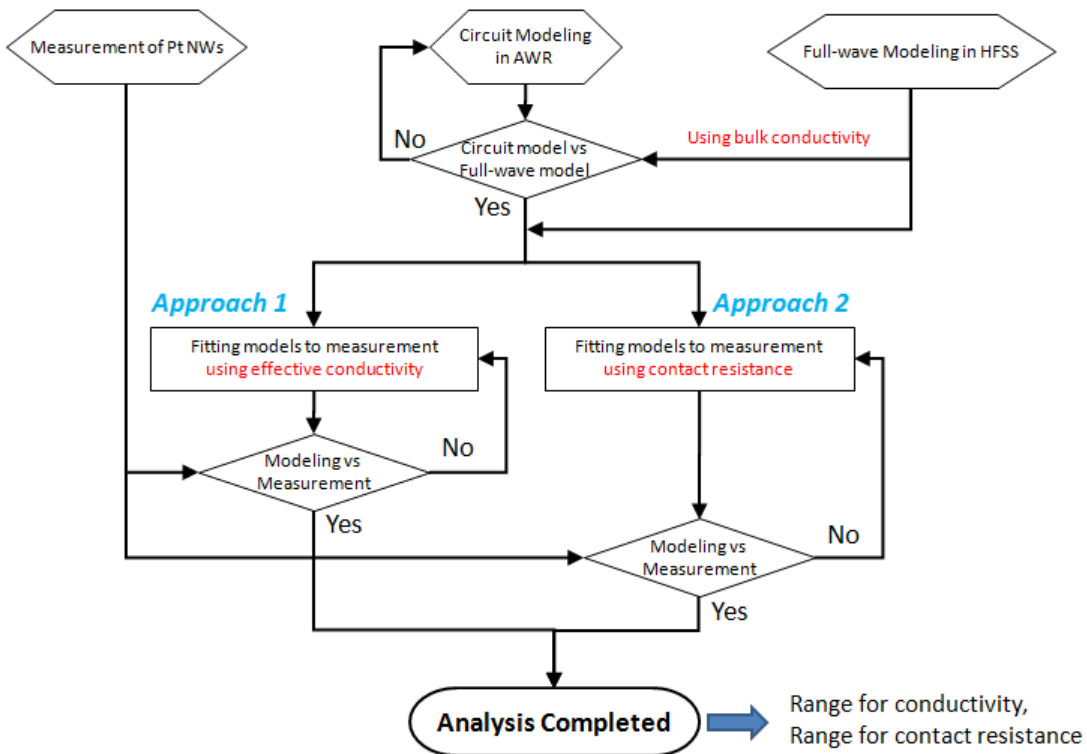


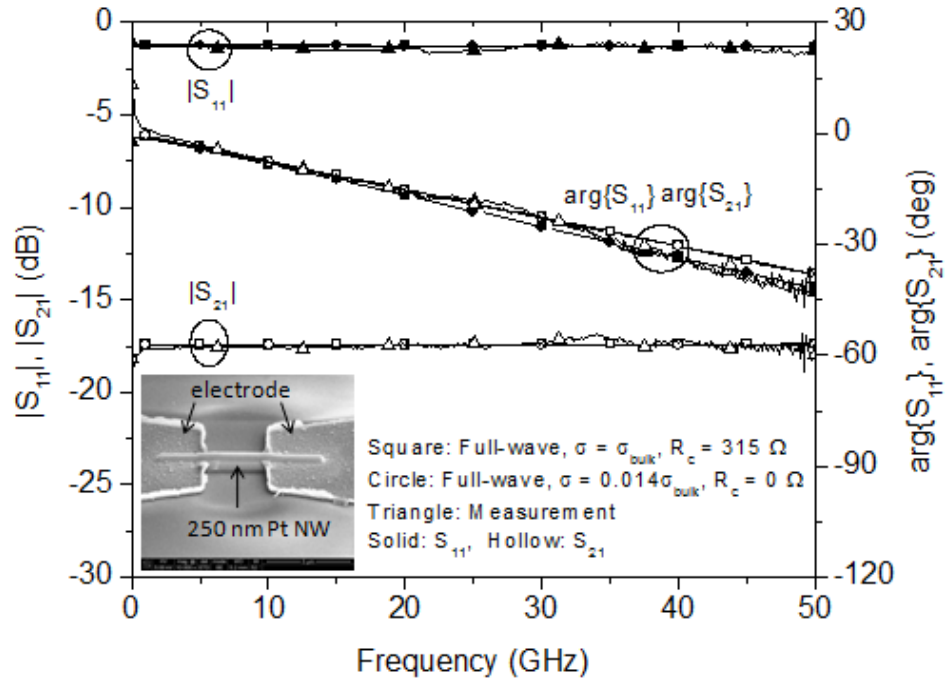
Fig. 2.12 Flow chart for the analysis approaches used to determine the interdependence between contact resistance and NW conductivity.

2.3.4. Results

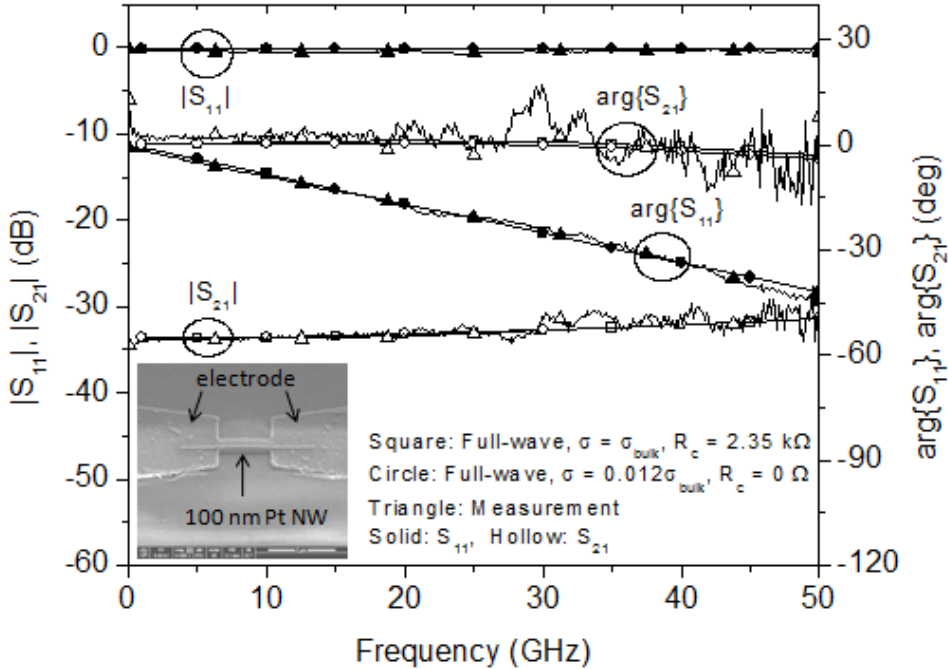
Measured and FEM simulated S-parameters for the devices with 100 and 250 nm diameters Pt NWs are shown in Fig. 2.13. For the 250 nm diameter Pt NWs in Fig. 2.13

(a), fitting the full-wave data to measurements results in the adjusted conductivity of $\sigma = 0.014\sigma_{bulk}$ when $R_c = 0 \Omega$. The second fitting produces the adjusted contact resistance of $R_c = 315 \Omega$ when $\sigma = \sigma_{bulk}$. Therefore, the range for the contact resistance and the conductivity of 250 nm Pt NWs is from 0 to 315Ω and from $0.014\sigma_{bulk}$ to σ_{bulk} , respectively. Maximum standard deviations between measurements and simulations are 1.5° for $\arg\{S_{11}\}$ and 0.3 dB for $|S_{21}|$. For the 100 nm diameter Pt NWs, shown in Fig. 2.13 (b), the minimal adjusted conductivity is found to be $\sigma = 0.012\sigma_{bulk}$, and the maximal adjusted contact resistance $R_c = 2.35 \text{ k}\Omega$. The maximum standard deviations are 1.4° , and 0.8 dB for $\arg\{S_{11}\}$ and $|S_{21}|$, respectively. As seen in both cases, the two approaches produce the same results, showing that the two parameters, the conductivity and the contact resistance, cannot be determined simultaneously. It is important to note that the obtained parameters represent the extreme values for a specific diameter Pt NW. Also the full-wave simulations guarantee that any parasitic effects are directly accounted for in the solution process, which is slightly different than the circuit simulations.

Circuit simulations with applied fitting are compared with measurements, shown in Fig. 2.14. For the 250 nm diameter Pt NW, the maximum R_c is found to be 315Ω which is the same as the full-wave result. However, the minimum conductivity is found to be $0.0165\sigma_{bulk}$, slightly larger than that obtained from the full-wave simulations. For the 100 nm diameter Pt NW, the minimum conductivity of the NW is $0.0125\sigma_{bulk}$ and the maximum R_c is $2.4 \text{ k}\Omega$, and both agree well with full-wave results as well as measurements. The maximum standard deviation of $\arg\{S_{11}\}$ is 1.8° , and that of $|S_{21}|$ is

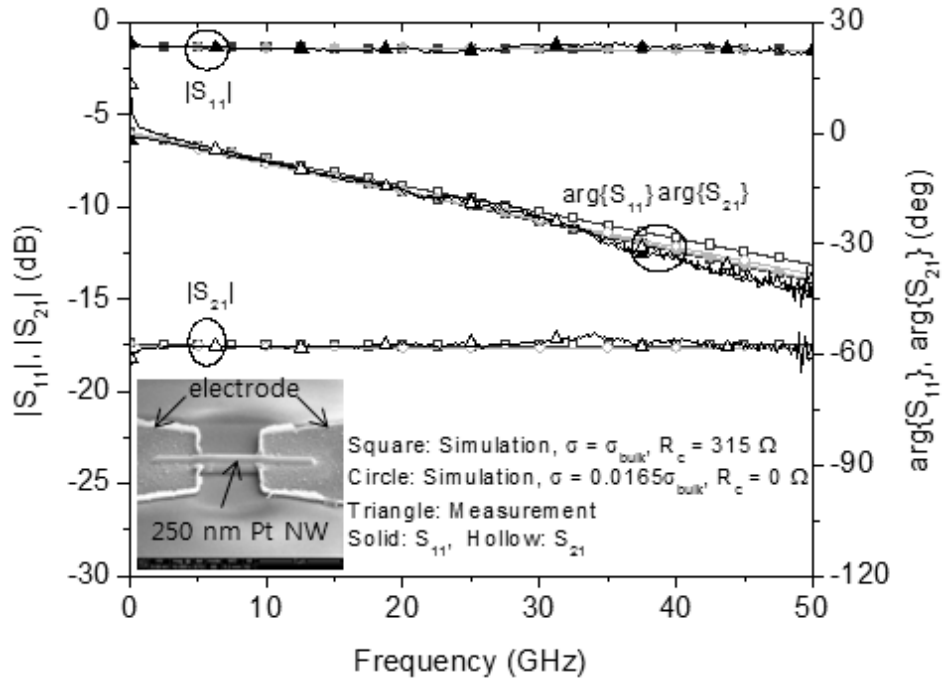


(a) Device with a 250 nm diameter Pt NW

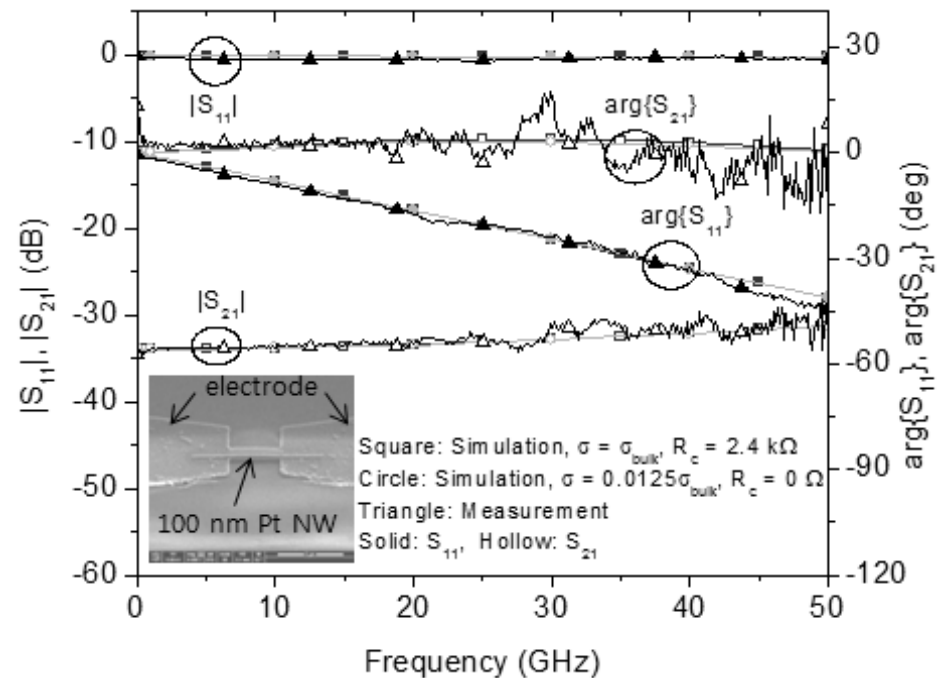


(b) Device with a 100 nm diameter Pt NW

Fig. 2.13 Measured and simulated S-parameters for the devices with Pt NWs. full-wave FEM modeling is used for the simulations. Insets: SEM images of measured device with Pt NW.



(a) Device with a 250 nm diameter Pt NW



(b) Device with a 100 nm diameter Pt NW

Fig. 2.14 Measured and simulated S-parameters for the devices with Pt NWs. Circuit modeling is used for the simulations. Insets: SEM images of measured devices with Pt NW.

1.8 dB larger than in the full-wave case as one would expect. Finally, to determine exact values for contact resistance and conductivity, additional sets of test-bed devices are needed as discussed in Section 2.4.

When either conductivity or contact resistance is determined, the other interdependent parameter can be subsequently obtained. The range for the conductivity is found to be from $0.012\sigma_{bulk}$ to σ_{bulk} and $0.014\sigma_{bulk}$ to σ_{bulk} for 100 and 250 nm diameter Pt NWs, respectively. The contact resistance is in the range of 0-2.4 k Ω and 0-315 Ω for 100 and 250 nm Pt NWs, respectively. Even though there are many solutions available within their ranges, the two parameters form a specific solution pair. The solution pairs for the 100 and 250 nm Pt NWs are plotted in Fig. 2.15. When one of the two parameters is chosen (or determined), the other can be obtained from this figure. Note that the obtained results are well correlated with relevant findings reported by other groups in [6, 19, 20]. Their results are summarized in Table 1.2.

In addition to the high frequency measurements, port-to-port DC resistances for the devices with 100 and 250 nm diameters Pt NWs are measured. Since the resistance is dominated by the Pt NWs rather than the signal line of the CPW, DC resistances for both Pt NWs can be estimated from (5-27) in [78], $(DC\ resistance) = (wire\ length) / (conductivity \times cross\ sectional\ area)$. For both cases maximum R_c and the minimum conductivity are used. Calculated and measured DC resistances are summarized in Table 2.1. As seen, the results support that both RF fitting approaches are correlated well with the DC resistance measurements. Note that the DC resistance of the signal line of the CPW is not included in calculation.

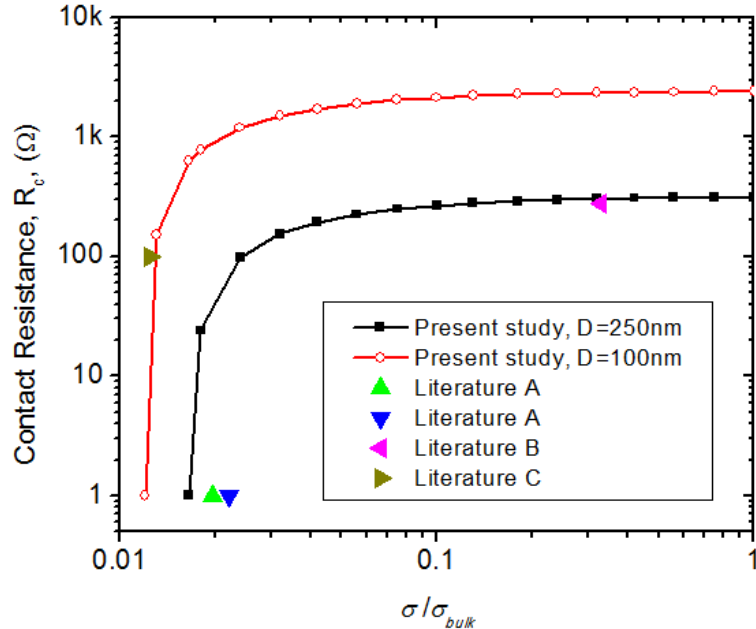


Fig. 2.15 Ranges for the conductivity of Pt NWs and the contact resistance. With one of the two parameters fix, the other can be obtained. Literature A: [19], Literature B: [6], Literature C: [20].

Table 2.1 Comparison between calculated and measured DC resistance. DC resistance of the NW is calculated from the formula, $(DC\ resistance) = (\text{wire length}) / (\text{conductivity} \times \text{cross sectional area})$. Comparisons are made with the solutions from the two approaches.

NW Diameter	$\sigma = \sigma_{bulk}$			$\sigma = 0.0125\sigma_{bulk}$ (100 nm NW) or $\sigma = 0.0165\sigma_{bulk}$ (250 nm NW)			Measured DC Resistance
	R_{NW}	R_C	$R_{NW} + 2R_C$	R_{NW}	R_C (assumed)	$R_{NW} + 2R_C$	
100 nm Pt NW	54.8 Ω	2.4 kΩ	4.85 kΩ	4.38 kΩ	0 Ω	4.38 kΩ	4.83 kΩ
250 nm Pt NW	8.8 Ω	315 Ω	639 Ω	54.8 Ω	0 Ω	531 Ω	670 Ω

2.4 Model-based Methods

In order to determine both contact resistance, R_c , and conductivity, σ , for Pt NWs with a particular diameter simultaneously, at least two devices with Pt NWs of different lengths are needed. The Pt NWs in both devices can be assumed to have the same

conductivity when the NWs are deposited in the same fabrication conditions. It is also assumed that NW's contact resistances on both sides of each device are identical. In fabrication, FIB moves back and forth from one CPW signal line to the other to deposit the Pt NW across the gap. Thus, the two contact resistances in one device may be the same. Although the contact resistance of a device may be different to that of the other devices because of uncertainties in devices and fabrication processes, this thesis focuses on a situation with four identical contact resistances (two devices, two contact resistances in each device).

This section demonstrates two model-based approaches developed to determine the conductivity and contact resistance for Pt NWs. First, an approach using a transmission line model for the NW is introduced, and its limitations and issues are discussed. Next, a method based on a lumped element model for the NW is developed. Validations for both approaches are conducted with circuit and full-wave FEM simulations. Finally, the second approach based on a lumped element model is used to analyze measurements and determine contact impedance and conductivity of Pt NWs.

2.4.1 Approach Based on Transmission Line Models

2.4.1.1 Algorithm Description

The NW is embedded as a signal line in CPW configuration, thus it can be represented by a simple transmission line model. The line between two contacts, R_c , is characterized with characteristic impedance, Z_c , and propagation constant, γ , as shown in Fig. 2.16. Assuming that the two contact resistances are identical and that R_c is

constant for a particular diameter of Pt NWs, Z_c and γ should be maintained independent on the length of the NWs. In other words, there is a condition for the solutions of σ and R_c for the NW, in which both Z_{c1} and γ_1 equal to Z_{c2} and γ_2 for two different lengths l_1 and l_2 , respectively. To solve this problem, we start by converting two-port S-parameters into ABCD matrix [74].

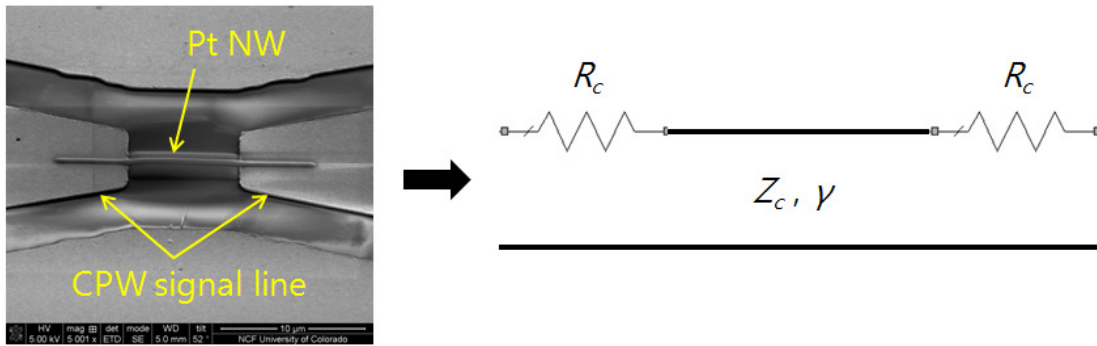


Fig. 2.16 SEM image of Pt NW and its equivalent model based on transmission line theory. The NW is modeled with a transmission line having characteristic impedance Z_c and propagation constant γ . Contact resistance, R_c , is connected at both ends of the NW.

S-parameters for the device with a Pt NW, $[S]_{\text{tot}}$, and those for the device without the NW, $[S]_{\text{empty}}$, are measured at the position of the taper end (between ordinary CPW and tapered CPW lines). This is possible by moving reference planes using NISTcal [75]. Each S-parameter set is converted to a Y-matrix as $[Y]_{\text{tot}}$ and $[Y]_{\text{empty}}$, using matrix conversion [74]. Assuming the NW and contacts are in parallel with the gap reactance, $[Y]_{\text{NW+Rc}}$ for the NW and the contact resistance (shown in Fig. 2.16) is obtained as

$$[Y]_{\text{NW+Rc}} = [Y]_{\text{tot}} - [Y]_{\text{empty}}. \quad (2.1)$$

Using matrix conversion again, $[Y]_{NW+R_c}$ is converted to ABCD matrix, $[ABCD]_{NW+R_c}$, to find the characteristic impedance, Z_c , and propagation constant, γ for the NW section, and contact resistance, R_c . Since the two contact resistances and the NW are connected in series, $[ABCD]_{NW+R_c}$ can be represented as,

$$\begin{aligned} [ABCD]_{NW+R_c} &= \begin{bmatrix} 1 & R_c \\ 0 & 1 \end{bmatrix} \cdot [ABCD]_{NW} \cdot \begin{bmatrix} 1 & R_c \\ 0 & 1 \end{bmatrix} \\ &= \begin{bmatrix} 1 & R_c \\ 0 & 1 \end{bmatrix} \cdot \begin{bmatrix} \cosh(\gamma l) & Z_0 \sinh(\gamma l) \\ \frac{1}{Z_0} \sinh(\gamma l) & \cosh(\gamma l) \end{bmatrix} \cdot \begin{bmatrix} 1 & R_c \\ 0 & 1 \end{bmatrix}, \end{aligned} \quad (2.2)$$

and the ABCD matrix for the NW is as follows,

$$\begin{aligned} [ABCD]_{NW} &= \begin{bmatrix} \cosh(\gamma l) & Z_0 \sinh(\gamma l) \\ \frac{1}{Z_0} \sinh(\gamma l) & \cosh(\gamma l) \end{bmatrix} \\ &= \begin{bmatrix} 1 & R_c \\ 0 & 1 \end{bmatrix}^{-1} \cdot [ABCD]_{NW+R_c} \cdot \begin{bmatrix} 1 & R_c \\ 0 & 1 \end{bmatrix}^{-1}. \end{aligned} \quad (2.3)$$

$[ABCD]_{NW+R_c}$ is obtained from measurements, and (2.3) can be rewritten as,

$$\begin{aligned} \begin{bmatrix} A_{NW} & B_{NW} \\ C_{NW} & D_{NW} \end{bmatrix} &= \begin{bmatrix} 1 & -R_c \\ 0 & 1 \end{bmatrix} \cdot \begin{bmatrix} A_{meas} & B_{meas} \\ C_{meas} & D_{meas} \end{bmatrix} \cdot \begin{bmatrix} 1 & -R_c \\ 0 & 1 \end{bmatrix} \\ &= \begin{bmatrix} A_{meas} - R_c C_{meas} & R_c^2 C_{meas} - R_c A_{meas} + B_{meas} - R_c D_{meas} \\ C_{meas} & D_{meas} - R_c C_{meas} \end{bmatrix} \end{aligned} \quad (2.4)$$

where $[ABCD]_{\text{NW}} = \begin{bmatrix} A_{\text{NW}} & B_{\text{NW}} \\ C_{\text{NW}} & D_{\text{NW}} \end{bmatrix}$ and $[ABCD]_{\text{NW+Rc}} = \begin{bmatrix} A_{\text{meas}} & B_{\text{meas}} \\ C_{\text{meas}} & D_{\text{meas}} \end{bmatrix}$. From (2.3),

characteristic impedance and propagation constant for the NW can be found as,

$$Z_c = \sqrt{\frac{B_{\text{NW}}}{C_{\text{NW}}}}, \quad (2.5)$$

$$\gamma = \frac{1}{l} \ln \left(A_{\text{NW}} \pm \sqrt{A_{\text{NW}}^2 - 1} \right), \quad (2.6)$$

where $\text{Re}\{\gamma\} > 0$. For two different line lengths l_1 and l_2 , the characteristic impedance and propagation constant can be obtained from (2.4) through (2.6) as,

$$Z_{c1} = \frac{C_{\text{meas1}} R_c^2 - (A_{\text{meas1}} + D_{\text{meas1}}) R_c + B_{\text{meas1}}}{C_{\text{meas1}}}, \quad (2.7)$$

$$Z_{c2} = \frac{C_{\text{meas2}} R_c^2 - (A_{\text{meas2}} + D_{\text{meas2}}) R_c + B_{\text{meas2}}}{C_{\text{meas2}}}, \quad (2.8)$$

$$\gamma_1 = \frac{1}{l_1} \ln \left(A_{\text{meas1}} - R_c C_{\text{meas1}} \pm \sqrt{(A_{\text{meas1}} - R_c C_{\text{meas1}})^2 - 1} \right), \quad (2.9)$$

$$\gamma_2 = \frac{1}{l_2} \ln \left(A_{\text{meas2}} - R_c C_{\text{meas2}} \pm \sqrt{(A_{\text{meas2}} - R_c C_{\text{meas2}})^2 - 1} \right). \quad (2.10)$$

Subscripts 1 and 2 denote the line lengths l_1 and l_2 , respectively. When a condition $Z_{c1} = Z_{c2}$ is satisfied, then contact resistance is found as,

$$R_c = \text{Re} \left\{ \frac{B_{\text{meas}2}C_{\text{meas}1} - B_{\text{meas}1}C_{\text{meas}2}}{C_{\text{meas}1}(A_{\text{meas}2} + D_{\text{meas}2}) - C_{\text{meas}2}(A_{\text{meas}1} + D_{\text{meas}1})} \right\}. \quad (2.11)$$

Note that contact impedance also can be obtained from (2.11), since the ABCD matrix contains complex numbers. For another condition $\gamma_1 = \gamma_2$, (2.9) and (2.10) are logarithmic equations with complex numbers, which cannot be solved analytically. Instead, an approximation

$$\cosh(x) = 1 + \frac{x^2}{2!} + \frac{x^4}{4!} + \frac{x^6}{6!} + \dots \approx 1 + \frac{x^2}{2!} \quad (2.12)$$

can be taken up to the quadratic term for (2.3). Thus, from (2.3) and (2.4),

$$\begin{aligned} A_{\text{NW}} &= A_{\text{meas}} - R_c C_{\text{meas}} \\ &= \cosh(\gamma l) \approx 1 + \frac{(\gamma l)^2}{2}. \end{aligned} \quad (2.13)$$

Therefore, the resulting propagation constant is

$$\gamma = \frac{1}{l} \sqrt{2(A_{\text{meas}} - R_c C_{\text{meas}} - 1)}, \quad (2.14)$$

and the condition for propagation constant, $\gamma_1 = \gamma_2$, results in

$$R_c = \text{Re} \left\{ \frac{l_1^2 (A_{\text{meas}2} - 1) - l_2^2 (A_{\text{meas}1} - 1)}{l_1^2 C_{\text{meas}2} - l_2^2 C_{\text{meas}1}} \right\}. \quad (2.15)$$

One can determine R_c by the use of either (2.11) or (2.15). Then, the characteristic impedance and the propagation constant for the NW sections in the two devices are found from (2.7) to (2.10).

Conductivity of the Pt NW can be computed from the characteristic impedance and the propagation constant of the NW section. The NW section can be represented with lumped elements: resistance per unit length R' , inductance per unit length L' , conductance per unit length G' , and capacitance C' per unit length. Z_c and γ are rewritten as;

$$Z_c = \sqrt{\frac{R' + j\omega L'}{G' + j\omega C'}}, \quad (2.16)$$

$$\gamma = \sqrt{(R' + j\omega L')(G' + j\omega C')}. \quad (2.17)$$

From (2.16) and (2.17), resistance per unit length for the NW section is

$$R' = \operatorname{Re}\{Z_c \cdot \gamma\} \text{ } (\Omega/\text{m}). \quad (2.18)$$

R' takes into account resistances of the Pt NW and ground metallization. Resistance of the ground layer is not simple to calculate because of a lack of detailed information about its dimensions. The ground layer is made from Au, the bulk conductivity of which is $4.1 \times 10^7 \text{ S/m}$ and about 4.4 times the bulk conductivity of Pt ($9.3 \times 10^6 \text{ S/m}$). If the conductivity of the Pt NW is smaller than its bulk conductivity, one can assume that the resistance of the Pt NW, R_{nw} , is the dominant contribution to R' . Thus, R' can be approximated to R_{nw} and represented as,

$$(1 \text{ m}) \cdot R' \approx R_{nw} = \frac{1}{\pi \cdot r \cdot \sigma} \text{ } (\Omega). \quad (2.19)$$

Formula (2.19) describes the DC resistance of a 1 m-long round wire with a radius r and conductivity σ . Even though this thesis characterizes Pt NWs at high frequencies, (2.19) is valid because the skin depth, δ , of Pt at 10 GHz is about $1.6 \mu\text{m}$, and it is much larger than the NW's radius. As seen in Fig. 2.17, current distribution is almost constant throughout the cross section of the round wire when $\sqrt{2}r/\delta = 0.1$ [79]. For the Pt NW with 250 nm diameter at 10 GHz, the factor, $\sqrt{2}r/\delta$, is 0.107, thus the current

distribution in Pt NWs is considered uniform. Therefore, the conductivity of the Pt NW is obtained from (2.19) as,

$$\sigma = \frac{1}{\pi \cdot r^2 \cdot R} = \frac{1}{\pi \cdot r^2 \cdot \text{Re}\{Z_c \cdot \gamma\}} \quad (2.20)$$

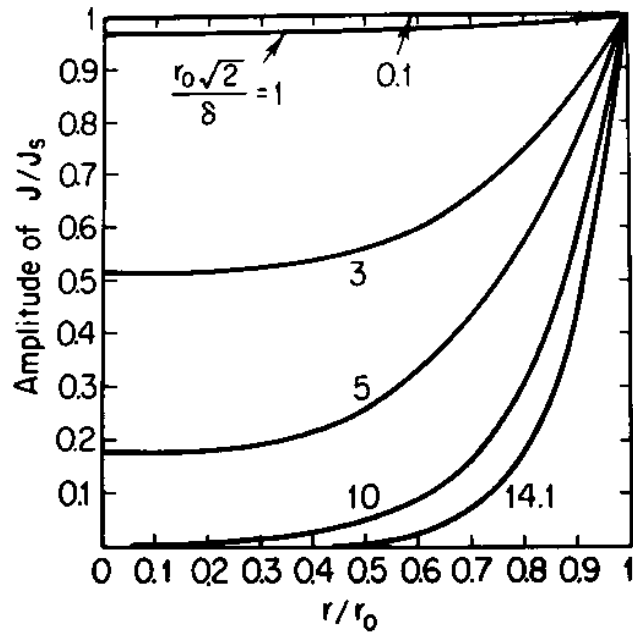


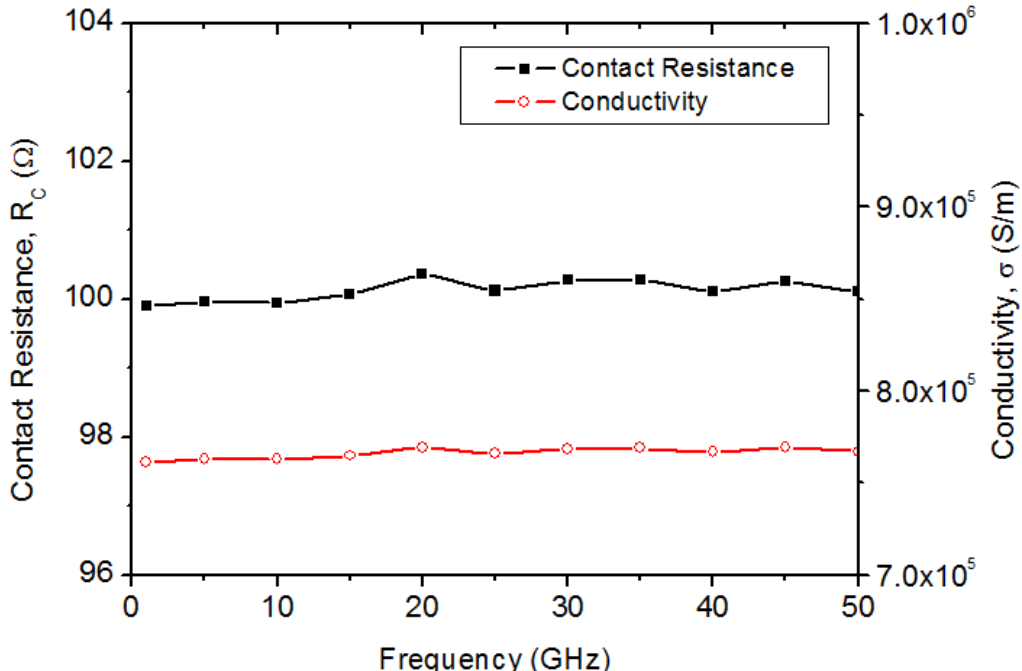
Fig. 2.17 Theoretical current distribution in a solid round wire, reproduced from [79]. J : current density in a wire, J_s : surface current density, r : radius within the wire, r_0 : outer radius of the wire, and δ : skin depth. Note that, when $\sqrt{2} r_0 / \delta = 0.1$, current distribution is uniform throughout the cross section of the wire.

2.4.1.2 Validation

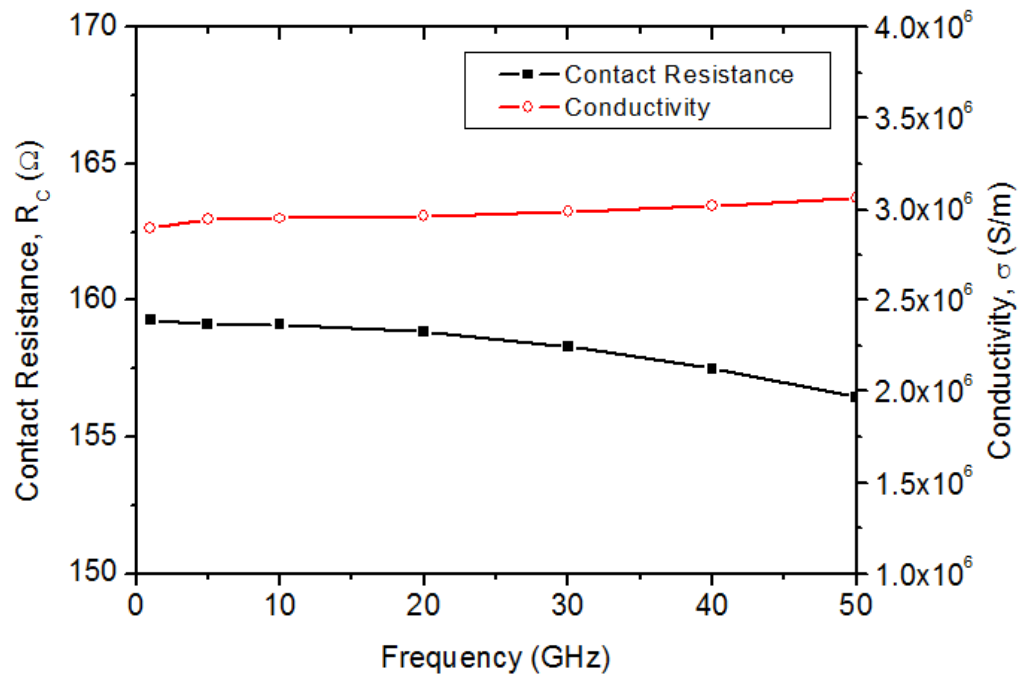
Validations for the above approach with the 250 nm diameter Pt NW are conducted using circuit and full-wave FEM based test-beds. Simulations are performed

using models described in Section 2.3. NW's lengths are chosen as 4 and 8 μm . Contact resistance and conductivity are set at $R_c = 100 \Omega$ and $\sigma = 9.3 \times 10^5 \text{ S/m}$ (ten times lower than its bulk conductivity). Obtained results for R_c and σ are plotted in Fig. 2.18 (a) and (b), respectively. As seen, the contact resistance obtained from circuit simulations agrees very well with the preset value. However, the extracted conductivity has about 17 % error which is likely due to the approximation in (2.19).

Obtained contact resistance and conductivity from the full-wave FEM simulations are very different from their preset values in Fig 2.18 (b). Because conductivity is depending on contact resistance in the formulations given in (2.20) and (2.7)-(2.10), a large error in conductivity is added due to incorrect contact resistance. The reason for incorrect contact resistance can be deduced from the non-TEM mode in the gap, as shown in Fig. 2.19, which, in a transmission line model, is assumed to be of TEM nature. However, electric fields normal to the metal surface in the gap are parallel with the NW for a few μm of the NW's length, as shown in the figure. These electric fields induce on-axis currents in the NW, so that some amount of NW's resistance, $R_{nw'}$, is included in the contact resistance, and not into the resistance per unit length of the NW CPW line. Therefore, resulting R_c from this approach is $R_c + R_{nw'}$, while resistance per unit length of the NW CPW line is $R_{nw} - R_{nw'}$. The effective length for $R_{nw'}$ may be about 2.5 μm since $(2.5 \mu\text{m}) / (\pi \cdot r^2 \cdot \sigma) = 55 \Omega$. When longer NWs are used, for example 16 and 20 μm , $R_{nw'}$ increases to about 80 Ω , indicating that using longer NWs cannot remove the effect of $R_{nw'}$. Note that higher conductivity can reduce this effect. For example, if ten times higher $\sigma (9.3 \times 10^6 \text{ S/m})$ is used, $R_{nw'}$ decreases to the one tenth of the above



(a) Results from circuit simulations



(b) Results from full-wave FEM simulations

Fig. 2.18 Computed R_c and σ from the transmission line model-based approach and (a) circuit and (b) full-wave FEM simulations. Preset contact resistance and conductivity are $R_c = 100 \Omega$ and $\sigma = 9.3 \times 10^5 \text{ S/m}$, respectively.

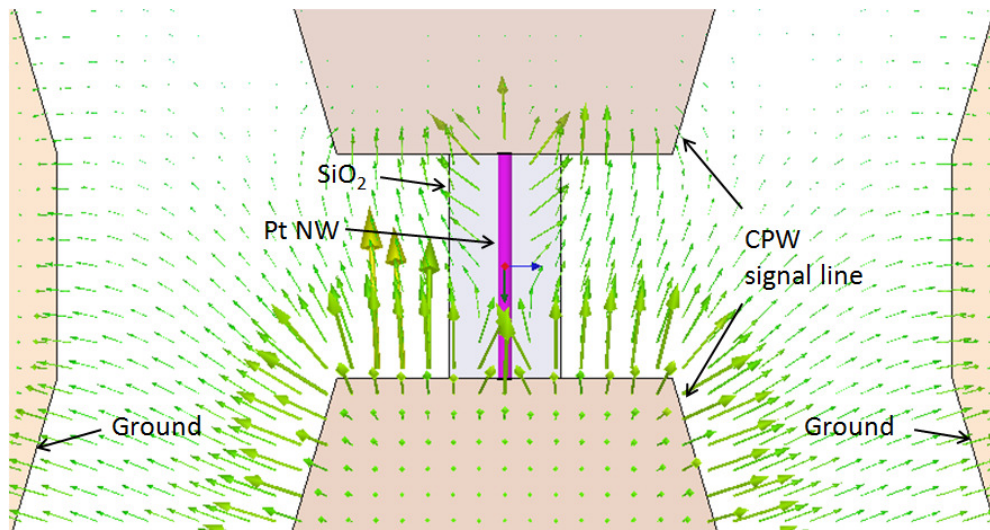


Fig. 2.19 Simulated electric field distribution around Pt NW using HFSS. The gap distance is $4 \mu\text{m}$. Note that the field distribution is not that of a TEM mode in the gap.

values. In fact, this phenomenon can happen in conventional transmission lines with ‘stepped’ discontinuity along the line. However, those lines are typically made from good conductors such as Cu or Au, and their R_{nw} is negligible.

In summary, the computational studies for the transmission line model-based approach show that the contact resistance can be determined accurately with circuit models, but the obtained conductivity is inaccurate. Based on the error seen with the full-wave models, this approach is deemed to be not very accurate and should not be further developed.

2.4.2 Lumped Element Based Approach

2.4.2.1 Algorithm Description

The Pt NW is modeled as an equivalent two-port T-network to represent symmetric nature of the device and appropriate loss mechanism, as shown in Fig. 2.20.

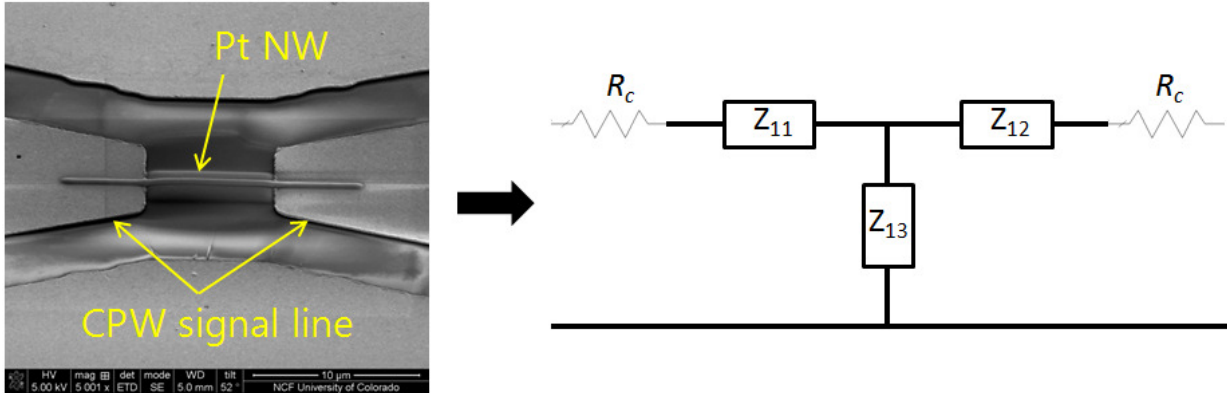


Fig. 2.20 SEM image of Pt NW and equivalent two-port T-network for Pt NWs with length l_1 . Series impedances Z_{11} and Z_{12} represent impedance of the Pt NW. Shunt impedance Z_{13} is impedance between the Pt NW and ground.

Series impedances Z_{11} and Z_{12} arising from conduction currents are one half of the NW's impedance ($Z_{11} = Z_{12}$) for the length of l_1 . Shunt impedance Z_{13} is included due to displacement currents between the NW and ground. For the length of l_2 , the series impedances Z_{21} and Z_{22} ($= Z_{21}$) and shunt impedance Z_{23} can be used. The relationships between impedances for the two lengths are as follows;

$$\frac{Z_{11}}{l_1} = \frac{Z_{21}}{l_2}, \quad (2.21)$$

and

$$Z_{13} \cdot l_1 = Z_{23} \cdot l_2. \quad (2.22)$$

Since the T-network of the model in Fig. 2.20 is represented with ABCD matrix as

[74],

$$[ABCD]_{NW} = \begin{bmatrix} 1 + \frac{Z_{11}}{Z_{13}} & 2Z_{11} + \frac{Z_{11}^2}{Z_{13}} \\ \frac{1}{Z_{13}} & 1 + \frac{Z_{11}}{Z_{13}} \end{bmatrix}, \quad (2.23)$$

the model for the NW with length of l_1 is,

$$\begin{aligned} [ABCD]_{NW+Rc,1} &= \begin{bmatrix} 1 & R_c \\ 0 & 1 \end{bmatrix} \cdot [ABCD]_{NW,1} \cdot \begin{bmatrix} 1 & R_c \\ 0 & 1 \end{bmatrix} \\ &= \begin{bmatrix} 1 & R_c \\ 0 & 1 \end{bmatrix} \cdot \begin{bmatrix} 1 + \frac{Z_{11}}{Z_{13}} & 2Z_{11} + \frac{Z_{11}^2}{Z_{13}} \\ \frac{1}{Z_{13}} & 1 + \frac{Z_{11}}{Z_{13}} \end{bmatrix} \cdot \begin{bmatrix} 1 & R_c \\ 0 & 1 \end{bmatrix}, \end{aligned} \quad (2.24)$$

and

$$\begin{aligned} &\begin{bmatrix} 1 + \frac{Z_{11}}{Z_{13}} & 2Z_{11} + \frac{Z_{11}^2}{Z_{13}} \\ \frac{1}{Z_{13}} & 1 + \frac{Z_{11}}{Z_{13}} \end{bmatrix} \\ &= \begin{bmatrix} A_{meas1} - R_c C_{meas1} & R_c^2 C_{meas1} - R_c (A_{meas1} + D_{meas1}) + B_{meas1} \\ C_{meas1} & D_{meas1} - R_c C_{meas1} \end{bmatrix}, \end{aligned} \quad (2.25)$$

where $[ABCD]_{NW+R_c,1} = \begin{bmatrix} A_{\text{meas1}} & B_{\text{meas1}} \\ C_{\text{meas1}} & D_{\text{meas1}} \end{bmatrix}$ is obtained from measurements. From (2.25),

impedances associated with the model are found as,

$$Z_{13} = \frac{1}{C_{\text{meas1}}}, \quad (2.26)$$

and

$$Z_{11} = \frac{A_{\text{meas1}} - R_c C_{\text{meas1}} - 1}{C_{\text{meas1}}}. \quad (2.27)$$

Z_{21} and Z_{23} for the NW with length l_2 can be obtained the same way using and expressions (2.27) and (2.26), respectively. The contact resistance, R_c , can be determined by substituting (2.27) for the two lengths l_1 and l_2 (using the subscript 2 instead of 1) into (2.21) as,

$$R_c = \text{Re} \left\{ \frac{l_2 C_{\text{meas2}} (A_{\text{meas1}} - 1) - l_1 C_{\text{meas1}} (A_{\text{meas2}} - 1)}{(l_2 - l_1) C_{\text{meas1}} C_{\text{meas2}}} \right\}. \quad (2.28)$$

Note that contact impedance (not only resistance) can also be found from (2.28) because the ABCD matrix is complex, similar to (2.11). Since the NW's resistance is a real part of

Z_{11} or Z_{21} , conductivity of the Pt NW can be determined using the formula for the DC resistance of a round wire (2.19) as,

$$\sigma = \frac{l_1}{2\pi \cdot r^2 \cdot \text{Re}\{Z_{11}\}} \text{ or } \frac{l_2}{2\pi \cdot r^2 \cdot \text{Re}\{Z_{21}\}}. \quad (2.29)$$

The factor of 1/2 is used due to the fact that Z_{11} (or Z_{21}) is impedance of the NW with a half length of l_1 (or l_2).

2.4.2.2 Validation

Validation is conducted with circuit and full-wave simulations. The circuit model for the device with Pt NWs is shown in Fig. 2.21. As seen, the model from Fig. 2.11 is modified by replacing a “CPW line” component with a “round wire” component. The wire component can be defined with its dimensions (wire length and diameter) and conductivity. Other components are the same as in Fig. 2.11. There are no changes in the full-wave FEM models. The contact resistance and NW’s conductivity are set at $R_c = 100 \Omega$ and $\sigma = 9.3 \times 10^5 \text{ S/m}$, the same as Section 2.4.1.2.

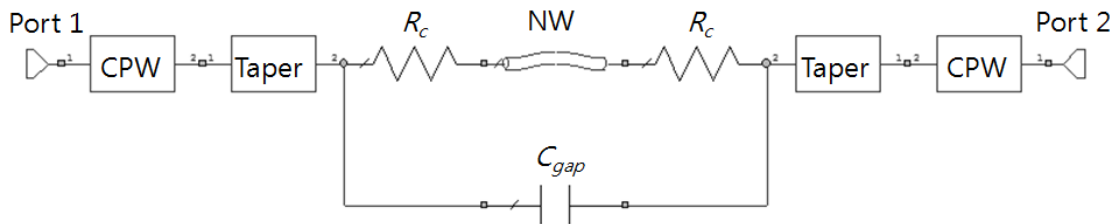
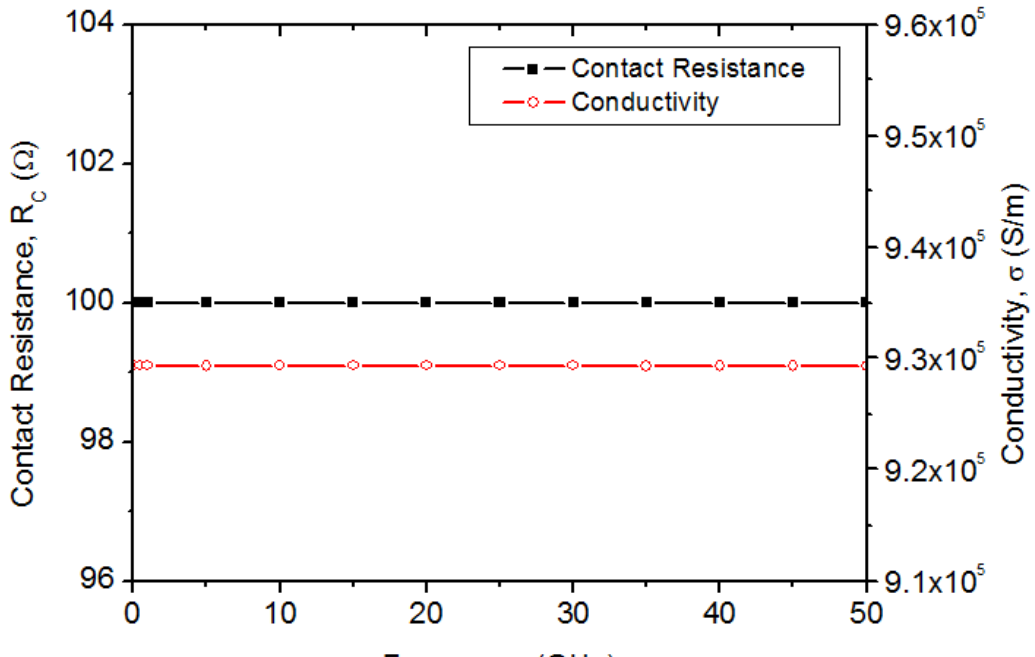


Fig. 2.21 Circuit model representing lumped element-based approach for the device with Pt NW. The Pt NW is modeled as a round wire component from the AWR library.

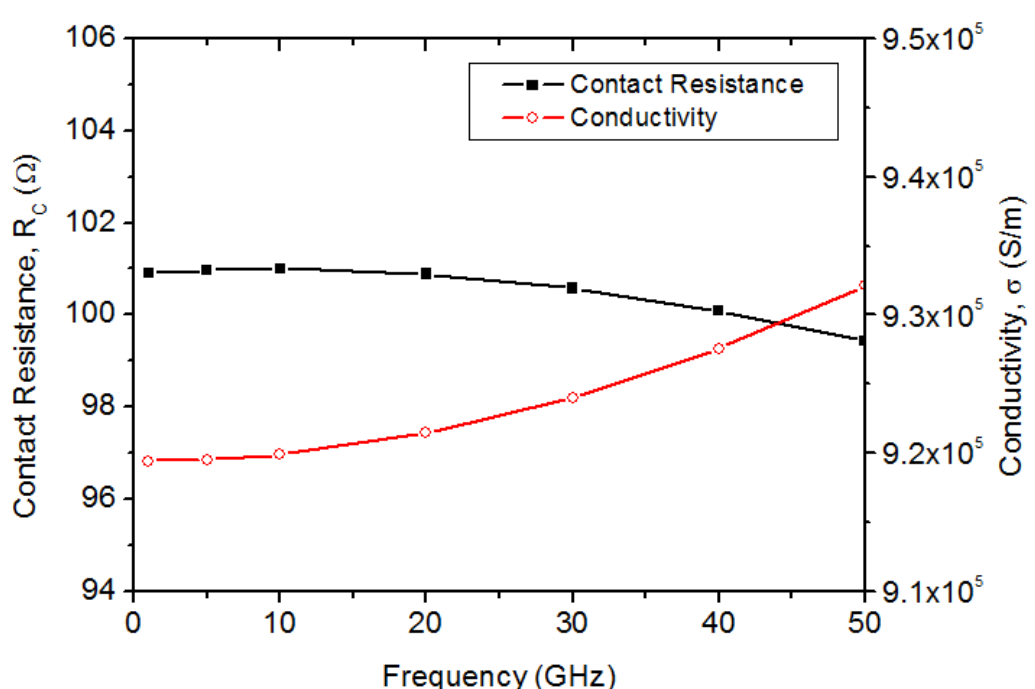
Extracted contact resistance and conductivity of the Pt NW from the lumped element-based models are shown in Fig. 2.22. Note that for clarify the results from circuit and full-wave simulations are separately plotted. As seen, the obtained R_c and σ are well correlated with their preset values for both circuit and full-wave simulations. Less than 1 Ω error for R_c in Fig. 2.22 (b) is observed, and it is likely caused by the tapered CPW line. For the full-wave simulations, the reference planes for simulated S-parameters are assumed to be at the ends of the tapered CPW lines (between constant cross-section CPW and tapered CPW lines). This setup is the same as measurements because the reference planes can be moved up to those positions along the constant cross-section CPW lines. Inherent resistance of the tapered CPW lines may be included in the obtained R_c . Also, stray fields between the two tapered CPW lines may affect R_c . The results clearly demonstrate that this approach is more accurate than the approach from Section 2.4.1. Therefore, the measurements of the fabricated Pt NW test sets are used with the lumped element-based approach.

2.4.3 Experimental Results

Test sets with the devices with Pt NWs with different lengths are fabricated as shown in Fig. 2.23. Each column contains different gap or Au short distances (4, 6, 8, 12, 16, and 20 μm) in the middle of the CPW devices. Pt NWs are deposited on the devices in rows 0 through 4. The devices in rows 5 and 6 are “the empty devices”, while those in rows 7 through 9 are the devices with “Au short”. CPW signal lines and ground are metalized with 200 nm-thick Au on a 500 μm -thick quartz substrate. Lengths of the



(a) Results from circuit simulations



(b) Results from full-wave FEM simulations

Fig. 2.22 Computed R_c and σ from the lumped element-based algorithm using (a) circuit and (b) full-wave FEM models. Preset contact resistance and conductivity are $R_c = 100 \Omega$ and $\sigma = 9.3 \times 10^5 \text{ S/m}$, respectively.

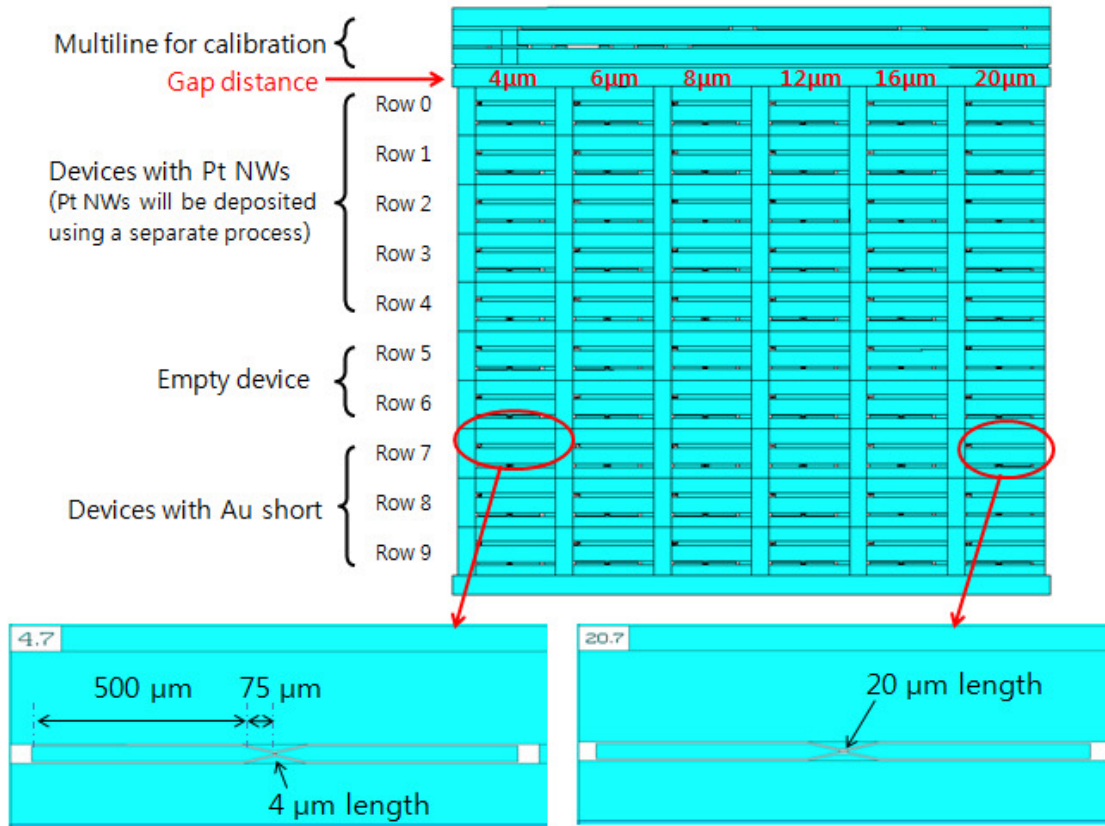


Fig. 2.23 Chip layout for measurements of Pt NWs with different lengths.

CPW line and tapered line are 500 and 75 μm , respectively. A GND 2 configuration investigated in Section 2.2.1 is used for all devices.

To experimentally validate the lumped element-based approach, the devices with Au short are measured, and their measured data are fed to a Matlab based code for the algorithm. Since the CPW signal lines are made from a uniform Au layer, the contact impedance is $R_c = 0 \Omega$. Also, the conductivity of the Au short should be the same as the bulk value ($4.1 \times 10^7 \text{ S/m}$) at low frequencies. Measured mean values and standard deviations of R_c and σ for devices with 4 and 8 μm -long Au shorts are shown in Fig. 2.24. Three sets of devices with Au short and two sets of empty devices with the

two lengths are measured, resulting in total of 36 combinations. As seen, obtained R_c is smaller than 1 Ω . The error is likely caused by the tapered CPW lines (see Section 2.4.2.2). Obtained conductivities for the Au short at around 3 GHz are close to the expected value of 4.1×10^7 S/m. Differences from expected value may be due to calibration. The results (specifically, standard deviations) at higher frequencies (> 20 GHz) are contaminated by the measurement noise. The results show that the extracted conductivity is more sensitive than the contact impedance. Next, devices with Pt NWs are measured and analyzed.

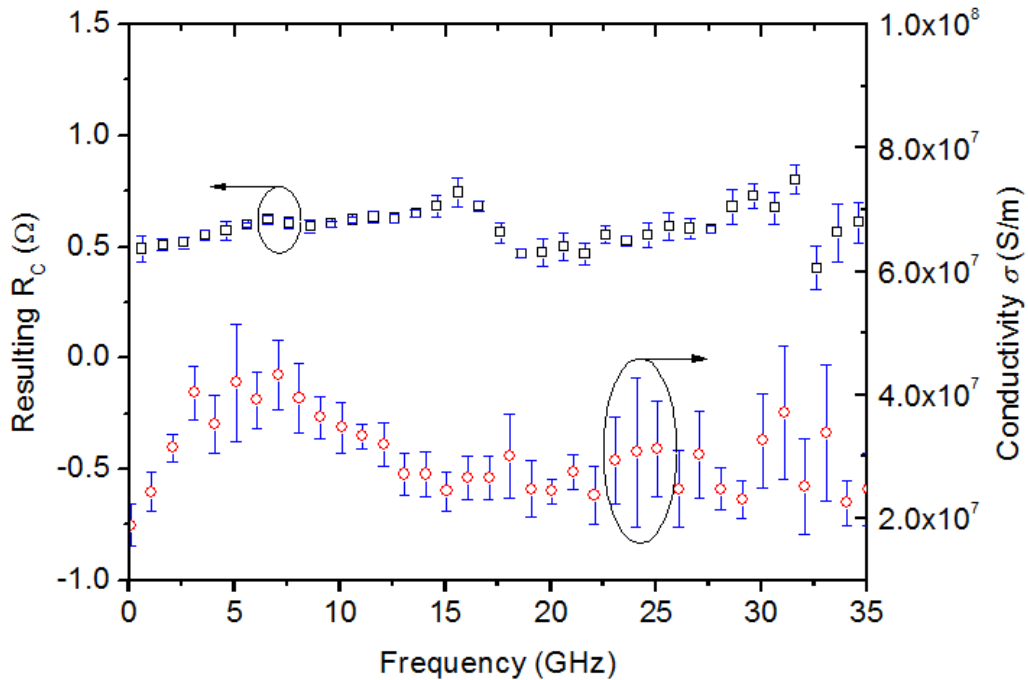


Fig. 2.24 Measured mean values and standard deviations for R_c and σ of Au short devices. Values are obtained using lumped element-based algorithm. Total of 36 different sets of the devices are used to obtain these statistics.

Ten Pt NWs are deposited on the devices with 4 and 8 μm gaps as shown in Fig. 2.25. The widths of the deposited Pt NWs are measured to be about 300 nm. NW's lengths are measured carefully since the R_c is dependent on the two lengths (see (2.28)). Even though the NW and signal lines are overlapping for about 3 μm , NW's lengths do not take into account this overlapping distance. Because the NWs are highly resistive, the majority of power flow is along Au signal lines and to the NW via the ends of the signal lines. Measured lengths are listed in Table 2.2.

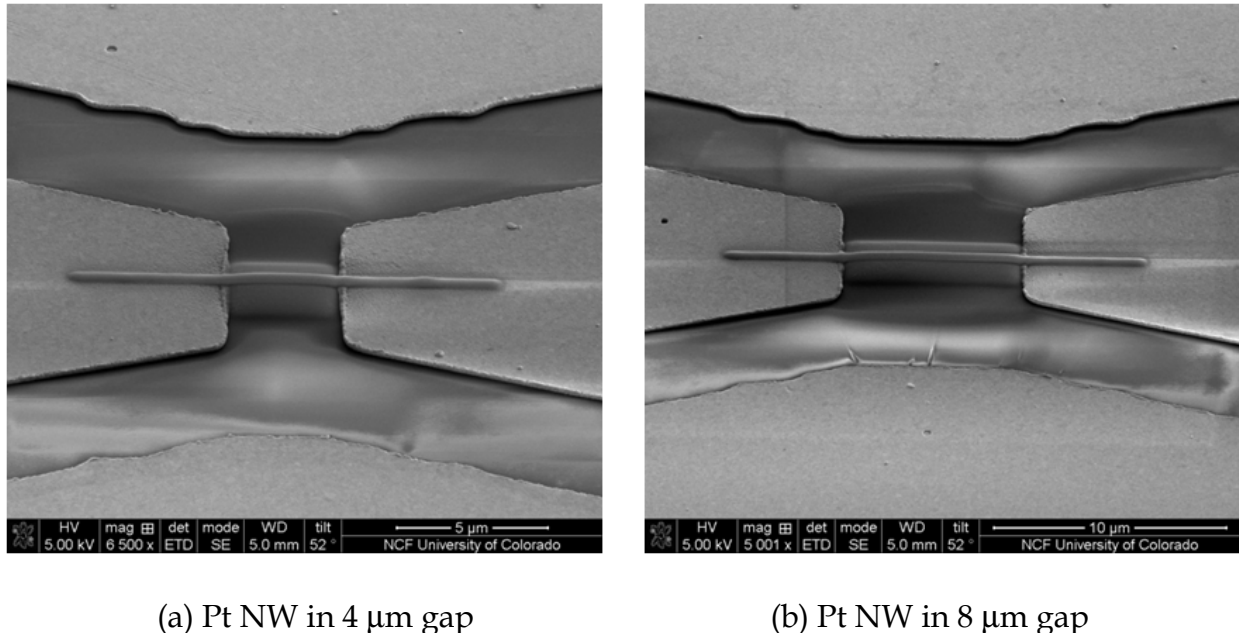


Fig. 2.25 SEM images of Pt NWs embedded in the 4 and 8 μm gaps of devices.

Table 2.2 Measured lengths of Pt NWs with overlapping distance between the NW and CPW signal lines ignored.

Device No.	NW's Length (μm)				
	DUT1	DUT2	DUT3	DUT4	DUT5
4 μm Gap	4.50	4.03	4.03	4.17	3.86
8 μm Gap	8.04	8.11	8.04	8.04	8.07

Measured mean values and standard deviations for R_c and σ for Pt NWs under test are shown in Fig. 2.26. The statistic results are obtained by processing 100 combinations with five devices with Pt NWs and two empty devices for each length (4 and 8 μm). As seen, R_c is measured to be about 50 Ω , and σ is about $0.013\sigma_{bulk}$. Note that the obtained R_c is lower than the reported values in the literature [6, 20, 22] (see Table 1.2). Measured resistivity is about 827 $\mu\Omega\cdot\text{cm}$, which is close to the results, 860-3078 $\mu\Omega\cdot\text{cm}$, of [20]. The low conductivity is due to effects of contaminants and NW's small size. Elemental analysis shows that the Pt NWs in this study have approximately 60% Pt, 34% C, and 6% Ga. In [20], Pt NWs were fabricated with 31% Pt, 10% C, and 50% Ga, in

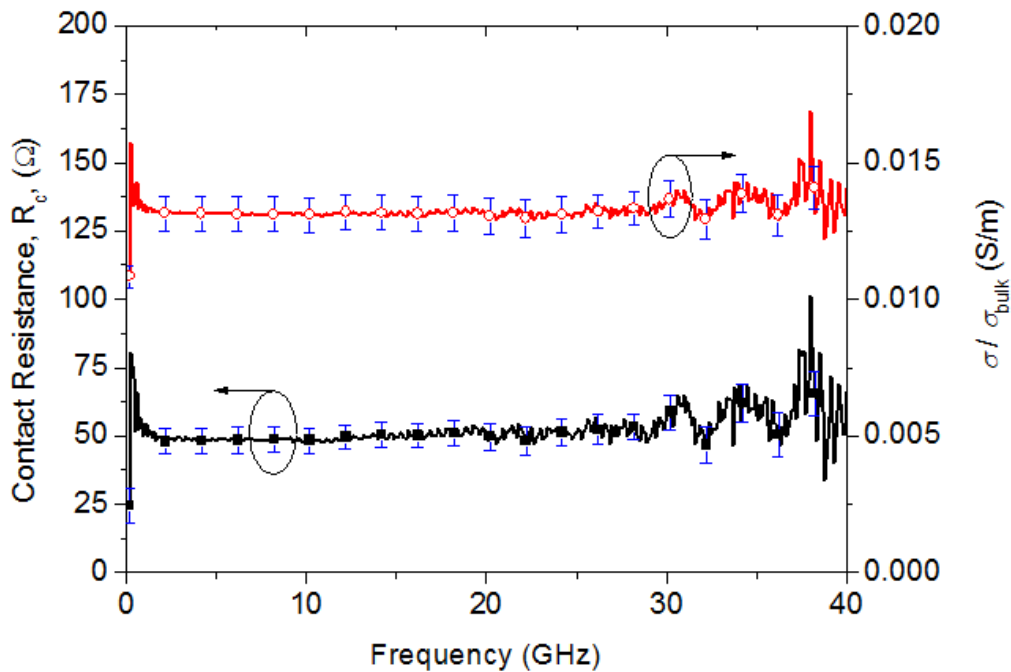


Fig. 2.26 Measured mean values and standard deviations for R_c and σ of 300 nm diameter Pt NWs. Values are obtained using lumped element-based algorithm. Total of 100 different sets of the devices are used to obtain these statistics.

reasonable agreement with the results from the present study since the Pt NWs in [20] have less Pt atoms and higher resistivity is this expected. An upturn observed at low frequencies (less than 2.5 GHz) is due to poorly calibrated S-parameter measurements in the frequency range. It is expected that errors in this range can be reduced by recalibration with longer calibration standards. The conductivity is computed assuming a circular 300 nm diameter cross-section of the NWs. Based on the results in Fig. 2.26, the total resistances of the NWs for 4 and 8 μm lengths including two contact resistances are 568Ω and 1036Ω , respectively. This is well correlated with measured DC resistance of the devices, listed in Table 2.3.

Table 2.3 Measured DC resistances including NW's resistance, two contact resistances, and resistance of CPW signal lines.

Device No.	DC Resistance (Ω)				
	DUT1	DUT2	DUT3	DUT4	DUT5
4 μm-long Gap	616	561	561	588	547
8 μm-long Gap	1009	1029	1013	1022	1025

CHAPTER 3

CHARACTERIZATION OF PLATINUM NANOWIRES (II) – CONTACTLESS APPROACH

The conductivity and contact impedance of Pt NWs are investigated by either direct current (DC) measurements [6, 20, 22] or high frequency measurements [10, 80]. Interestingly, the majority of papers report certain ranges for the two parameters. This is because the uncertainty introduced by the contacts between the NW and electrodes of the host device presents additional challenges for accurate characterization of NWs, as addressed in [9] for MWCNTs. Even though full-wave modeling and lumped circuit modeling are used to characterize the NWs in a two-port setup, exact values of conductivity and contact impedance can not be determined simultaneously from a single measurement [10, 80]. Recently, capacitive coupling between single walled CNT arrays and a CPW host structure was used to separate contact effects from the CNT's properties [81]. However, since a large number of CNTs is included in the investigated array, intrinsic properties of any individual CNT could not be determined.

In this chapter, the issue of ohmic contacts between individual Pt NWs and electrodes of a CPW host device is removed by utilizing capacitive coupling. This approach simplifies the problem of NW's characterization into determining only their

conductivity. The contact between the NW and the signal line of the CPW is formed with slots or a dielectric layer. Thus, the host device and NW interact exclusively via displacement current. CPW devices with embedded NWs are measured from 0.1 to 40 GHz. To determine the conductivity of Pt NWs, full-wave FEM modeling with ANSYS HFSS [70] is conducted. The simulations are then fitted to measurements to extract the NW's conductivity.

This chapter is organized as follows:

- Section 3.1 introduces FEM-based modeling approach used to study capacitive contacts between NWs and CPW signal lines, and it verifies that two contactless approaches are applicable to determining the conductivity of Pt NWs computationally. Parametric studies of the configuration which has NWs on a dielectric layer are carried out to find critical parameters and their appropriate values. Finally, several computational experiments are demonstrated for the two contactless approaches aimed to show validity of the methods.
- Section 3.2 discusses fabrication, measurement, structural analysis, and modeling for three contactless prototypes. One CPW device for the slot approach and two devices for the dielectric layer approach are examined to find their limitations and issues in fabrication and measurement. Structural investigation of fabricated devices is conducted, so that actual dimensions can be used in modeling. Then, the conductivity of Pt NW is determined from the modeling and measurements of a device on the dielectric layer.

- Section 3.3 further discusses the Pt NW conductivity obtained from Section 3.2, and compares the results with those from Chapter 2. Avenues for further work aimed to improve the accuracy of the contactless approach are also proposed.

3.1. Modeling

The two CPW configurations with coupling contacts are modeled using the full-wave FEM code, ANSYS HFSS. Full-wave modeling is advantageous because it provides solutions based on Maxwell's equations and boundary conditions for three dimensional geometries, once all material properties and dimensions are given. Thus, all coupling effects are directly taken into account in the solution process.

Two configurations with a capacitive contact between an individual Pt NW and the CPW signal lines are developed, as shown in Fig. 3.1. The first approach utilizes a configuration in which a slot slightly wider than the Pt NW is cut into each CPW signal line and the Pt NW is deposited into the slot across the CPW gap (top right in Fig. 3.1). Thus, the Pt NW resides within the slot aperture in the same plane as the signal lines and on top of the substrate. This is referred to as the in-slot configuration. In this case, coupling occurs across the slot. The second approach employs a structure where the Pt NW is supported by a dielectric deposited on top of the CPW signal lines (bottom right in Fig. 3.1). This structure is referred to as the on-dielectric configuration. In this case, coupling occurs through the dielectric layer. The FEM modeling of the two configurations is used to verify the applicability of the two approaches for determining the conductivity of Pt NWs. Modeling validation is carried out with the in-slot

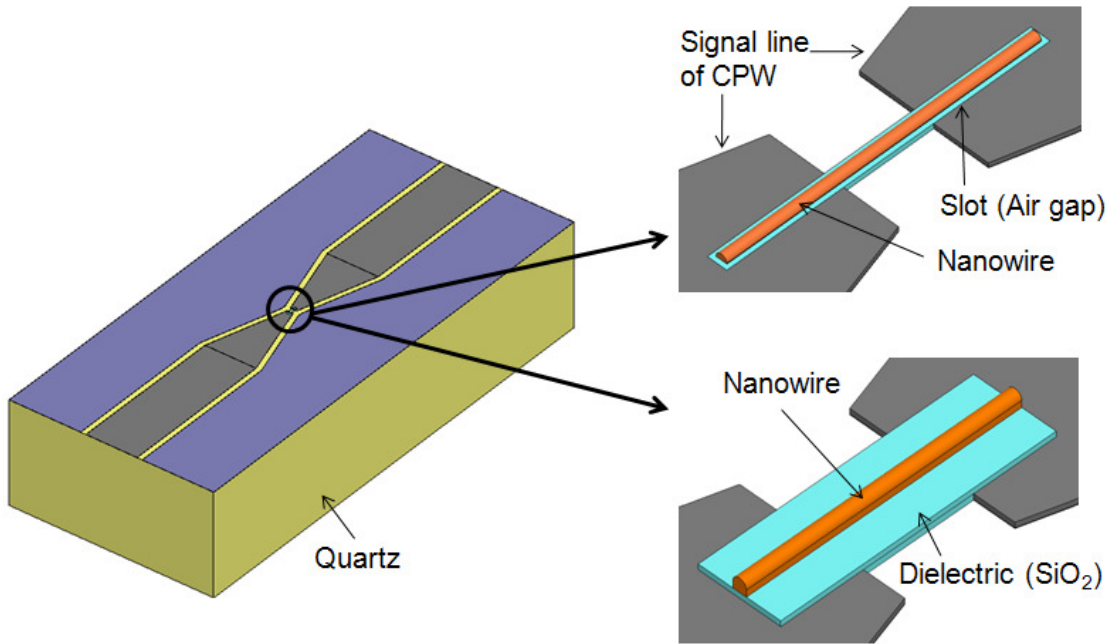


Fig. 3.1 CPW device with individual Pt NWs and details for the two considered approaches. Top right is the in-slot configuration, and bottom right is the on-dielectric configuration.

configuration first. Then, parametric studies are performed with the on-dielectric configuration in order to find the effects and an appropriate range for each parameter. The computational experiments show that both configurations result in similar S-parameter trends for three different conductivities, and that they are applicable in determining the conductivity of Pt NWs.

3.1.1. Validation

CPW devices with the benchmark in-slot configuration are fabricated with a Au line instead of a Pt NW in the slot, and their modeling validation is discussed in this section. The reasons for using the in-slot configurations with the Au line are:

- Both in-slot and on-dielectric configurations are based on capacitive coupling and are expected to produce similar trends in measured S-parameters. Therefore, modeling validation with one configuration is sufficient.
- Realization of an in-slot configuration is much easier than that of an on-dielectric configuration with a metallic line having known material properties. Specifically, the device using an in-slot configuration with a Au line can be realized by simply modifying the Au-short device which is used in Chapter 2.

The suitability of an FEM modeling approach is validated with simple CPW structures having extremely high impedances (empty devices) and low impedances (Au-short devices) shown in Chapter 2. For the in-slot configuration with a Au line, two CPWs are fabricated as shown in Fig. 3.2. The signal lines and the short on either side of the gap are cut to create a 100 μm -long Au line which is isolated from the signal lines. The Au line width and slot width are 1.35 μm and 146 nm for one device (referred to as device A, Fig. 3.2 (c)), and 1.63 μm and 83 nm for the other device (referred to as device B, Fig. 3.2 (d)), respectively. The distance across the gap between the two signal lines is 4 μm . Simulations are conducted with two different values for slot trench depth, 0.1 μm and 1 μm , which is indicated in Fig. 3.2 (d) by dark lines. Although the slot trench depth plays a significant role on the S-parameters, its precise value is very difficult to estimate. From the SEM images it appears the slot trench depth is a few tenths of a μm (see right SEM image in Fig. 3.13; the thickness of the Au signal line is 0.2 μm). Measured and simulated S-parameters of the devices are compared in Fig. 3.3. Simulated S-parameters for slot trench depth of 0.1 μm are well correlated with measurements, and those with a

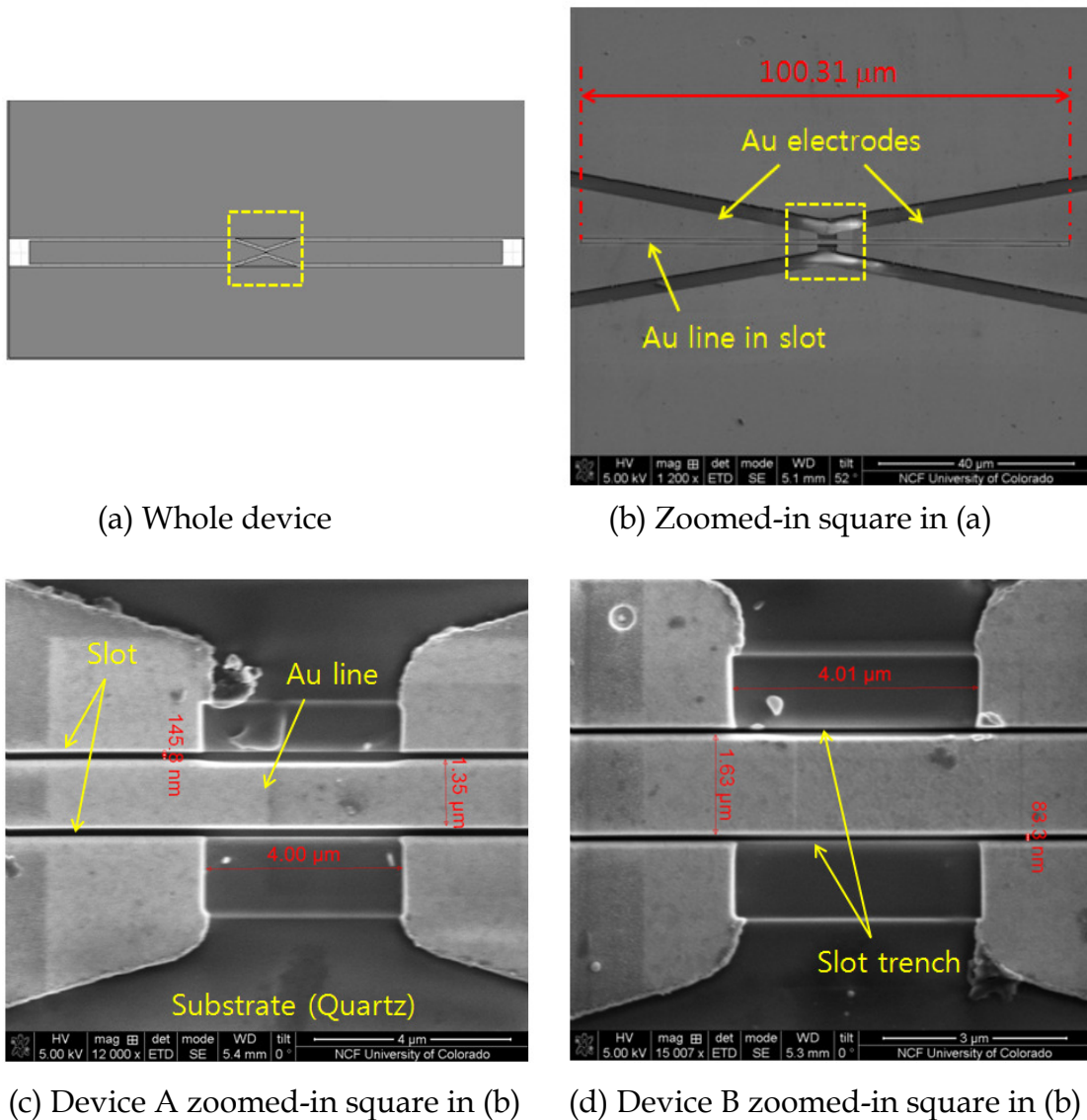


Fig. 3.2 SEM for fabricated devices of the in-slot configuration with a Au line in the slot. (b) is zoomed-in square in (a). (c) and (d) are zoomed-in square in (b).

1 μm depth are matched even better. Differences between simulated and measured $|S_{21}|$ for device A are about 1.6 dB and 0.2 dB for 0.1 μm and 1 μm slot depth, respectively. The differences for device B are about 1.6 dB and 1 dB for 0.1 μm and 1 μm slot trench depths, respectively. If these trenches are omitted in modeling, the difference

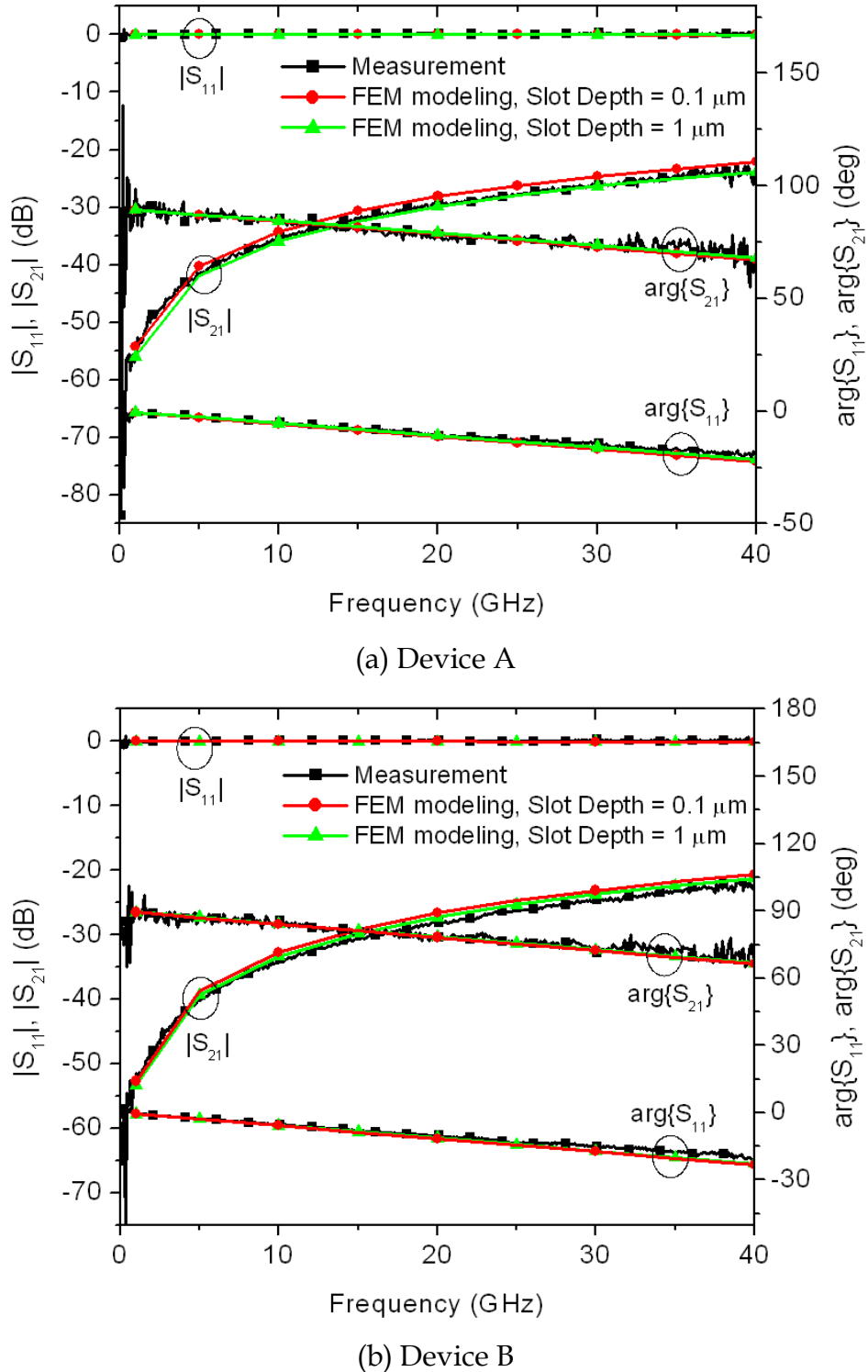


Fig. 3.3 Measured and simulated S-parameters for the devices using an in-slot configuration for modeling validation. The Au line width and the slot width for device A (a) are 1.35 μm and 146 nm, and those for device B (b) are 1.68 μm and 83 nm, respectively.

between simulated and measured results is noticeably increased (about 3 dB for $|S_{21}|$ for device A, and 3.9 dB for device B).

3.1.2. Parametric Study

The conductivity of the Pt NW is the only parameter to be fitted with measurements. The other modeling parameters are:

- a gap distance between the two signal lines, L_{gap} ,
- a contact length (the overlapping length between the NW and signal line), L_{cont} ,
- a dielectric thickness, t_{Die} , or a slot width, W_{slot} , defined from the NW to the signal lines, as shown in Fig. 3.4.

Sensitivity studies for each parameter with the on-dielectric configuration (Fig. 3.4 (b)) are discussed next.

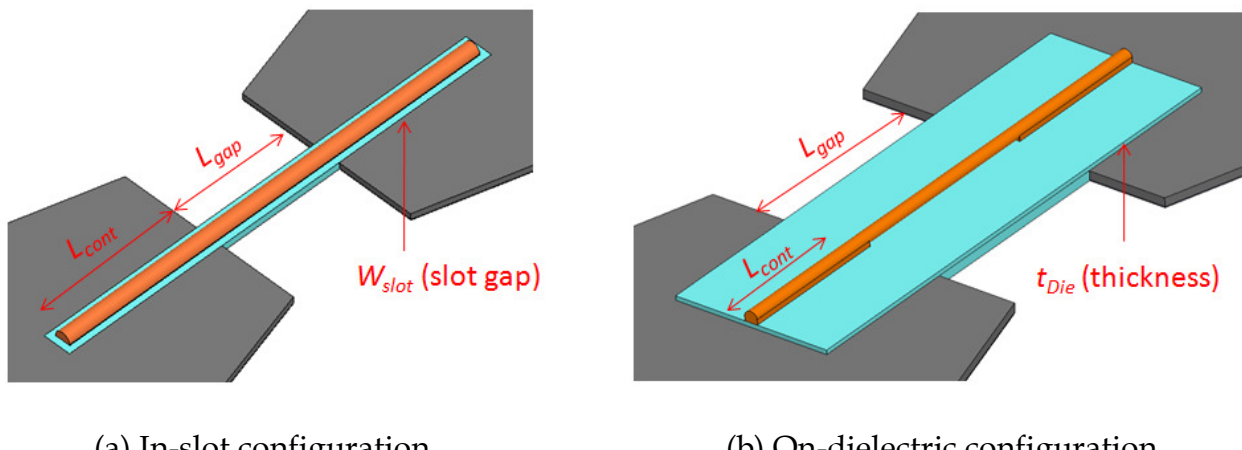


Fig. 3.4 Pt NW of the in-slot and on-dielectric configurations, and their related parameters.

In order to find the most sensitive parameter and each parameter's appropriate value, computational experiments are performed with one parameter varying in a certain range and the other two fixed. Each experiment is carried out with three different Pt NW conductivities, specifically, σ_{bulk} , $0.1\sigma_{bulk}$, and $0.014\sigma_{bulk}$, where σ_{bulk} is the bulk conductivity (9.3×10^6 S/m) and $0.014\sigma_{bulk}$ is the minimum value for a Pt NW as reported in Section 2.3.4. The diameter of the Pt NW is 250 nm, and the frequency is 40 GHz.

The dielectric thickness, t_{Die} , is varied first in the range from 1 to 20 nm. The gap distance and the contact length are set at 4 μm and 20 μm , respectively. Simulated S-parameters for the three conductivities are shown in Fig. 3.5. Note that each conductivity produces unique responses for $|S_{11}|$ and $|S_{21}|$. As seen, when t_{Die} is smaller than 7 nm, the difference for both $|S_{11}|$ and $|S_{21}|$ is significantly larger. However, phase responses of S_{11} and S_{21} are less sensitive as the conductivity decreases ($0.1\sigma_{bulk}$ - $0.014\sigma_{bulk}$).

Next, the gap distance, L_{gap} , is varied from 4 μm to 20 μm . In this case, the dielectric thickness and the contact length are fixed at 10 nm and 20 μm , respectively. Fig. 3.6 shows simulated S-parameters for the three conductivities. Results show that magnitudes of S_{11} and S_{21} are sensitive to the conductivity, but phases are not for low conductivities. It is also observed that both $|S_{11}|$ and $|S_{21}|$ do not change very much when L_{gap} is varying over the range, meaning that L_{gap} does not play as significant a role as t_{Die} .

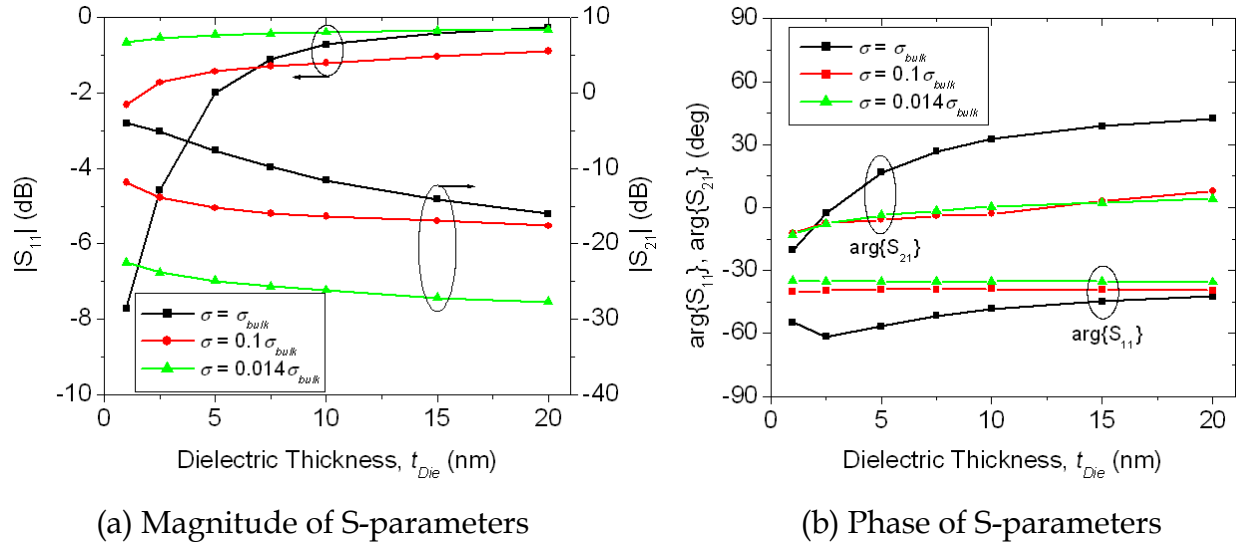


Fig. 3.5 Simulated S-parameters for parametric studies with dielectric thickness t_{Die} varied from 1 nm to 20 nm. L_{gap} is 4 μm and L_{cont} is 20 μm . The frequency is 40 GHz.

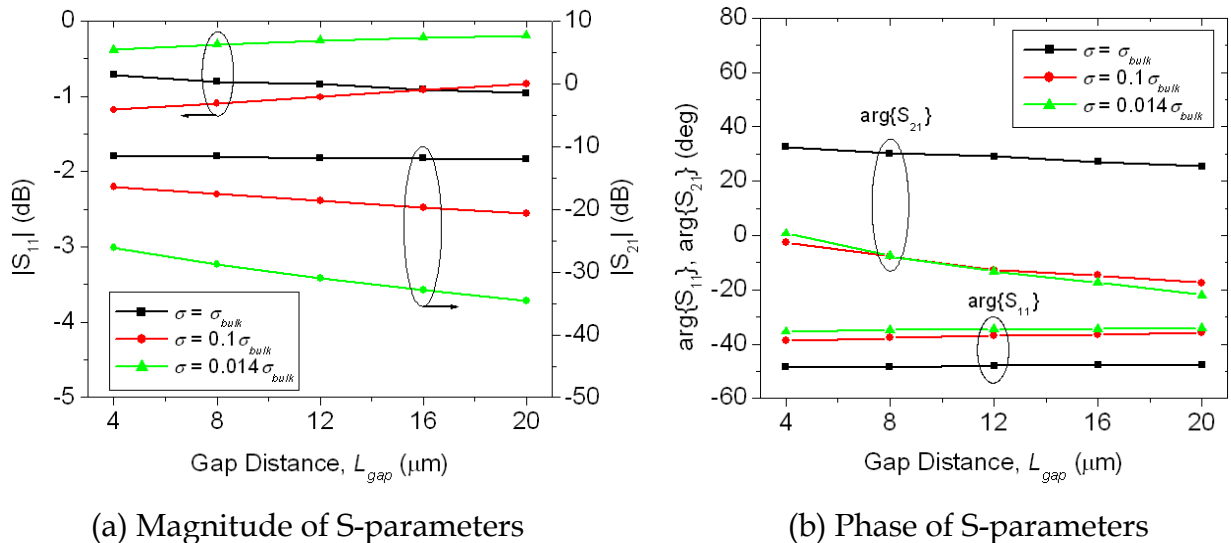


Fig. 3.6 Simulated S-parameters for parametric studies with gap distance, L_{gap} . t_{Die} is 10 nm and L_{cont} is 20 μm . The frequency is 40 GHz.

Finally, the contact length is varied from 10 μm to 50 μm with fixed dielectric thickness of 10 nm and gap distance of 4 μm . S-parameters are shown in Fig. 3.7. As before, it is seen that the magnitude responses are more sensitive than the phase

responses. $|S_{11}|$ and $|S_{21}|$ become even more sensitive when L_{cont} is larger than 20 μm . Also note that $|S_{11}|$ and $|S_{21}|$ responses (except $|S_{11}|$ for high conductivity ($\sigma = \sigma_{bulk}$)) saturate at $L_{cont} = 40 \mu\text{m}$. Therefore, it seems that L_{cont} does not need to be longer than 50 μm for this study.

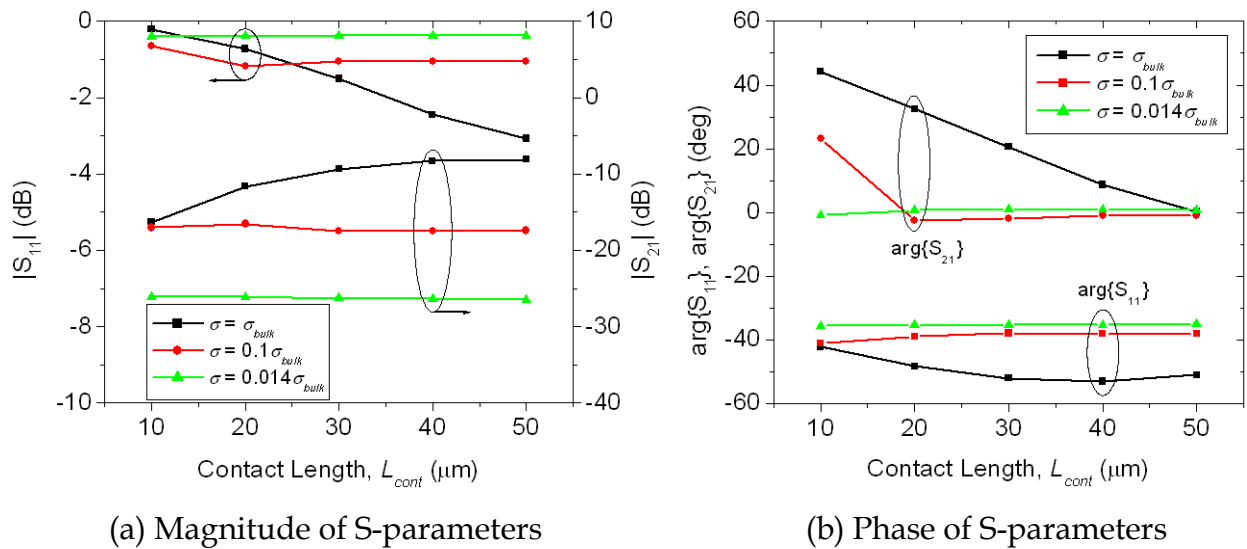


Fig. 3.7 Simulated S-parameters for parametric studies with contact length L_{cont} . t_{Die} is 10 nm and L_{gap} is 4 μm . The frequency is 40 GHz.

Overall, it is found that the most sensitive parameter is the dielectric thickness, followed by the contact length. This is not surprising as both quantities are closely related to the capacitive coupling strength. Appropriate values for each parameter are also found: the dielectric thickness is recommended to be smaller than 7 nm, and the contact lengths in 40–50 μm range are acceptable. The gap distance is not as important within the range from 4 to 20 μm .

An important necessity of this methodology is to have the NW to strongly couple with signal lines. However, to cut narrow slots and to deposit a thin dielectric layer on a nm-scale is quite challenging. At the very best the width of a focused ion beam (FIB) cut slot in SiO_2 is 15 nm at the Nanomaterials Characterization Facility (NCF) at the University of Colorado. Instead of reducing the slot width and the dielectric thickness, the coupling area can be increased by increasing the contact length. Numerical studies are conducted for the two contactless configurations. The contact length of 50 μm and the slot width / the dielectric thickness of 50 nm are used in the further computational studies. Fig. 3.8 and Fig. 3.9 show simulated S-parameters for the devices with in-slot and on-dielectric configurations, respectively. A 250 nm diameter Pt NW is employed with conductivities of σ_{bulk} , $0.1\sigma_{\text{bulk}}$, and $0.014\sigma_{\text{bulk}}$. As seen for both configurations, the S-parameter responses are quite sensitive to the chosen conductivities of the NWs,

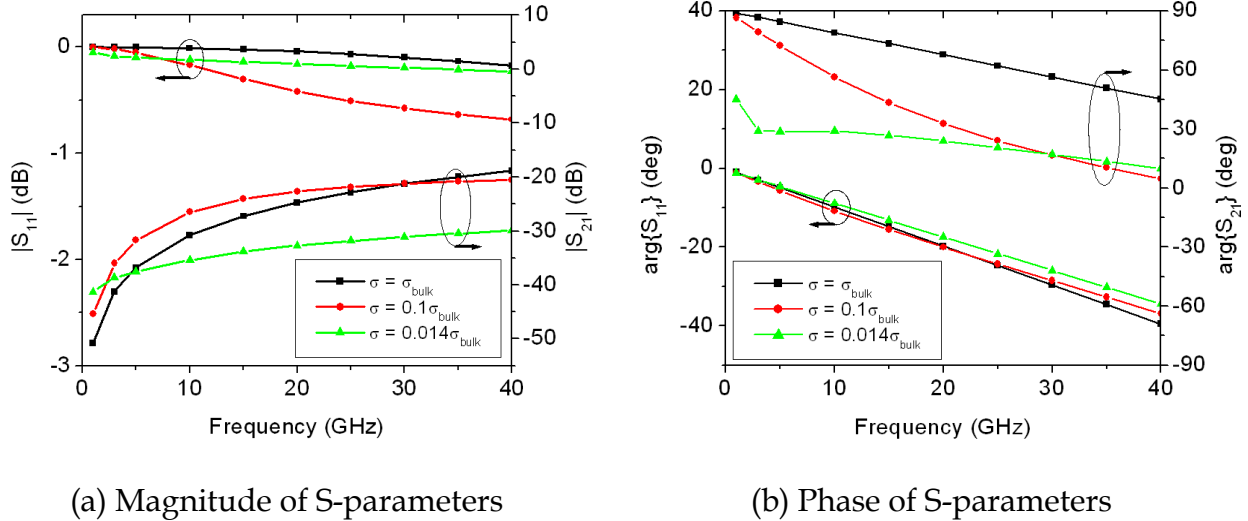


Fig. 3.8 Simulated S-parameters for in-slot configurations with three different conductivities of σ_{bulk} , $0.1\sigma_{\text{bulk}}$, and $0.014\sigma_{\text{bulk}}$.

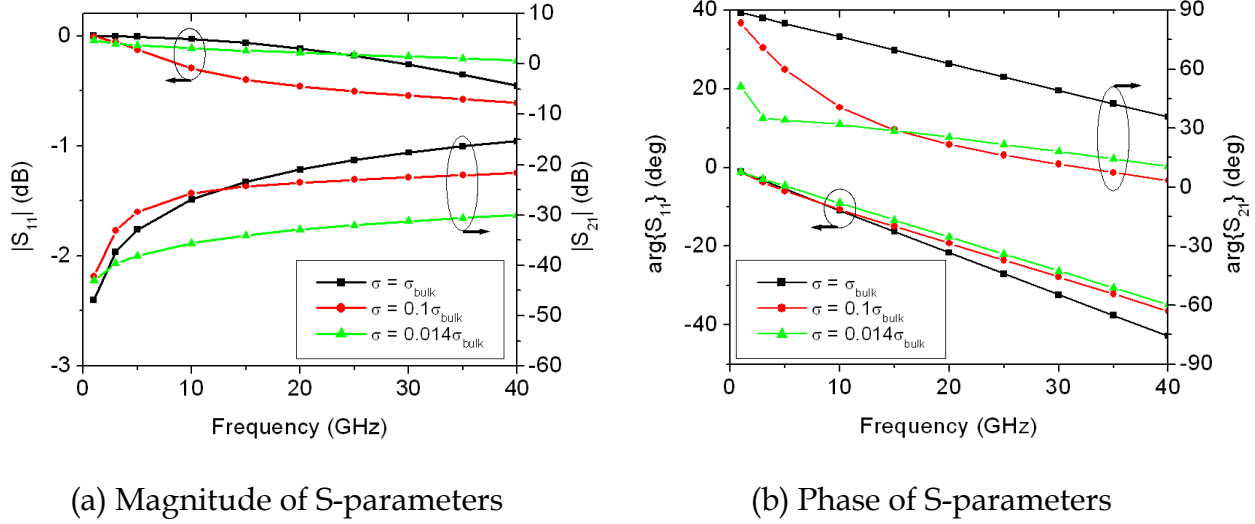


Fig. 3.9 Simulated S-parameters for on-dielectric configurations with three different conductivities of σ_{bulk} , $0.1\sigma_{bulk}$, and $0.014\sigma_{bulk}$.

particularly the responses for S_{21} . There is a slight difference between the two structures, but general trends are very similar.

3.2. Prototypes

As seen earlier, building a narrow slot or a thin dielectric is required for strong coupling and good sensitivity. However, the fabrication of both is quite challenging. Three prototypes (one for in-slot and two for on-dielectric configurations) are fabricated to find limitations and issues in the fabrication process and measurements using the available facilities. After the measurements are completed, fabricated devices for the on-dielectric configuration are evaluated using destructive analysis to better understand their structure and dimensions. Their elemental analysis is performed to find the composition of contaminations in the dielectric. Two-port S-parameters and DC

resistances for the devices are measured to verify if the coupling contacts are fabricated correctly and working properly with the Pt NWs.

3.2.1. Fabrication and Measurements

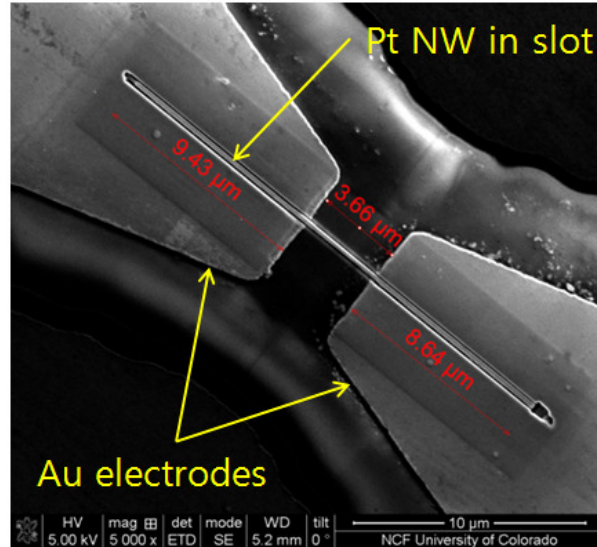
For the in-slot configuration, a slot slightly wider than the Pt NW is cut into each CPW signal line. The Pt NW is subsequently deposited into this slot region and across the gap. A final trimming is performed around the NW to isolate it from the CPW signal line. For the on-dielectric configuration, the NW is supported above the signal lines by a thin SiO₂ dielectric layer which is 30 to a few hundreds nm thick. Note that with the NCF's SEM the minimum measurable thickness is about 15 nm. The dielectric covers both the signal line and the gap allowing for a smooth continuous surface for the NW. The CPW is fabricated on a quartz substrate using conventional micro-lithography. Fabrication of the CPW structures and calibration lines are described in Section 2.1.1.

A dual beam FIB is used to fabricate the NW structures. The FIB employs a Ga ion beam to deposit Pt and sculpt the surface of the CPW. A field emission SEM is focused at the same position as the Ga ion beam allowing viewing of the CPW as modifications are in progress. A technique referred to as ion beam induced deposition (IBID) is employed for the Pt and SiO₂ deposition. Trimethyl [(1,2,3,4,5-ETA.)-1 Methyl 2, 4-Cyclopentadien-1-YL] Platinum is heated in a crucible and injected onto the CPW. The energy of the ion beam dissociates the Pt from the organic components and the Pt quickly adheres to the sample surface under the beam. The resulting NW is approximately 6% Ga, 34% C, and 60% Pt. In addition, using the same deposition

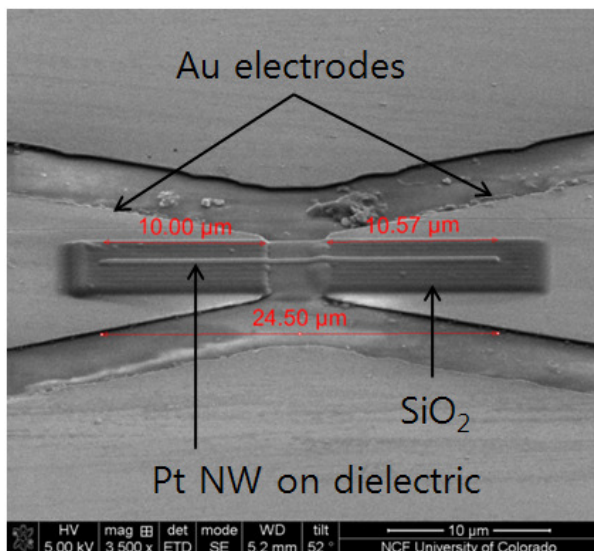
mechanism as the Pt deposition, the SiO_2 insulating support structure for the Pt wire is IBID deposited onto the CPW electrodes. In this case, the precursor compound Tetraethyl Orthosilicate [$\text{Si}(\text{OC}_2\text{H}_5)_4$] is used to deposit SiO_2 . The SiO_2 has a high concentration of Ga from the deposition process. Ion beam sputtering is used to cut the slot into the Au CPW signal lines. All of the FIB processing is performed at 30 kV with beam currents ranging from 1.5 pA to 98 nA. Vacuum in the specimen chamber is 5×10^{-6} Torr. Dimensions were later examined using FIB cross-sections viewed in the SEM.

Fig. 3.10 shows the fabricated prototypes with their dimensions estimated from SEM photographs. One for the in-slot configuration (Fig. 3.10 (a)) and two for the on-dielectric configuration are shown. The two on-dielectric devices are distinguished by the thickness of the SiO_2 dielectric layer: thick SiO_2 shown in Fig. 3.10 (b), and thin SiO_2 in Fig. 3.10 (c). They have about a 10 μm -long overlap between the Pt NW and CPW signal lines on each side, and about 4 μm -long gap distance between the signal lines. Other dimensions are represented later when each device is discussed in greater detail.

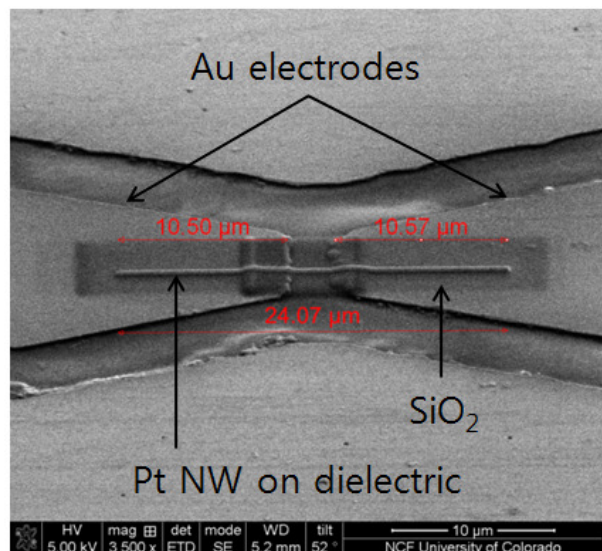
Two-port S-parameter measurements for the devices with Pt NWs are carried out from 0.1 to 40 GHz with ground-signal-ground (GSG) probes. For broadband measurements, on-wafer multiline Thru-Reflect-Line (TRL) calibration is performed. The calibration standards, including four different length lines, are patterned on the same chip. A multimeter connected to the two probes is used to measure DC resistance during high frequency measurements simultaneously. Measured DC resistance easily indicates if the NW is shorted to the CPW signal lines.



(a) In-slot configuration



(b) On-dielectric (thick)



(c) On-dielectric (thin)

Fig. 3.10 SEM of fabricated prototypes with Pt NWs. (a) In-slot configuration, (b) on-dielectric configuration with thick SiO_2 , and (c) on-dielectric configuration with thin SiO_2 .

3.2.2. In-slot Configuration Prototype

The fabricated device for an in-slot configuration with an individual Pt NW in the slot is shown in Fig. 3.11. Dimensions of the device are estimated from the SEM

images. The contact lengths are $9.43\ \mu\text{m}$ and $8.64\ \mu\text{m}$, and the gap distance is $3.66\ \mu\text{m}$, slightly shorter than intended dimensions, as shown in Fig. 3.11 (a). The width of the NW is measured to be about $177\ \text{nm}$. The slot widths are $22.5\ \text{nm}$ and $32.8\ \text{nm}$ on both sides of the NW (asymmetric slot, Fig. 3.11 (b)).

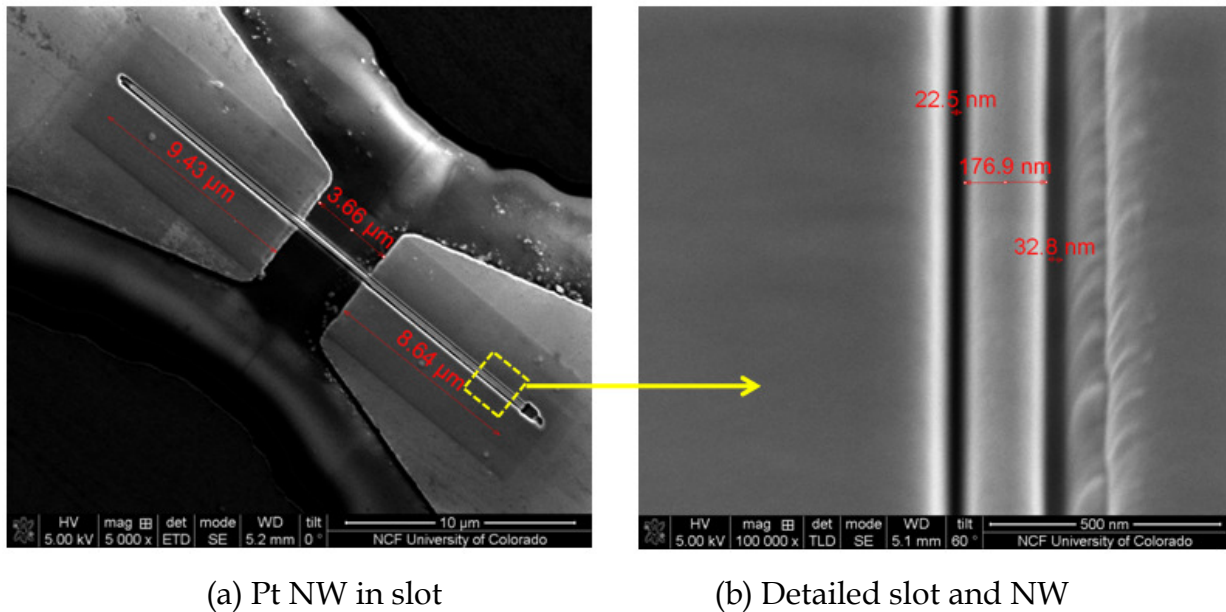


Fig. 3.11 SEM of fabricated prototypes of the in-slot configuration. (a) Pt NW in slot, (b) detailed slot and Pt NW, and their dimensions. The NW width is estimated at about $177\ \text{nm}$. The slot is asymmetric with respect to the NW.

Two-port measurements of DC resistance and S-parameters from $0.1\ \text{GHz}$ to $40\ \text{GHz}$ are conducted on the prototype device. The DC resistance is measured at about $1.72\ \text{k}\Omega$, although it is expected to be $1\text{--}2\ \text{M}\Omega$ (the multimeter used in measurements records about $2\ \text{M}\Omega$ for empty devices or open circuits) due to the presence of the slot. Measured magnitudes of S-parameters are shown in Fig. 3.12. It is observed that $|S_{21}|$ at lower frequencies is about $-25\ \text{dB}$ which is much higher than expected. If the coupling

contacts with the slot work as designed, $|S_{21}|$ at around 0.1 GHz should be lower than -50 dB, as shown in Fig. 3.3.

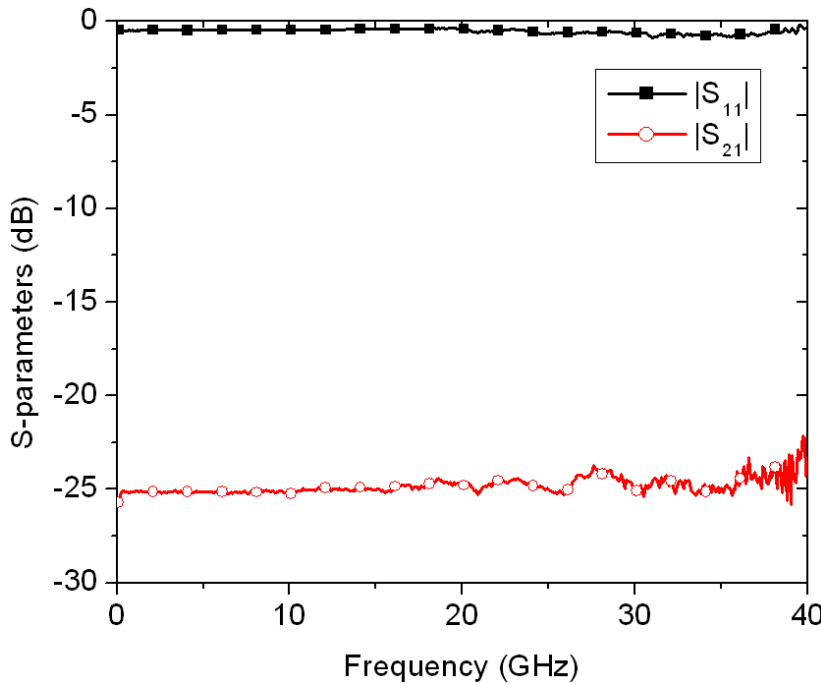


Fig. 3.12 Measured magnitude of S-parameters for the prototype with an in-slot configuration.

To better understand the problem, structural investigation (destructive analysis) is conducted for the device from one contact end to the other. Fig. 3.13 shows the two ends of the Pt NW. The results indicate that residual, thinned metal bridges remained after post processing and are directly connecting the NW and signal lines. The measured DC resistance of $1.72 \text{ k}\Omega$ is much lower than $2 \text{ M}\Omega$ for the open circuit, however, it is very high for a short circuit. It is thought that the high contact resistance is caused by very small contact points. The structural analysis clearly shows the difficulty in fabricating an ideal narrow slot in a device with individual Pt NW.

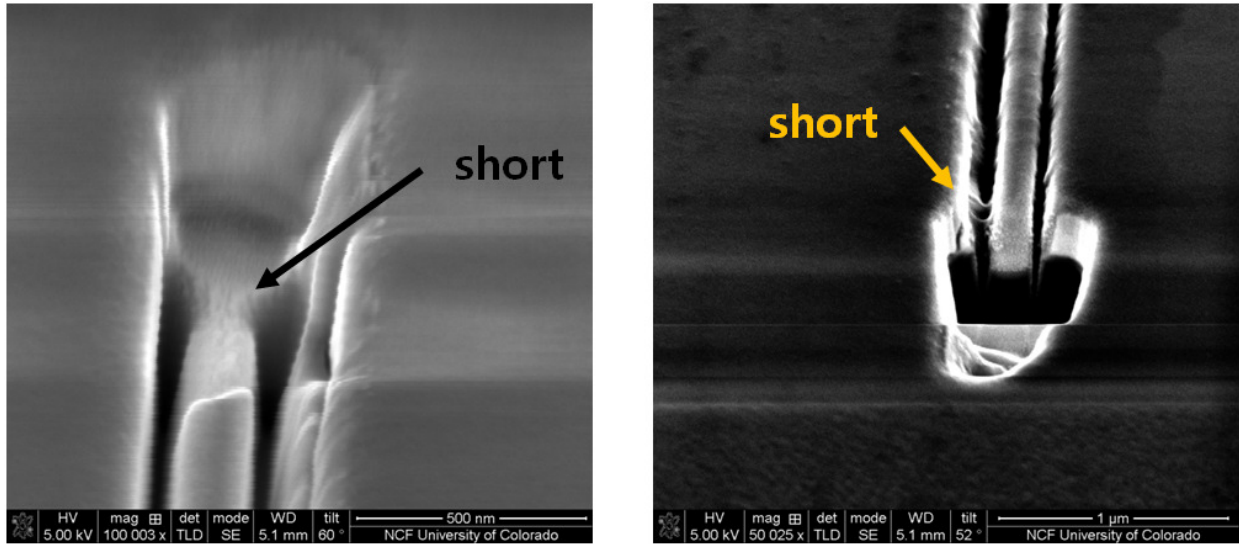


Fig. 3.13 SEM of the two ends of the Pt NW in the prototype with an in-slot configuration. It seems that there are short connections between the Pt NW and the signal lines at both ends. Because the contact points are very small, DC resistance is measured at about $1.72\text{ k}\Omega$.

3.2.3. On-dielectric Configuration Prototypes

DC resistances for the two prototypes with the on-dielectric configuration are measured to be about $2\text{ M}\Omega$ for the device with thick SiO_2 and $1\text{ M}\Omega$ for thin SiO_2 . From these results, both capacitive contacts seem to be fabricated properly. However, the device with the thin dielectric produces unexpected S-parameters as shown in Fig. 3.14. $|S_{21}|$ for the device with thin dielectric is very similar when compared to that of empty devices, which is shown in Fig. 2.4 (a), even though it is expected to be higher than that of a device with thick dielectric. Also, $\arg\{S_{22}\}$ for the device with thin dielectric is different than $\arg\{S_{11}\}$. Phase responses of S-parameters show that port 2 of this prototype is short circuited because $\arg\{S_{11}\}$ and $\arg\{S_{22}\}$ are 180° out of phase. It is not clear yet what causes this failure.

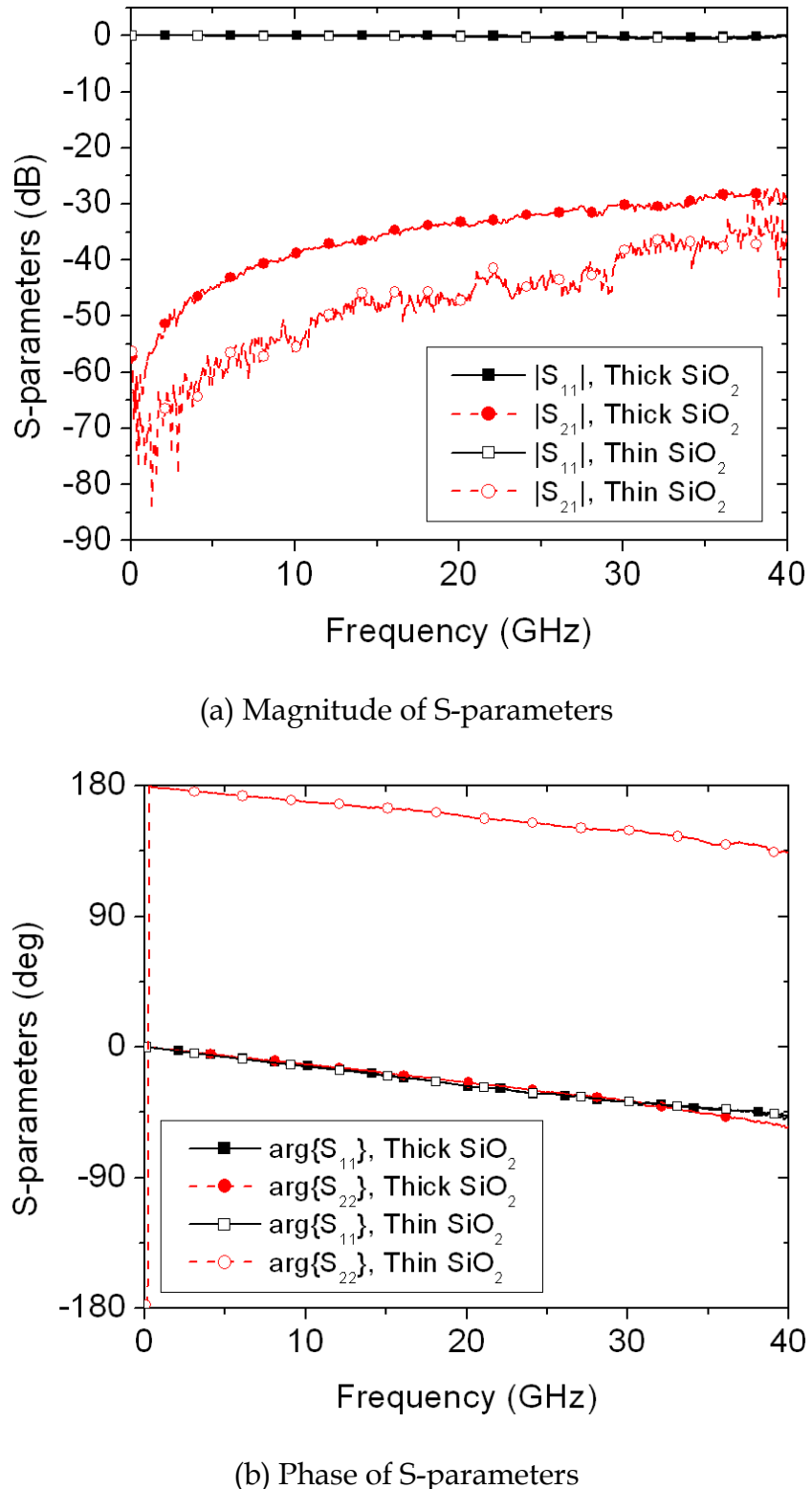


Fig. 3.14 Measured S-parameters for two prototypes of the on-dielectric configuration.

In order to accurately model a device under test, solid information about its dimensions is necessary. However, the dimensions for devices pertained to the on-dielectric configuration cannot be determined from the SEM images of Fig. 3.10 because the thickness of the SiO₂ under the Pt NW is difficult to measure using non-destructive approaches. Therefore, after the S-parameters are measured, one side of the Pt NW is cross-sectioned using FIB to measure the thickness of the SiO₂ as shown in Fig. 3.15. For the device with thick SiO₂, the dielectric thickness under the NW is measured at 222 nm. In addition, the cross section of the Pt NW is found to be a rounded rectangle with a 216 nm height and 340 nm width, as seen in Fig. 3.15 (a). FEM modeling for this prototype has been conducted with these dimensions. Although it is known that the device with thin SiO₂ does not work properly, destructive analysis for this prototype is also performed. Fig. 3.15 (b) shows that the thin SiO₂ has a 60 nm dielectric thickness, and that the Pt NW has a 420 nm width and 298 nm height.

To estimate the conductivity of the Pt NW, FEM modeling for the prototype of thick SiO₂ is conducted with the above dimensions for the NW and SiO₂ dielectric, and modeling results are compared to measured data. Initial conductivity for the NW is set at σ_{bulk} . In Fig. 3.16, simulated S-parameters for four modeling variations of the conductivity and dielectric constant of SiO₂ are compared to measurements. The best modeling fit is when $\sigma = 0.014\sigma_{bulk}$ and $\epsilon_{r,eff} = 12$, where $\epsilon_{r,eff}$ is an effective dielectric constant. To better understand this result, three points need to be discussed. First, the obtained conductivity from this configuration is well correlated with the value determined in Chapter 2 (see Section 2.4.3). This finding is consistent with the finding in

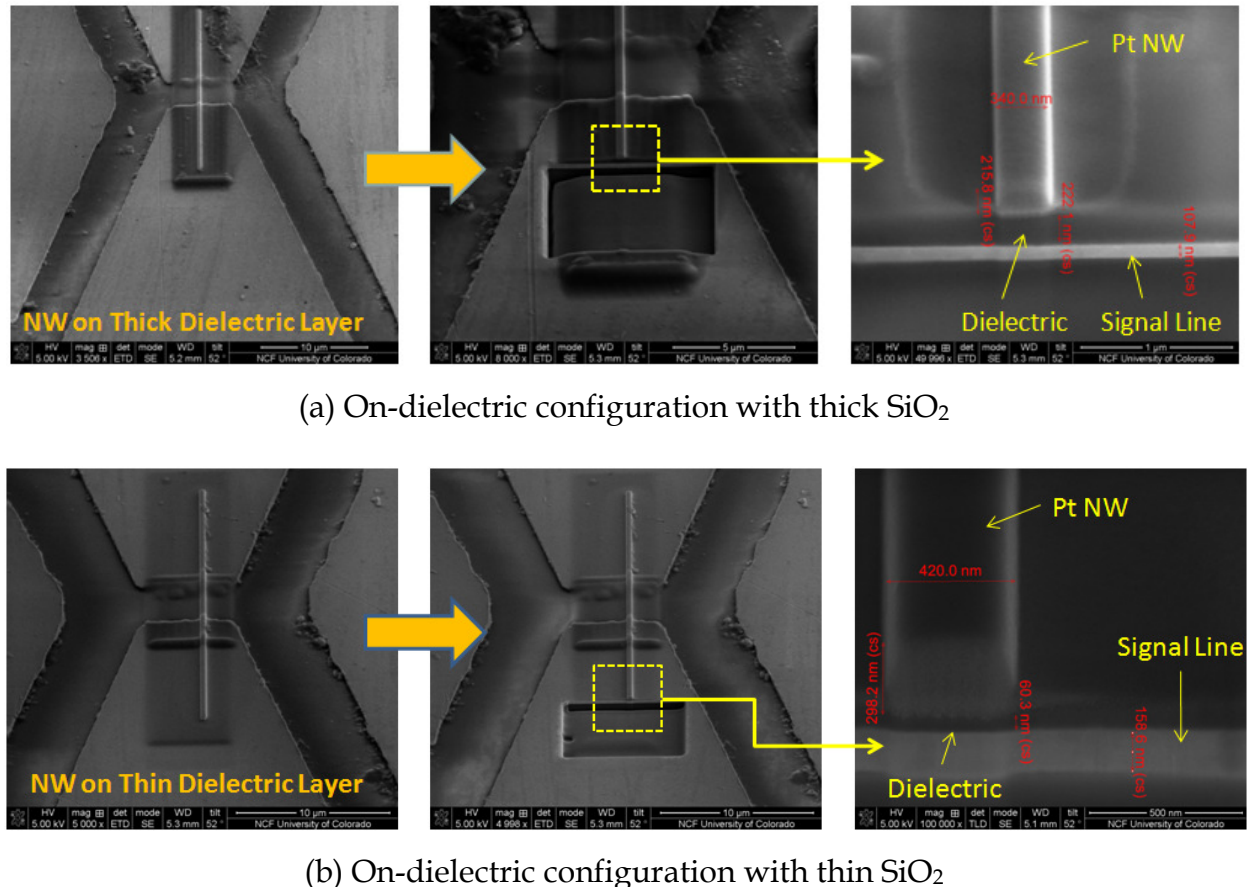


Fig. 3.15 SEM of destructive analysis for prototypes of the on-dielectric configuration. One end of the Pt NW and SiO_2 layer is cross-sectional cut to estimate dimensions. Dimensions of the Pt NW and the thickness of the SiO_2 dielectric are measured from these cross-sectional images.

the previous chapter that the contact resistance is indeed relatively small. The NW on the device in Chapter 2 is overlapping with the signal lines over the long length ($3 \mu\text{m}$ on either side). Although it is assumed that a contact point is tiny at any cross-section of the NW, the overall contact is established on a $3 \mu\text{m}$ length on each side.

Second, the resultant effective dielectric constant of the dielectric layer supporting the NW is much larger than the dielectric constant of pure SiO_2 , which is about 4. This may be due to the presence of contaminations in the dielectric layer.

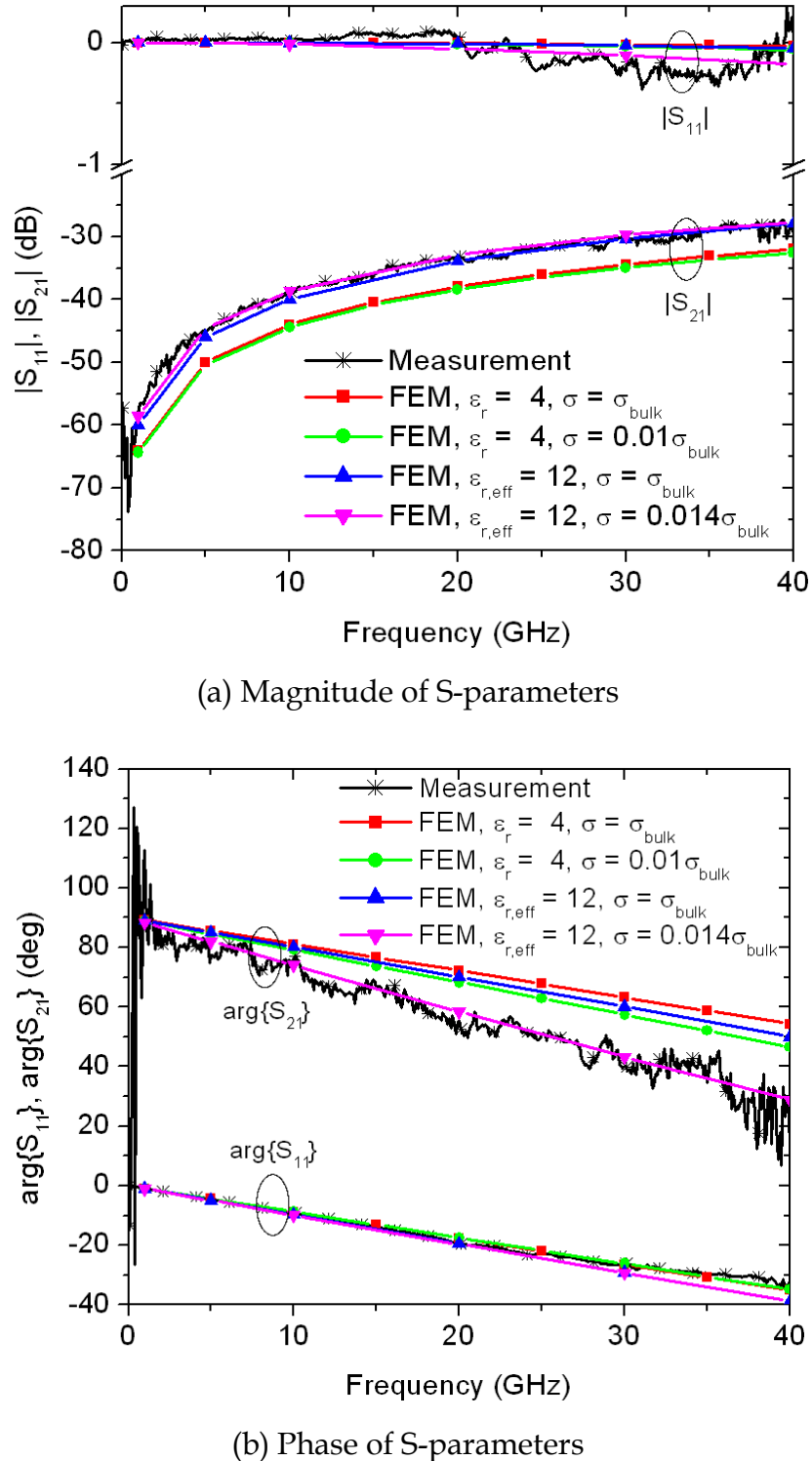


Fig. 3.16 Measured and simulated S-parameters for the prototype of the on-dielectric configuration of thick SiO₂. FEM modeling fits are conducted with effective dielectric constant $\epsilon_{r,\text{eff}}$ and conductivity σ . The best fit is of $\epsilon_{r,\text{eff}} = 12$ and of $\sigma = 0.014\sigma_{\text{bulk}}$.

Similar to the NW mentioned in Section 3.3.1, it is expected that Ga and C are mixed in the dielectric layer during deposition of the SiO_2 , thus affecting the material properties of the dielectric. This can result in a larger effective dielectric constant of the dielectric layer than its tabulated value. Elemental analysis of the SiO_2 dielectric deposited on Ni substrate was conducted for several conditions and results are given in Appendix C. The results show that Ga and Si atoms are indeed present and their values are about 35 % and 10 %, respectively. Therefore, the deposited dielectric layer is more likely Ga_2O_3 than SiO_2 . The dielectric constant of Ga_2O_3 is 10-14 [82], which is similar to the obtained effective dielectric constant.

Third, the measured thickness of the deposited dielectric is large, thus the S-parameters are not very sensitive to different conductivities. Only one end of the NW has been cut to measure the dielectric thickness, however, its thickness can vary along the length of the NW depending on the fabrication process. Dimensions are determined by comparing contrast for each layer from the SEM image, and are difficult to measure exactly. Further structural investigations are necessary. In addition, simulated S-parameters for the two different conductivities (σ_{bulk} and $0.01\sigma_{bulk}$) when the dielectric constant equals to 4 are close to each other, although noticeable differences are expected. The above discussion clearly indicates that the dielectric layer is too thick for the *small* NW to strongly couple with the CPW signal lines. Additionally, computational studies with several different thicknesses of the dielectric layer from 10 nm to 200 nm show that differences for the two conductivities are less than 1 dB for $|S_{21}|$ and 10° for $\arg\{S_{21}\}$ at 40 GHz when the thickness is larger than 150 nm. Differences in S_{11} are smaller than

those in S_{21} . Therefore, it is not recommended to use a thick dielectric layer compared to the diameter of the NW under test to characterize the NW's material parameters.

3.3. Discussion

Experiments and related observations discussed in Section 3.2 show that the contactless metrology approaches are highly dependent on the ability to fabricate test devices with known structural and electrical forms. Studies of the on-dielectric configuration with a thick dielectric, however, have resulted in a reasonable value for the conductivity of a Pt NW. That is, the obtained conductivities from the on-dielectric configuration and from the direct contact configuration in Chapter 2 are well correlated ($\sigma = 0.013\sigma_{bulk}$ to $0.014\sigma_{bulk}$). The results are also close to the minimum value of conductivity obtained from fitting methods in Section 2.3.4. Therefore, the on-dielectric configuration based contactless approach is feasible for the characterization of metallic NWs.

Additional research is needed to improve the accuracy of the method and obtained results. First, the deposited dielectric layer in on-dielectric configuration needs to be fully characterized. As discussed earlier, the dielectric layer is heavily contaminated, thus the material property, i.e. dielectric constant, is significantly altered. Measurement of the dielectric constant of the dielectric layer is necessary to improve the results. Secondly, as discussed in Section 3.2.3, using a thinner dielectric layer for stronger coupling is recommended. That way, $|S_{21}|$ responses will be more sensitive to small variation of the conductivity. Parametric studies in Section 3.1.2 show that the

dielectric thicknesses under 10 nm enable observation of large difference between different conductivities. Note that a few nanometers thick dielectrics can be achieved by oxidation of a thin metal layer such as aluminum oxide [83].

CHAPTER 4

CHARACTERIZATION OF INDIVIDUAL CARBON NANOTUBES AND APPLICATIONS

Over the past 15 years, carbon nanotubes (CNTs) [26] have attracted a great deal of interest among scientists and engineers. Excellent electrical, thermal, and mechanical properties have inspired discussions about the use of CNTs in various microwave applications [34], future low-loss high speed VLSI circuits [84], and THz interconnects [85]. It has been suggested that the connection between nanoscale systems and the macroscopic world can be effectively engineered with CNT dipole antennas [53]. Electromagnetic analysis and prediction of CNT parameters important for their RF use, such as S-parameters, losses, impedance, and far-field characteristics for antennas, are, however, challenging. Excellent treatment of this problem and an effective semi-classical approach for determining the input impedance of a CNT dipole antenna are provided by Hanson [8].

In this chapter, metallic single wall CNTs (SWCNT) are characterized by the use of frequency-dependant complex conductivity. Several interconnect applications using individual SWCNTs are solved numerically within the classical Maxwellian formulation. Interconnects to be investigated herein are wireless configurations with

CNT dipole antennas, nano-coaxial lines, and single wire transmission lines. The analysis is conducted with commercial software tools based on MoM and FEM. Computed S-parameters from either method are used for evaluating the performance of CNTs as interconnects. To assess the potential benefits of CNTs the comparison with their Cu-based counterparts is also provided.

This chapter is organized as follows:

- Section 4.1 discusses modeling approaches and multi-step modeling validation for individual SWCNTs. Wire and surface models of CNTs are developed for use with MoM and FEM, respectively. A dipole antenna and a coaxial line are used for the validation. Then, several parameters are introduced to evaluate the performance of CNTs for interconnect applications.
- Section 4.2 provides discussion of several CNT interconnect embodiments including half-wavelength dipole pair, atomic layer deposition (ALD) enabled nano-coaxial line [86, 87], Sommerfeld and Goubau transmission lines [88]. Transmission coefficient and line loss of the interconnects are computed from simulated S_{21} , and CNTs are compared with their Cu-based counterparts.
- Section 4.3 compares signal transmission for all the interconnect embodiments studied in this chapter with respect to shorter and longer distances. Specifically, a coaxial line and single wire transmission lines are studied with several different coating thicknesses.

4.1. Modeling Individual CNTs

4.1.1. Modeling Approaches and Validation

Metallic SWCNTs are modeled using a frequency-dependant complex conductivity for wire and surface based models in the MoM code EMSS FEKO [89]. In the FEM tool ANSYS HFSS [70], the SWCNTs are also modeled by utilizing an impedance boundary condition. In this thesis, the wire and surface models refer to the way in which the CNTs are meshed within the full-wave models. In MoM, wire segment and triangular tessellation schemes correspond to different basis functions used in the solution process. Notice that triangular tessellation scheme (surface models) has an error associated with approximation of curved surfaces with flat triangles. The 3-D FEM employs volumetric meshing, thus the surface of the CNTs is discretized with triangular facets. It is well established that the CNT's complex conductivity can be computed as [8]

$$\sigma_{CNT}(\omega) = -j \frac{2e^2 v_F}{\pi^2 \hbar a (\omega - j\nu)} \text{ (S)}, \quad (4.1)$$

where e is the electron charge, \hbar is Planck's constant divided by 2π , ω is the angular frequency, a is the radius of the CNT, ν ($= \tau^{-1}$, τ : the relaxation time) is the relaxation frequency discussed in detail in [90], and v_F is the Fermi velocity (9.71×10^5 m/s). Notice that the unit for conductivity is S, not S/m since the walls of the CNT are

assumed to be infinitely thin, supporting the flow of surface currents. Using (4.1), the surface resistance per unit length for the CNT wire model can now be obtained as

$$Z_{CNT} = \frac{1}{2\pi a \sigma_{CNT}} \text{ } (\Omega/\text{m}), \quad (4.2)$$

and the surface resistivity for the CNT surface model is

$$\rho_{CNT} = \frac{1}{\sigma_{CNT}} \text{ } (\text{S}). \quad (4.3)$$

To compare CNTs with Cu nanotubes, the latter needs to be characterized in the same way as CNTs. The conductivity of the Cu nanotubes, derived from the Fermi-gas model of electrons in metals, is represented as [8]

$$\sigma_{Cu}(\omega) = -j \frac{e^2 N_e^{2d}}{m_e(\omega - jV)} \text{ } (\text{S}), \quad (4.4)$$

where m_e is the mass of an electron, and N_e^{2d} is the number of electrons per square meter. N_e^{2d} can be found from $N_e^{2d} = (N_e^{3d})^{2/3}$, where N_e^{3d} ($\approx 8.46 \times 10^{28}$ electrons/m³ for Cu) is the three-dimensional electron density. To find the surface resistance per unit length Z_{Cu} and the surface resistivity ρ_{Cu} of Cu nanotubes, σ_{CNT} needs to be replaced by σ_{Cu} in (4.2)

and (4.3). As mentioned, both the wire and surface models can be developed for MoM formulation, and their validations are conducted with the simple resonant dipole antennas.

To assess the ability of FEM for modeling CNT interconnects, the frequency dependent surface resistivity (4.3) is utilized for respective surface models. The surface resistivity is applied within the impedance boundary conditions for the CNTs and Cu nanotubes. To validate FEM surface models, ALD-enabled nano-coaxial lines are employed instead of dipole antennas. A detailed flow chart of the modeling approaches and the multi-step validation procedures are shown in Fig. 4.1. Firstly, the MoM wire models of the CNT and Cu dipole antennas are validated with corresponding results reported in [8]. Secondly, the MoM surface models of the CNT dipole antennas are validated with their MoM wire models. Finally, the FEM models of a nano-coaxial line having a CNT inner conductor are validated with corresponding MoM surface models.

Shown in Fig. 4.2 (a) is an input impedance comparison for wire-based models of Cu nanotube dipole antennas (step 1 in Fig. 4.1), and in Fig. 4.2. (b), is a comparison for surface-based models of CNT dipole antennas (step 2 in Fig. 4.1). The radius of the dipoles is 2.712nm, and their length is 20 μm . As seen, excellent agreement between the two modeling approaches and literature is obtained for both Cu nanotube and CNT dipoles. Note that, although the dimensions of the two dipoles are the same, their characteristics over a wide frequency range are quite different. Specifically, the Cu nanotube dipole does not resonate at all, while the CNT dipole does at three frequencies. These resonances occur due to the excitation and propagation of surface plasmon

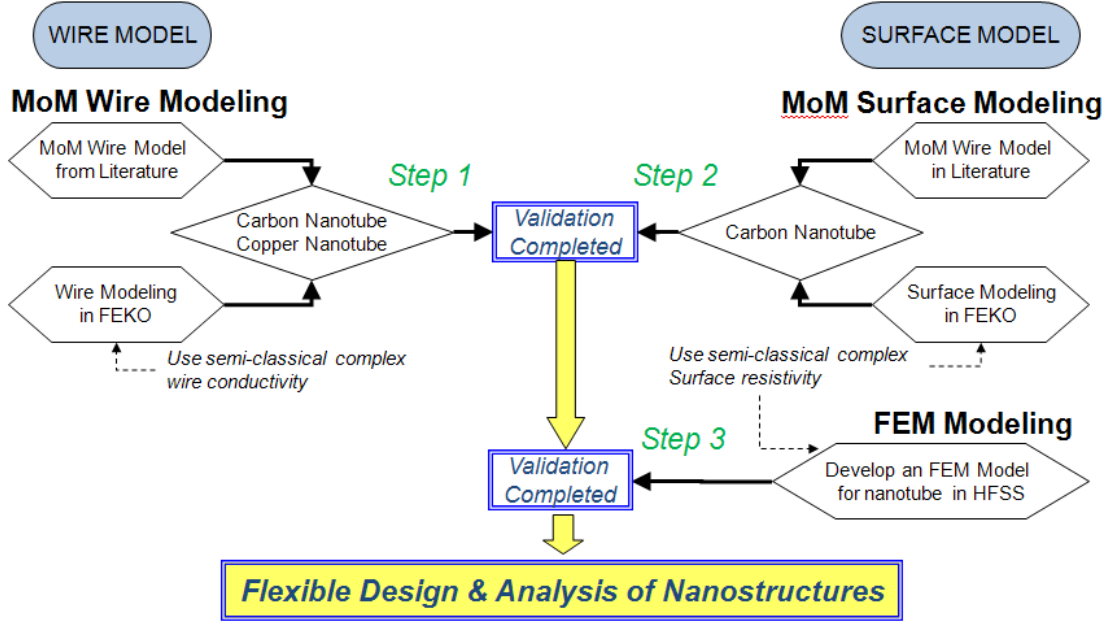


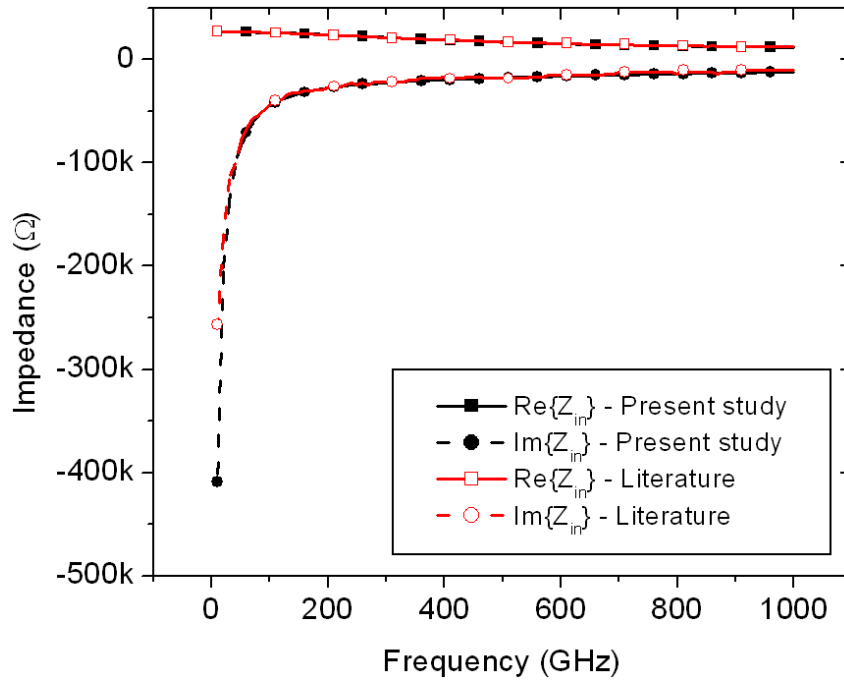
Fig. 4.1 Modeling approach and three step validation flow chart. The paper referred in the chart is reference [8].

polaritons [8] and are quite different than the length-based resonances.

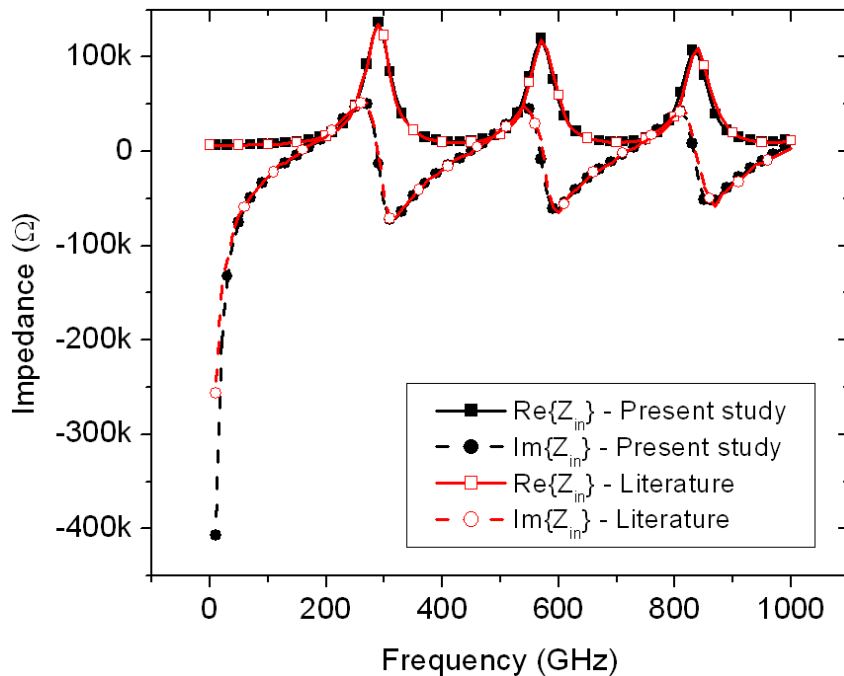
The comparison between characteristic impedances of nano-coaxial lines computed with FEM and MoM surface models (step 3 in Fig. 4.1) is shown in Fig. 4.3. The radius of the inner conductor made from CNT is 2.712 nm. The inner radius of the outer conductor (made from tungsten) is varied from 4.86 to 14.36 nm. Z_{c_conv} on the x-axis represents the characteristic impedance of a conventional coaxial line computed as [74]

$$Z_{c_conv} = \frac{60\ln(b/a)}{\sqrt{\epsilon_r}} (\Omega), \quad (4.5)$$

where a (= 2.712 nm) is the radius of the inner conductor, b (4.86 nm – 14.36 nm) is the



(a) MoM wire models of Cu nanotube dipole antennas



(b) MoM surface models of CNT dipole antennas

Fig. 4.2 Computed input impedances from MoM models and comparison with literature [8]. (a) Wire model of a Cu dipole, and (b) surface model of a CNT dipole.

inner radius of the outer conductor, and ϵ_r is the permittivity of the dielectric between inner and outer conductor in the coaxial line (air). It is assumed that the thickness of the outer conductor is much larger than the skin depth and that the length of the line is 1 μm . The results show that the two full-wave models correlate well with each other. Note that the impedance is much higher than the impedance computed using a conventional approach (4.5) because of an intrinsically high resistance of CNTs (an individual SWCNT has 6.5 $\text{k}\Omega$ intrinsic resistance).

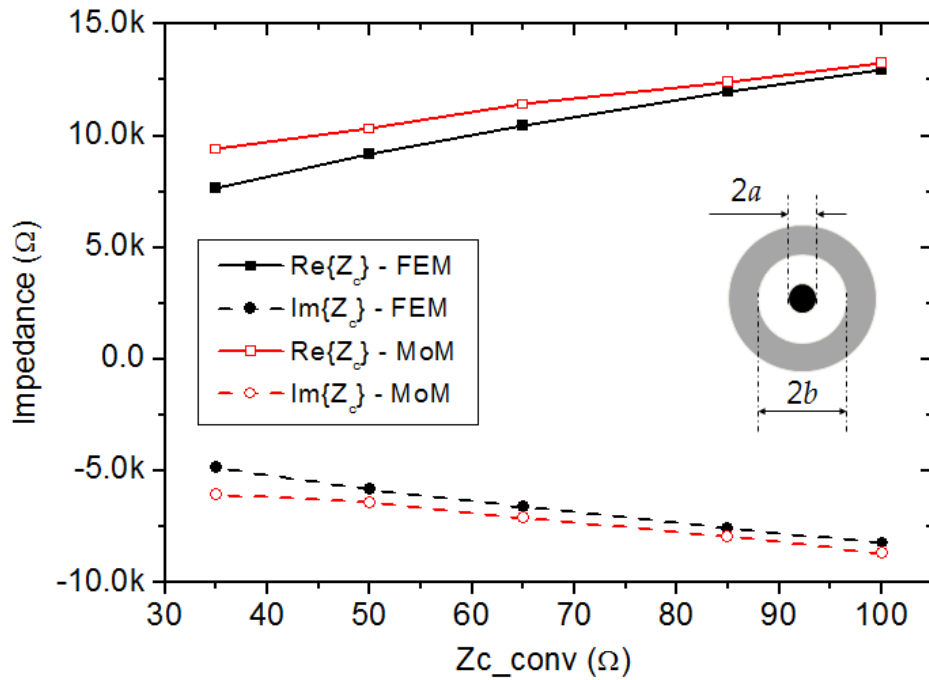


Fig. 4.3 Computed characteristic impedances from the FEM and MoM models of the nano-coaxial line having a CNT inner conductor. For x-axis, the radius of inner conductor is fixed but the inner radius of the outer conductor varies to give an impedance Z_{c_conv} from the conventional formula (4.5). ($a = 2.712 \text{ nm}$, $b = 4.86 \text{ nm} - 14.36 \text{ nm}$).

4.1.2. Evaluation Parameters

In order to assess the performance of CNT interconnects, several parameters are computed for each interconnect application. The parameters include impedance, gain, propagation constant, insertion loss, and slow wave factor. Input impedance for wireless interconnects, such as antennas, and characteristic impedance for transmission lines have to be conjugate matched to a source and a load to deliver maximal power. Because of the very high intrinsic resistance of CNTs, impedance matching with CNTs is a critical issue that needs to be solved.

The second parameter used for evaluation is antenna gain, which for the individual CNT dipole antenna is expected to be about -53 dBi [8]. Power transmission which can be assessed with wireless interconnect transfer function $|S_{21}|$ is proportional to the gain. Therefore, increasing the antenna gain is another goal in the design process. The two parameters, impedance and gain, can be improved when a number of CNTs are used to form a bundle, which will be discussed in Chapter 5.

A propagation constant (γ) for CNT transmission lines, which is composed of an attenuation constant ($\alpha = \text{Re}\{\gamma\}$) and a phase constant ($\beta = \text{Im}\{\gamma\}$), is also evaluated. The attenuation constant is dependent on line medium and line dimensions, and is also related to the transmission parameter S_{21} as [91]

$$\alpha (\text{dB/m}) = 20 \frac{\log|S_{21}|}{d}, \quad (4.6)$$

where d is the line length. Line loss can be estimated from $|S_{21}|$ when the line is uniform and the reflection is small. However, if the reflection is not small, the insertion loss (IL) is computed as

$$IL \text{ (dB)} = -10 \log \left(\frac{|S_{21}|^2}{1 - |S_{11}|^2} \right). \quad (4.7)$$

The phase constant is useful to estimate wave velocity on the line. A slow-wave factor (F_{SW}), which represents a measure for the reduction of a wave velocity on the line compared to the speed of light, is computed as

$$F_{SW} = \frac{c}{\omega/\beta}, \quad (4.8)$$

where c is the speed of light, and ω is the angular frequency.

4.2. Interconnect Applications

4.2.1. Wireless Interconnect with CNT Antennas

Since polarization- and length-dependent optical properties of CNTs to illumination have been reported experimentally [52], CNT dipole antennas have been proposed to wirelessly interconnect nanoscale and macroscopic systems [53]. Because of the CNT's large slow-wave factor of 50 to 100, it is suggested that very small nano-

antennas are feasible. Fig. 4.4 shows the modeling setup used to evaluate a wireless interconnect with a CNT dipole and a half-wavelength PEC dipole. Performance of this interconnect is examined at 160 GHz. Note that the CNT dipole cannot resonate below about 50 GHz [8]. Also, the CNT dipole is much smaller than the PEC dipole, as shown in the figure, even though they resonate at the same frequency. Three cases are considered: two-CNT dipoles separated by 1 μm and 100 μm , and a CNT dipole - half-wavelength PEC dipole (length 917 μm , width 0.1 μm) pair separated by 100 μm .

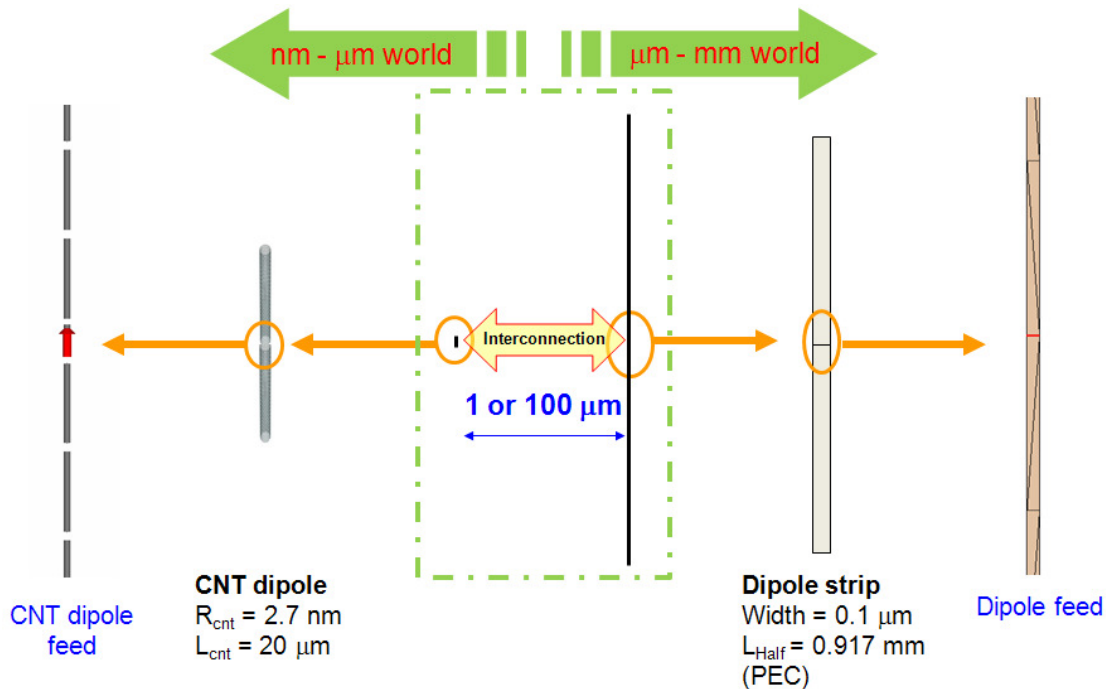


Fig. 4.4 Modeling setup used to evaluate wireless interconnecting scheme.

Reflection coefficients for CNT and PEC dipoles when the distances between them are 1 μm and 100 μm are shown in Fig. 4.5. When their separation is 1 μm , the best

CNT dipole match is shifted to a lower frequency, while that for the PEC dipole is unchanged. It appears that the CNT is affected by the PEC dipole through the proximity coupling, however, the CNT is too small and lossy to affect the PEC dipole. Transmission, S_{21} in dB, for each pair is computed and shown in Fig. 4.6. The maximum transmission is seen to be about -11 dB for the CNT-CNT pair at 1 μm distance. For 100 μm separation, 24 dB lower transmission with the CNT-CNT is shown when compared to the CNT-PEC dipole pair. This is due to the extremely low efficiency of the CNT dipole (gain < -50 dB). Results for the above three cases show that these of individual CNTs in a wireless interconnect can be practical only with very small, (sub)micron distance.

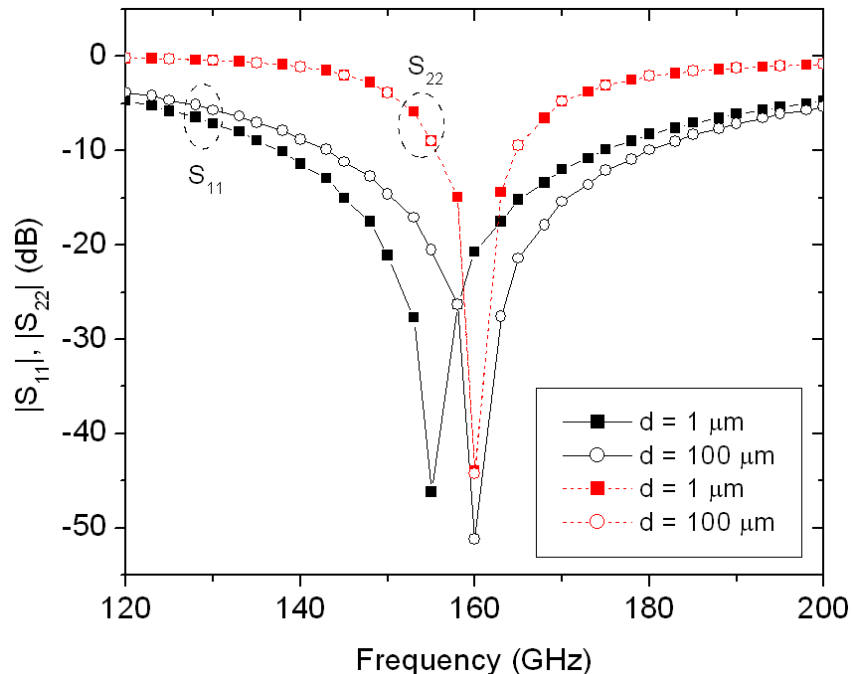


Fig. 4.5 Computed reflection coefficients of CNT-PEC dipole antennas used in studied wireless interconnects. Port 1 (S_{11}) is the CNT dipole and port 2 (S_{22}) is the PEC dipole.

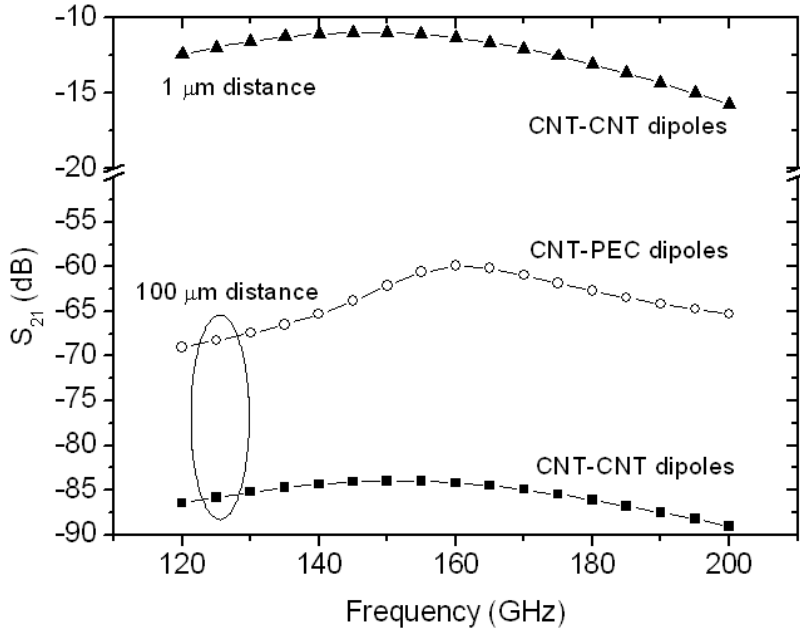


Fig. 4.6 Computed transmissions (S_{21}) for three cases: the CNT-CNT dipole pair separated by $1\text{ }\mu\text{m}$ and $100\text{ }\mu\text{m}$, and the CNT-PEC dipole pair separated by $100\text{ }\mu\text{m}$.

4.2.2. Nano-Coaxial Lines

Effects of dielectric loading and cross-sectional dimensions on nano-coaxial line loss, characteristic impedance, and slow-wave factor are studied in this section. It has been shown that ALD can be used to sequentially coat a single CNT with alumina (Al_2O_3) and tungsten (W) with realized cross-sections resembling a traditional coaxial line [87]. A transmission electron microscopy (TEM) image of a cross section of the ALD-coated CNT line and its coaxial line model are given in Fig. 4.7. An ALD-enabled alumina dielectric is placed between the nano-CNT/Cu-core and the shield (alumina is typically used in ALD, $\epsilon_r = 10$). The inner conductor of CNT or Cu has a radius of 2.712 nm and the dielectric is either air or alumina. The outer conductor is assumed to be much thicker than the skin depth and is made from tungsten.

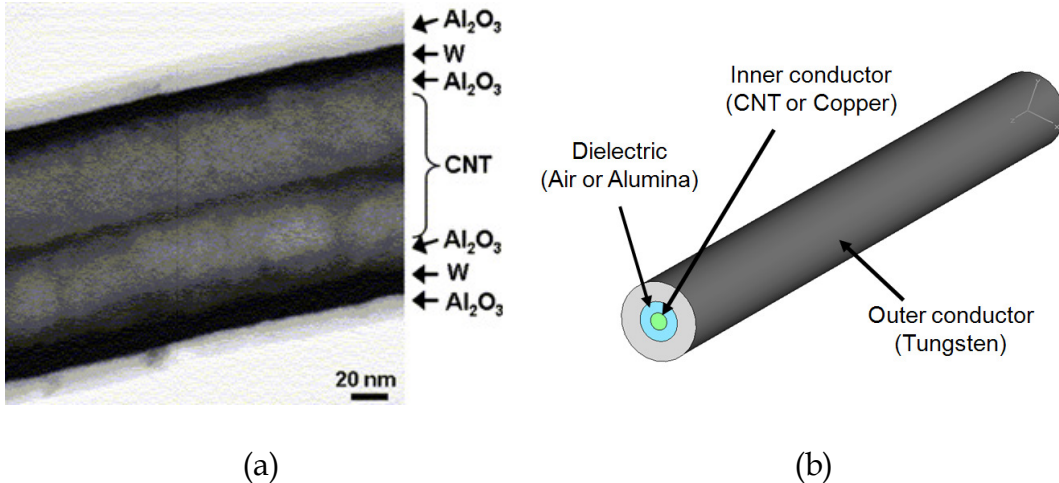
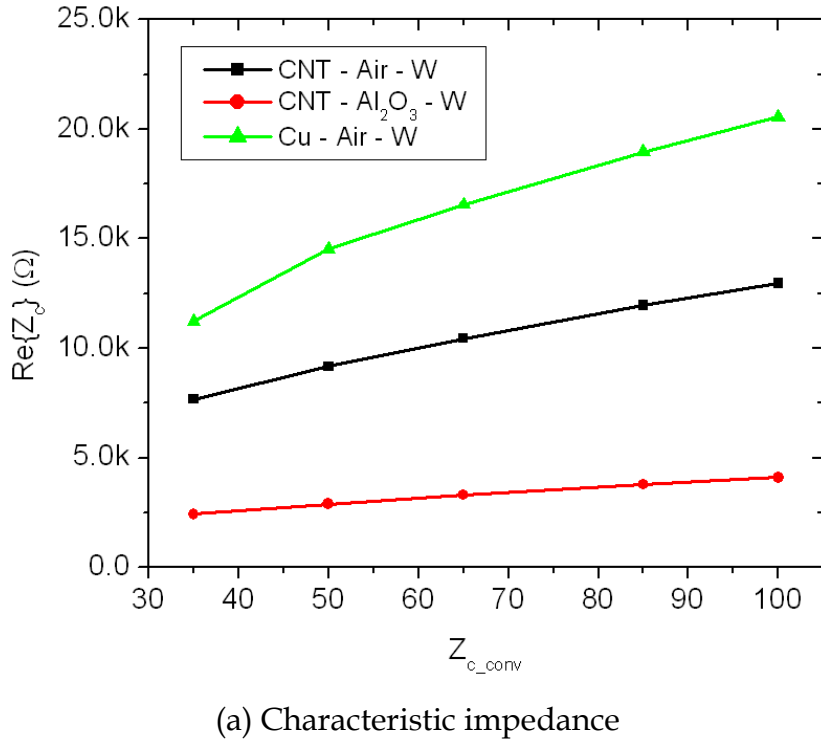


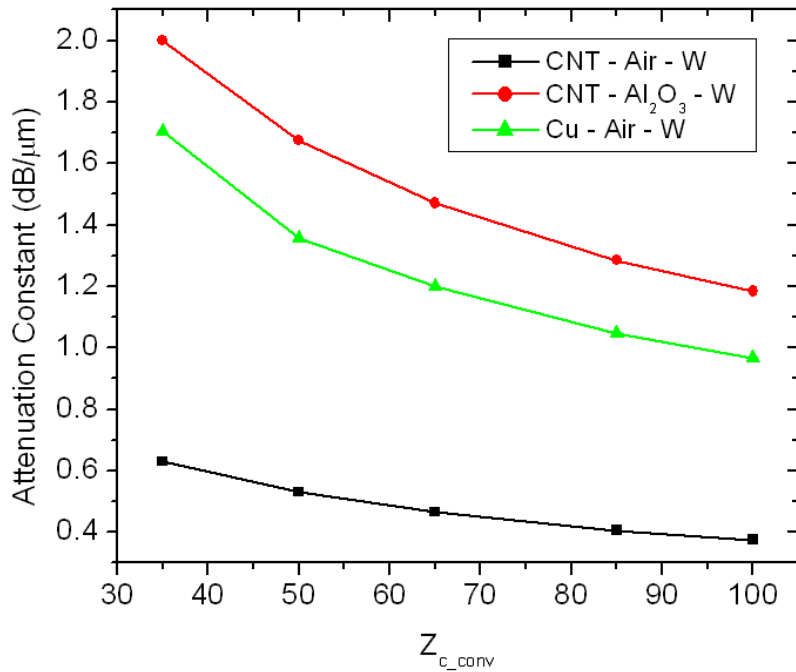
Fig. 4.7 TEM image of a cross section of ALD CNT coated with Al_2O_3 and tungsten (W) [87] (a), and its computational model (b).

The characteristic impedance and the propagation constant of a CNT-coax and a Cu-coax are computed for three cases: CNT-Air-W, CNT- Al_2O_3 -W, and Cu-Air-W. The real part of the characteristic impedance and the attenuation constant computed at 25 GHz are shown in Fig. 4.8. The results are plotted versus the conventionally calculated characteristic impedance (4.5), which is a function of the inner radius of the outer connector. As seen, the alumina dielectric leads to a lower impedance and higher loss (attenuation constant) compared to air dielectric. Also, the CNTs have better performance (lower impedance and loss) than Cu nanotubes of the same size. Mismatch losses are excluded from these results.

Effect of nanotube's size on performance of ALD-coated CNT coaxial lines is also investigated. The radii of 2.712 nm and 10 nm for CNTs and Cu nanotubes are used. The dielectric is assumed to be Al_2O_3 . Fig. 4.9 shows the characteristic impedance and attenuation constant for the CNT-coax and the Cu-coax at 25 GHz. Results show that



(a) Characteristic impedance



(b) Attenuation constant

Fig. 4.8 Effect of dielectric loading on (a) the characteristic impedance and (b) the attenuation constant of CNT coaxial lines, and performance comparison between CNT and Cu at 25 GHz.

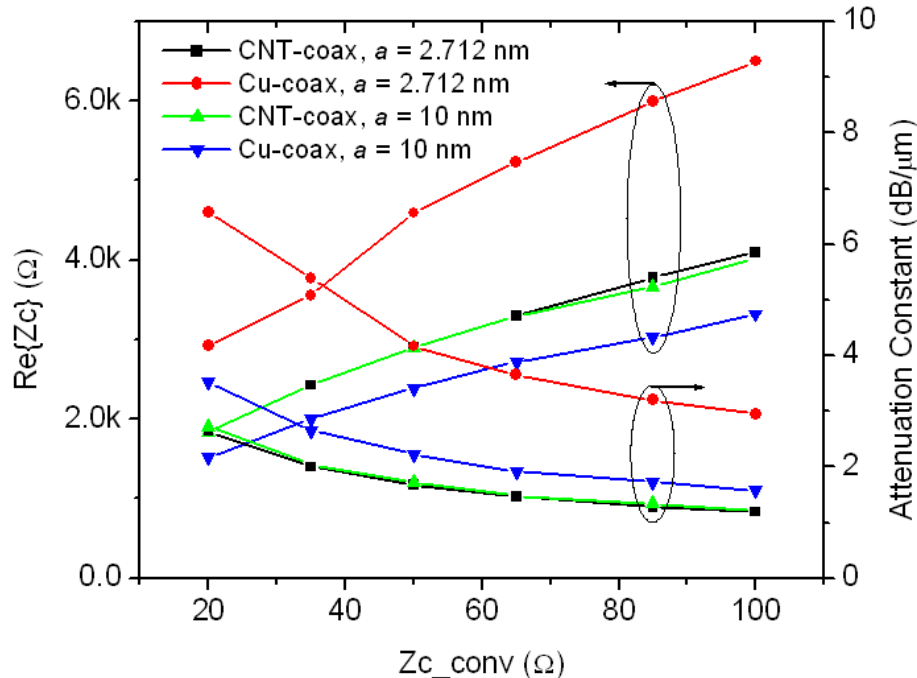


Fig. 4.9 Characteristic impedance and attenuation constant of coaxial lines with a CNT or Cu nanotube inner conductor at 25 GHz. The radius of both CNT and Cu nanotube is fixed at 2.712 nm or 10 nm. Note that the impedance and attenuation constant for the two radii of CNTs are the same.

the CNT-coax has lower impedance and a smaller attenuation constant than the Cu-coax when their radii are small ($a = 2.712 \text{ nm}$). However, the impedance of the CNT-coax is higher than its Cu-based counterpart if the radii are larger ($a = 10 \text{ nm}$). Note that CNTs always have lower loss than Cu. In addition, there is no change in the impedance and attenuation constant of CNT coaxial lines for the two radii because the effect of CNT's radius is cancelled out in (4.1) and (4.2).

4.2.3. Single Wire Transmission Lines

Single wire transmission lines have been shown to have lower loss than coaxial lines. However, since the propagating mode is not TEM, the fields are guided over a

larger volume so that increased distance from the ground is needed and the coupling with other lines is stronger. To overcome some disadvantages, Goubau proposed the use of a dielectric layer as a coating to the wire transmission line [88]. The distance between the signal line and neighboring lines or the ground is reduced with the dielectric layer confining fields around the line. The drawback is the increased loss. An uncoated single wire line is usually referred to as Sommerfeld line, while the coated structure is known as Goubau line. To validate the modeling approach, FEM simulations are compared with Cu-based Sommerfeld lines proposed as THz interconnects in [92]. Results shown in Fig. 4.10 provide high confidence in the validity of results from this study.

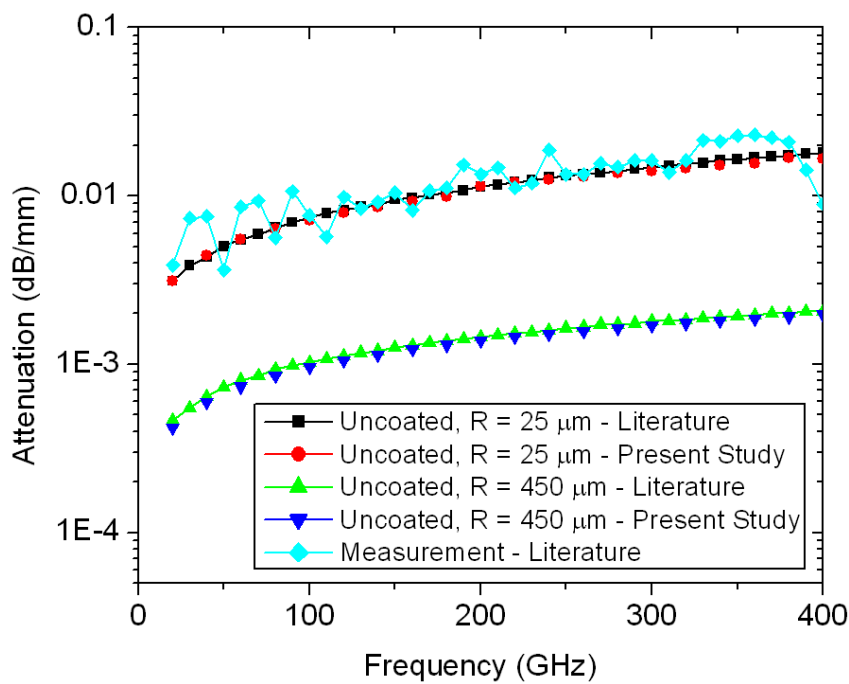


Fig. 4.10 Validation of FEM modeling for Sommerfeld lines with results in literature [92].

Since coated CNT lines can be built by applying an ALD technique on individual CNTs, several structures with different ALD-compatible coatings are studied. First, CNT lines and Cu lines without coating and with 10 nm-thick Al_2O_3 coating are considered. Simulated results for those lines at 25 GHz are summarized in Table 4.1. Results show that CNTs provide lower impedance and line loss than Cu nanotubes. Even though their impedances are very high, respective line losses are significantly reduced when compared with the nano-coaxial structures discussed in Section 4.2.2.

Table 4.1 Characteristic impedance (Z_c) and line losses per μm of single wire CNT lines and Cu lines. Radius of the nanotubes is 2.712 nm.

Characteristic Parameters	No Coating		10 nm thick Al_2O_3 Coating	
	CNT	Cu	CNT	Cu
Z_c (k Ω)	20.8	33.0	17.8	28.2
S_{21} (dB/ μm)	0.24	0.60	0.27	0.68

The attenuation characteristics for the uncoated CNT lines and for the CNT lines with 1 nm, and 10 nm thick coating layers are also computed. They are compared to other interconnecting schemes (wireless interconnects and nano-coaxial lines) investigated previously in the next section.

4.3. Discussion

Various interconnecting schemes with metallic SWCNTs are investigated in Section 4.2, that is, wireless interconnects with CNT dipole antennas, nano-coaxial lines with CNTs as their inner conductor, and single wire CNT Sommerfeld and Goubau

lines. It is seen that the CNT-based interconnects have superior electrical performance when compared to their Cu-based counterparts. That is expected because it is known that metallic CNTs have better electrical properties (i.e. higher conductivity) than other conventional nanoscale conductors. However, as seen, the use of individual CNTs produces very high impedance and loss because of their *small* size. To overcome the drawback of high impedance and loss, the use of a number of CNTs in a bundle has been proposed. This is further discussed in Chapter 5.

The transmission effectiveness of the interconnecting schemes studied here as characterized by $|S_{21}|$ is shown in Fig. 4.11. The specific configurations include 1) wireless interconnects with CNT - CNT pair and CNT - PEC dipole pairs; 2) CNT coaxial lines with Al_2O_3 dielectric layers of 10 nm, 50 nm, and 100 nm; and 3) single wire CNT Goubau lines without coating and with 1 nm- and 10 nm-thick coatings. The length of communication for all configurations is varied from 1 μm to 200 μm . The frequency is set at 70 GHz since the resonance of the CNT dipole is suppressed below the relaxation frequency of ~ 53 GHz [8]. For the resonance at 70 GHz, the CNT dipole with 2.712 nm radius has a length of 64.12 μm and a resistance of about 45 $\text{k}\Omega$. A PEC strip dipole with 100 nm width is 2.09 mm long and its resistance is 72 Ω . As seen, all configurations exhibit a very high loss past a few μm length of interconnect. The wireless interconnect produces the worst performance at short distances and the best performance at longer distances, even though the values of $|S_{21}|$ are likely impractical. Finally, as in the classical case, the single wire transmission lines are less lossy when compared with the CNT coax lines.

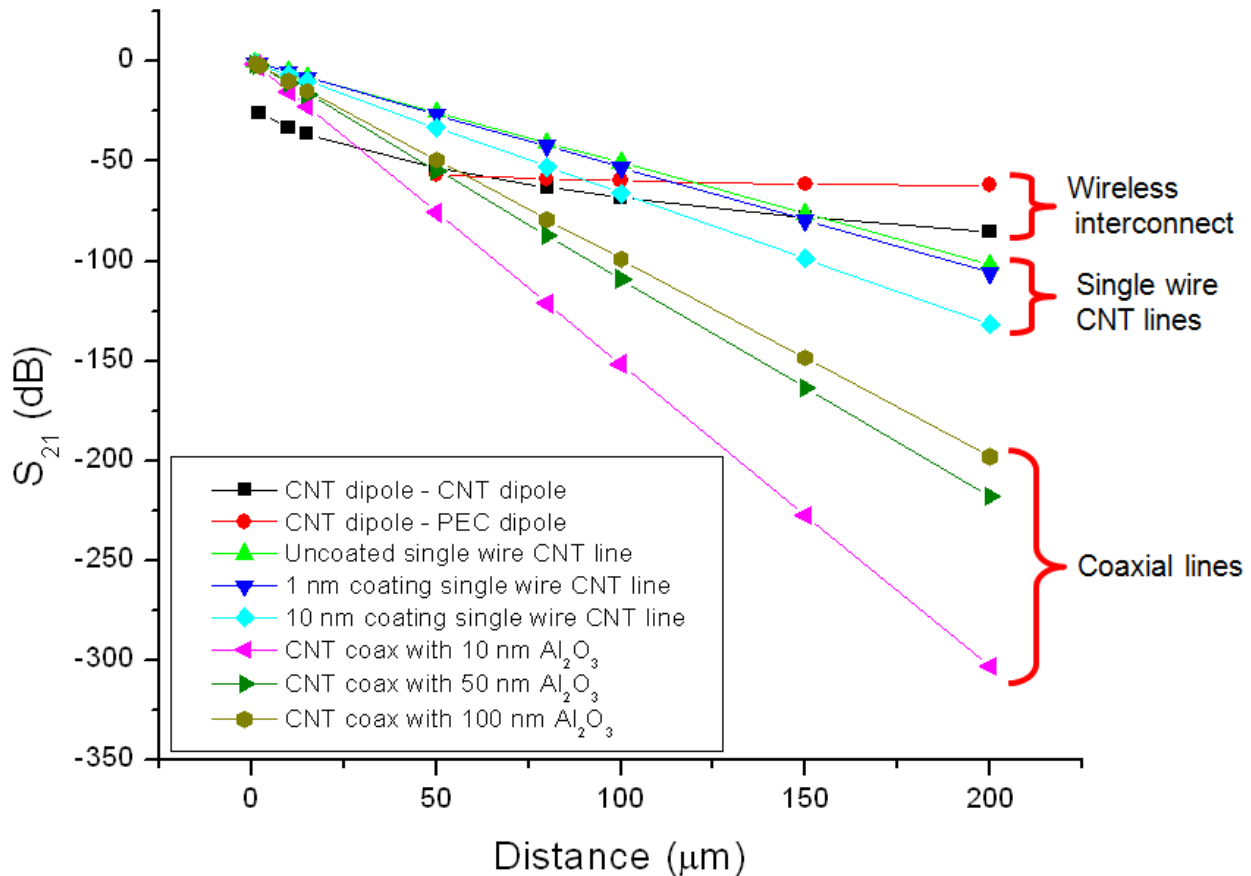


Fig. 4.11 Computed transmission for studied interconnect schemes: wireless interconnects with CNT dipole antennas, single wire CNT lines, and CNT coaxial lines.

CHAPTER 5

CHARACTERIZATION OF CARBON NANOTUBE BUNDLES AND APPLICATIONS

Carbon nanotubes (CNTs) are a promising candidate for future nano-systems due to their excellent electrical, mechanical, and thermal properties as compared to conventional materials [34]. Metallic CNTs are thus considered for the nanoscale microwave interconnects as antennas or traditional transmission lines [93]. However, it is also known that individual CNTs have high loss and very high impedance as interconnects, thus introducing a major problem for their use, as shown in Chapter 4. To reduce their impedance and loss the CNT bundle is proposed [94], and its application as vertical vias in multi-layered integrated circuits [95, 96] has been proposed. While various circuit models and equivalent transmission line models have been proposed for investigating CNTs, their full-wave analysis and design are still in infancy. Typical full-wave studies are conducted with fundamental geometries such as a dipole and a single CNT wire over a ground plane [8, 97].

In this chapter, microwave interconnect configurations composed of a bundle of CNTs are discussed. A CNT bundle monopole antenna, a nano-coaxial line with the inner conductor composed of a CNT bundle, and a single wire transmission line with

CNT bundle are investigated. All CNTs considered are metallic single walled and their performance is compared with Cu-based counterparts. Full-wave simulations in either MoM or FEM are conducted taking into account quantum effects on CNTs. The interconnect design and analysis are performed after a thorough modeling validation over the wide microwave spectrum. Obtained results show that performance of the interconnects with CNT bundles are superior to that of the Cu-based structures when the CNTs possess a smaller diameter and a larger number of CNTs comprise the corresponding bundles.

This chapter is organized as follows:

- Section 5.1 briefly reviews some experimentally found properties of CNT bundles and several modeling approaches investigated by other groups. These approaches include circuit and equivalent transmission line models, and multi-conductor or multi-shell models. Modeling methods applied in this study are also described.
- Section 5.2 discusses the application of CNT bundles as wireless interconnects. MoM modeling validation is conducted for CNT bundle dipole with respect to the number of CNTs. Then, CNT bundle monopole antennas are designed for matching to 50Ω and their input impedance, gain, and efficiency are compared to their Cu-based counterparts.
- Section 5.3 demonstrates performances of nano-coaxial lines with a CNT bundle as their inner conductor. Bundles composed of identical CNTs or mixed CNTs

are modeled in FEM to evaluate their characteristic impedance, line loss, and slow-wave factor. These parameters are compared to those of the Cu-based coaxial line. CNT filling factor is defined and used for performance assessment.

- Section 5.4 discusses characteristics of single wire transmission lines made from a CNT bundle. Sommerfeld and Goubau lines with 10 nm dielectric coating are modeled in FEM, and their performance is compared with Cu-based Goubau lines with the same coating.

5.1. Carbon Nanotube Bundle Modeling

Since the introduction of CNT bundles [98], many research groups have investigated their properties, fabrication approaches, and possible applications. Some of the CNT bundle properties that have been discovered include:

- A CNT bundle can be composed of hundreds of (non)identical metallic CNTs [98];
- The metallic CNTs comprise about a third of all CNTs in the bundle [99]. The remaining CNTs are semiconducting.
- Resistance and inductance of the CNT bundle are inversely proportional to the number of CNTs [94].
- The lattice constant, defined as the minimum distance between neighboring CNTs, is $D_{\text{CNT}} + 0.34 \text{ nm}$ [98], where D_{CNT} is a CNT diameter, as shown in Fig. 5.1.

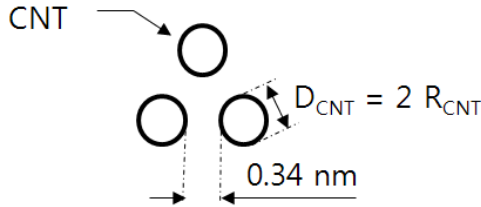


Fig. 5.1 Lattice constant of a CNT bundle, $D_{\text{CNT}} + 0.34 \text{ nm}$. R_{cnt} is CNT's radius.

For theoretical understanding, studies, and design, various modeling methods for CNT bundles are proposed. Circuit and transmission line models are reported in [94, 100-102]. The models are developed with a quantum resistance of $6.45 \text{ k}\Omega$, a kinetic inductance of 16 nH , and a quantum capacitance of about 100 aF per unit length (μm) for a single CNT. Therefore, the resistance and inductance of a CNT bundle are obtained by dividing by the number of the CNTs in the bundle, while capacitance should be multiplied. When the bundle is composed of identical metallic CNTs, the CNTs at a certain distance from the center of the bundle can be considered as a larger equivalent metallic tube which has a radius equal to that distance. This idea is the basis for the multiconductor transmission line, an equivalent single conductor model [103, 104], and equivalent multishell [105] models. Combining the transmission line model and CNT's quantum effects, hybrid transmission line-quantum mechanical models are proposed in [106]. All methods above assume that inter-coupling between CNTs is negligible.

With current fabrication technologies, the CNT bundles are composed of a mixture of metallic and semiconducting CNTs or SWCNTs and multi-walled CNTs (MWCNTs). A CNT bundle with one-third population of metallic CNTs will not

produce better electrical performance than the one fully populated with metallic CNTs. Recently, several techniques aimed to separate individual CNTs are reported [65-68]. Thus, densely packed bundles with only metallic CNTs are expected to be feasible in the near future.

In this thesis, modeling of CNT bundles as microwave interconnects is carried out to evaluate their performance, specifically impedance matching, efficiency, and line loss. The specific configurations include CNT bundle monopole antennas, nano-coaxial lines, and single wire lines, similar to those in Chapter 4. The modeling is conducted using full-wave MoM and FEM with included quantum effects and mutual effects of neighboring CNTs. The CNT bundles studied here are assumed to be densely packed with only metallic SWCNTs separated by their lattice constant.

5.2. Wireless Interconnects

In Chapter 4, dipole antennas are used to assess the quality of wireless interconnects with CNTs. When a large number of CNTs are used in modeling a dipole bundle, the computational overhead is expected to increase significantly. On the other hand, a monopole reduces computational resources compared to a corresponding dipole. Therefore, wireless interconnects with CNT bundles are investigated with monopole antennas. Modeling validation is performed with different numbers of CNTs. In order to design a CNT bundle monopole that is well matched to 50Ω , effects of the separation between CNTs and the number of CNTs in the bundle are studied.

Performance of the designed CNT bundle monopole is compared to that of the Cu monopole of the same size.

5.2.1. Modeling Validation

Modeling validation for CNT bundle monopoles is carried out by comparison with published multishell modeling approach with dipole antennas [105]. CNT bundle dipoles with 7, 19, and 55 CNTs are considered. It is assumed that all CNTs are identical, metallic, and single-walled. CNTs are densely packed, thus the separation between neighboring CNTs is the same as the lattice constant ($D_{CNT} + 0.34$ nm). Zigzag (21, 0) CNTs with 1.644 nm diameter are used. The top views of the three studied CNT bundle dipoles are shown in Fig. 5.2, and obtained results are summarized in Table 5.1. MoM computed resonant frequency for the 55 CNTs bundle and efficiency at 27 THz for all three bundles are compared with literature [105]. As seen, excellent agreement is obtained thus providing a great confidence in the following studies. Single CNT performance is also included for easy assessment of the trends due to a bundle arrangement.

5.2.2. CNT Bundle Monopole Antennas

To determine bundle effects on antenna performance and come-up with design guidelines, the separation between CNTs and the number of CNTs in the bundle are studied. Effects of separation between CNTs on antenna performance are studied first. Two CNTs are placed over the ground plane and are separated by 7.5 nm. They are

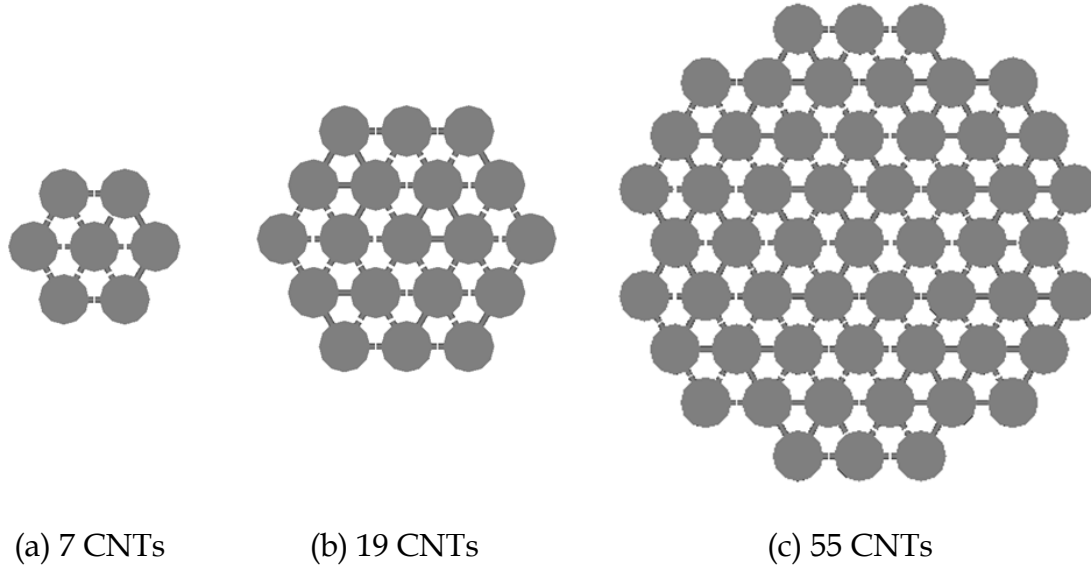


Fig. 5.2 Top view of various CNT bundle dipoles of (a) 7 CNTs, (b) 19 CNTs, and (c) 55 CNTs.

Table 5.1 Validation of MoM modeling for CNT bundle dipole antennas with results from [105].

	Resonant Frequency	Efficiency (%) at 27 THz			
Number of CNTs	55	1	7	19	55
CNT Length	1 μm	0.0755 μm	0.192 μm	0.32 μm	0.54 μm
MoM	16 THz	0.0013	0.03	0.1	0.49
Literature	17 THz	0.0013	0.03	0.1	0.5

connected at their base by a perfect electric conductor (PEC) wire to form a monopole antenna as shown in Fig. 5.3 (a). The contact impedance is neglected as its value is not known at the time. For a chosen CNT radius, R_{CNT} , of 2.712 nm and length, 10 μm , a single CNT monopole resonates at 160 GHz. The separation distances $D = 3R_{\text{CNT}}$, $10R_{\text{CNT}}$, and $50R_{\text{CNT}}$ are considered and simulated input impedances are shown in Fig. 5.4. As seen, the resonant frequency f_0 is lowered as the separation D becomes larger: $f_0 = 215$ GHz for $D = 3R_{\text{CNT}}$, $f_0 = 205$ GHz for $D = 10R_{\text{CNT}}$, and $f_0 = 195$ GHz for $D = 50R_{\text{CNT}}$.

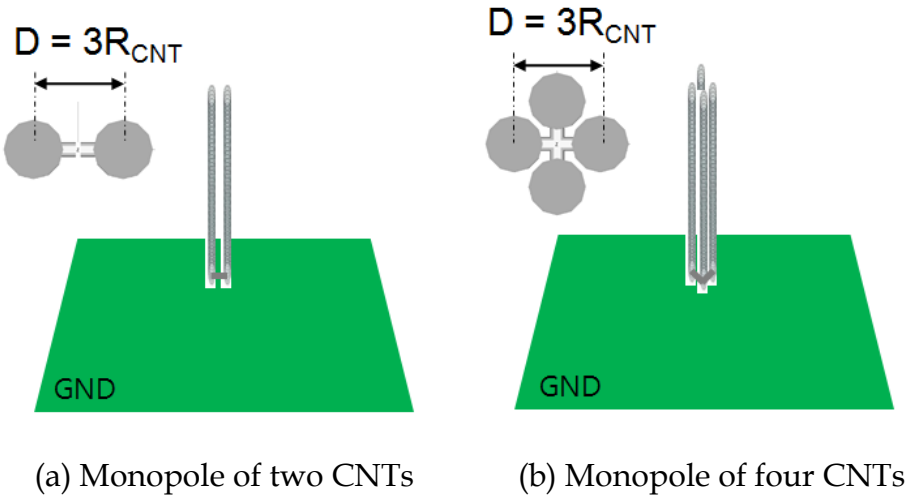


Fig. 5.3 CNT bundle monopoles of (a) two CNTs and (b) four CNTs over a ground plane. R_{CNT} is the radius of the CNTs. The CNTs are connected at their base by a PEC wire.

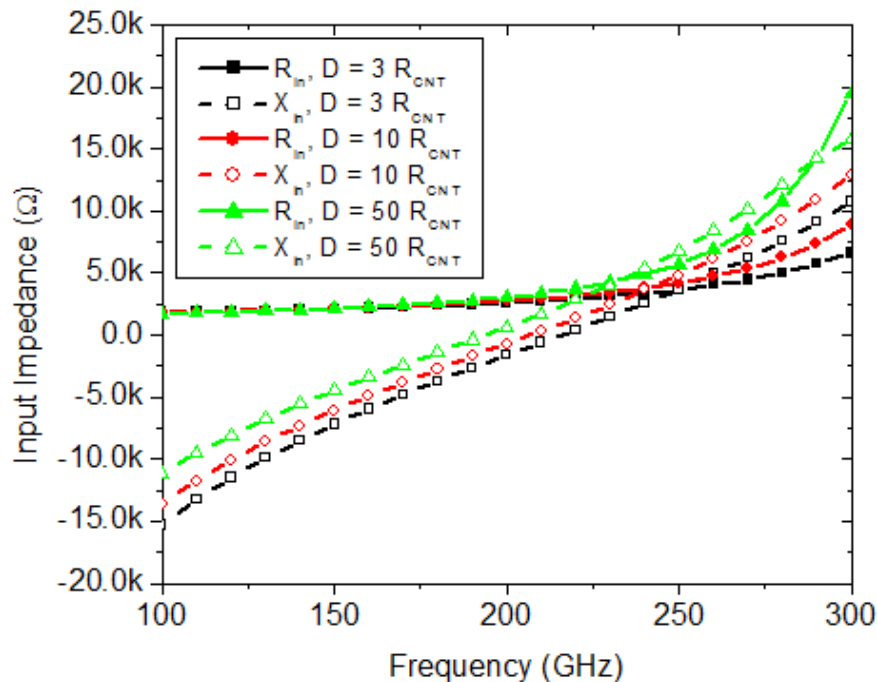


Fig. 5.4 Simulated input impedance of two-CNT monopoles shown in Fig. 5.3 (a) for different separations: $D = 3R_{\text{CNT}}$, $10R_{\text{CNT}}$, and $50R_{\text{CNT}}$. The radius of the CNTs, R_{CNT} , is 2.712 nm, and their length is 10 μm at which a single CNT monopole resonates at 160 GHz.

Clearly, the resonant frequency of a monopole (dipole) is affected by the density of metallic CNTs in the bundle. Their input resistance and gain at each resonant frequency are $2.9 \text{ k}\Omega$ and -45 dBi , respectively, and no difference in the two parameters is found between the three separation distances.

Next, the computational studies with seven CNTs are conducted with four configurations as shown in Fig. 5.5: dense bundle, sparse bundle, cone-shaped bundle A, and another cone-shaped bundle B (the inverted version of cone-shaped A). Conical shapes are considered to model geometrical cases where many CNTs have more defects or breaks as the CNTs go through from one end to the other, so that the bundle may have different diameters at the both ends. The separation between CNTs for the dense bundle is equal to the lattice constant, while the separation for the sparse bundle is 10 times the lattice constant. The cone-shaped bundles have CNTs spacing with the lattice constant at one end and 10 times the lattice constant at the other. Obtained input impedances are shown in Fig. 5.6. Similarly as before, the sparse bundle resonates at a lower frequency than the dense bundle. It is also observed that the cone-shaped A configuration has lower resonant frequency than the cone-shaped B which is wider at its feed. Again, the resonant frequency is affected by the shape of the bundle. Note that the effects of CNT's separation for monopole antennas cannot be obtained from a circuit-based modeling approach. Also, the equivalent currents on each CNT are affected by the currents flowing on their neighbors via free-space Green's function. The final result is a 'steady-state' solution that takes into account all coupling effects.

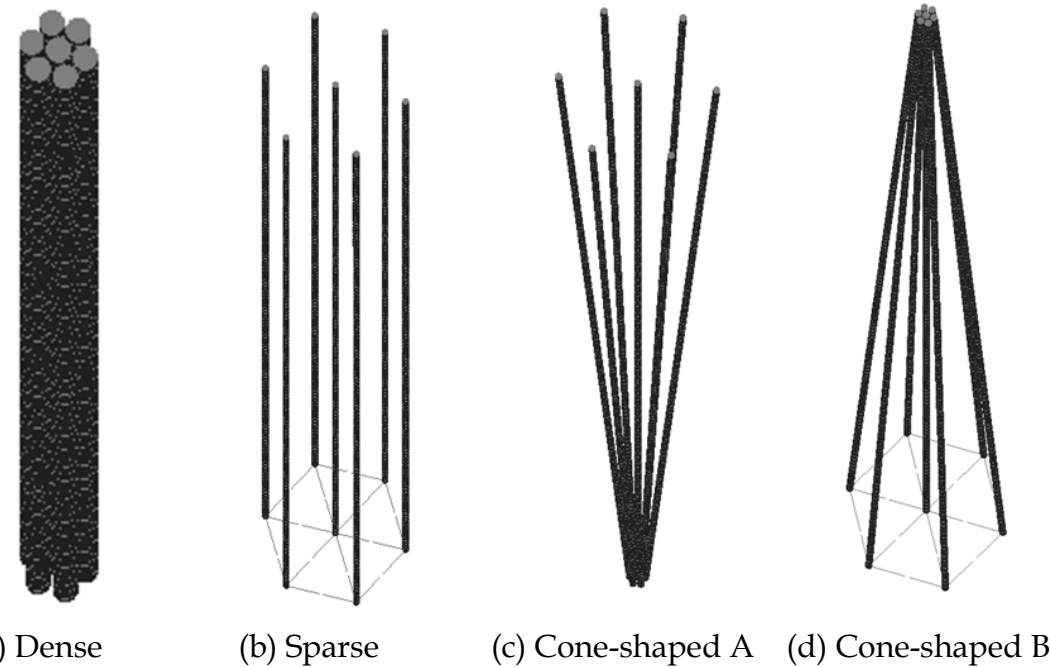


Fig. 5.5 Various CNT bundle monopole configurations with 7 CNTs. (a) Dense bundle with $D = D_{\text{CNT}} + 0.34 \text{ nm}$, (b) sparse bundle with $D = 10(D_{\text{CNT}} + 0.34 \text{ nm})$, (c) cone-shaped A with $D_{\text{Bottom}} = D_{\text{CNT}} + 0.34 \text{ nm}$ and $D_{\text{Top}} = 10(D_{\text{CNT}} + 0.34 \text{ nm})$, and (d) cone-shaped B with $D_{\text{Bottom}} = 10(D_{\text{CNT}} + 0.34 \text{ nm})$ and $D_{\text{Top}} = D_{\text{CNT}} + 0.34 \text{ nm}$.

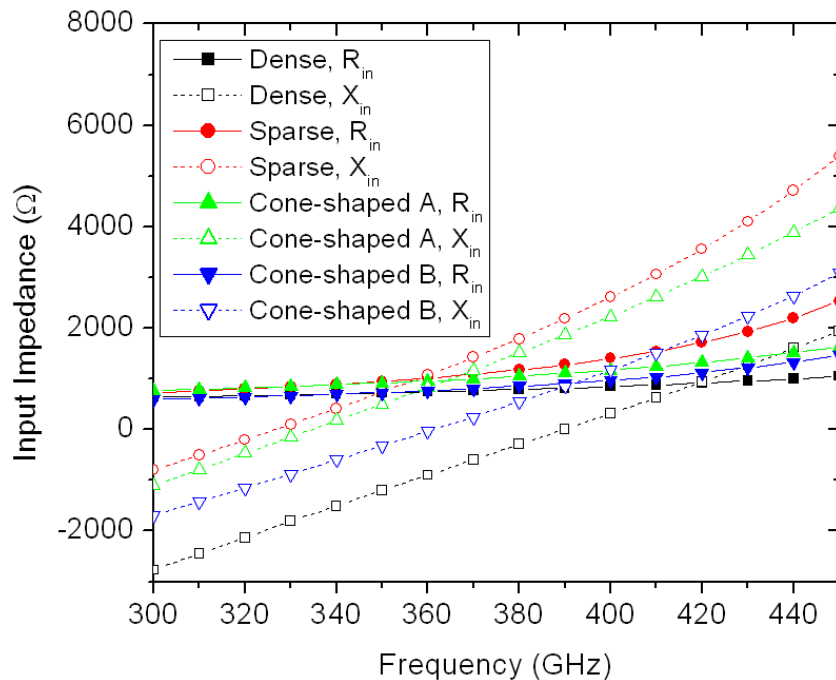


Fig. 5.6 Simulated input impedance of various shaped monopoles with 7 CNTs shown in Fig. 5.5.

The number of CNTs in the bundle is studied next. Since the resistance of the bundle is inversely proportional to this number, the input resistance of CNT bundle monopoles is expected to decrease as the number of CNTs increases. Two-CNT and four-CNT bundle monopoles shown in Fig. 5.3 are considered. The radius and the length of CNTs are 2.712 nm and 10 μm , respectively, and separation between CNTs is kept at $3R_{\text{CNT}}$. The obtained input impedance for the two CNT bundle monopoles is given in Fig. 5.7. As seen, the monopole with four CNTs resonates at a higher frequency, 300 GHz, compared to that with two CNTs at 215 GHz. The resonant resistance for the four-CNT bundle monopole is, however, decreased from 2.9 k Ω (for two- CNT bundle monopole) to 1.4 k Ω . A simple scaling indicates that 60 CNTs bundle monopole will have about a 100 Ω resonant resistance which results in a VSWR of approximately 2:1 with respect to 50 Ω . The gains for the two-CNT and four-CNT bundles are computed to be -44 dBi and -38.5 dBi, respectively. Overall, more CNTs result in lower input resistance, higher resonant frequency, and higher gain. As with earlier studies, the effects of contact impedance are not considered.

Based on the above results, a densely packed bundle monopole with 61 CNTs is designed. This antenna is expected to have VSWR of about 2:1. Also, another monopole with 85-CNT bundle is designed. The lengths of CNTs are fixed at 10 μm . Top views of the two CNT bundle monopoles are shown in Fig. 5.8. All CNTs are connected by PEC wires at their base (no contact impedance). For comparison with relevant Cu based monopole, a single Cu wire monopole is modeled with the same diameter of 52.8 nm as the 85-CNT bundle. The conductivity for the Cu wire is $2.7\text{e}^7 \text{ S/m}$ [4]. Computed results

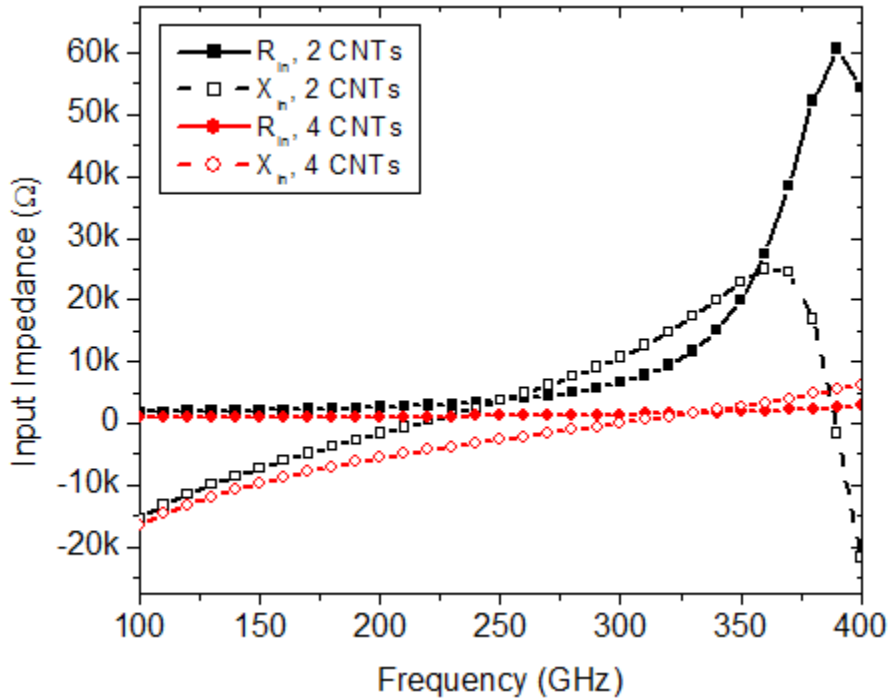


Fig. 5.7 Simulated input impedance of CNT bundle monopoles with (a) two CNTs and (b) four CNTs shown in Fig. 5.3.

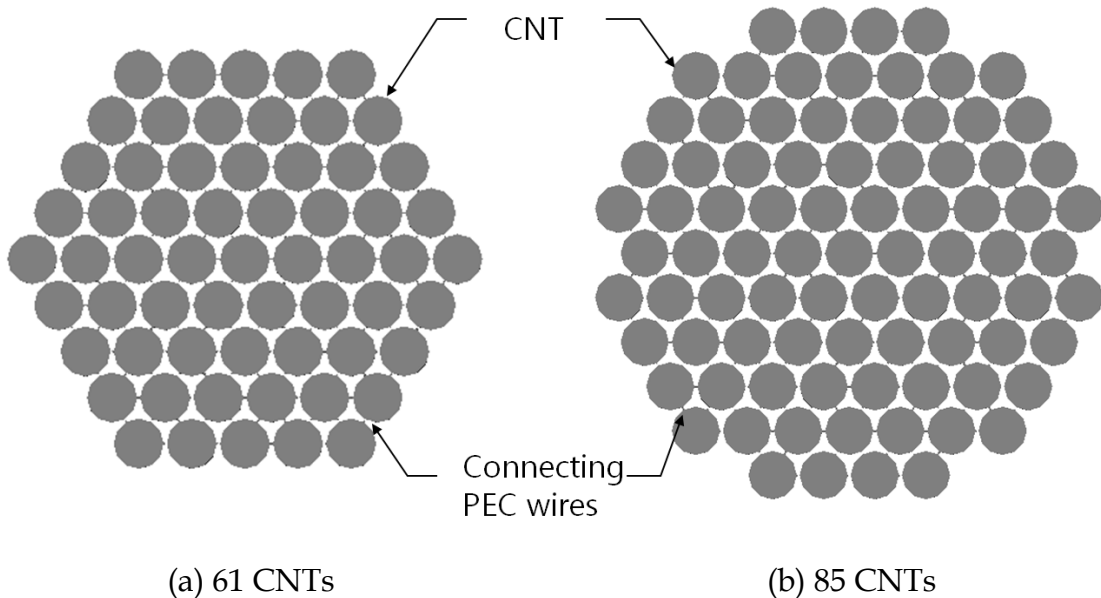


Fig. 5.8 Top view of two CNT bundle monopoles with (a) 61 and (b) 85 CNTs.

for the input resistance, resonant frequency, gain, radiation resistance, and efficiency for the two CNT bundles and the Cu monopole are summarized in Table 5.2. The same performance parameters for a single CNT dipole and monopole are also provided. Several observations can be made:

- The 61- and 85-CNT bundle monopoles are matched as expected;
- The Cu wire monopole is heavily capacitive. The resonant frequency of the Cu wire monopole of 10 μm will be around 15 THz;
- The resonant frequency for the bundle monopoles increases with the number of CNTs in the bundle. Therefore, antenna miniaturization is getting worse as the number of CNT increases;
- The gain and the efficiency for the bundle monopoles are improved significantly compared to the single CNT dipole/monopole although the values are still small;
- The gain and the efficiency for the 85-CNT bundle monopole are higher than those for the Cu wire monopole. The poor performance of the Cu wire monopole

Table 5.2 Performance comparison between CNT dipole, CNT monopoles, and Cu monopole. (* VSWR is with respect to 50 Ω)

	Single CNT dipole (L = 10 μm)	Single CNT monopole (L = 10 μm)	61 CNTs monopole (L = 10 μm)	85 CNTs monopole (L = 10 μm)	Cu Wire Monopole (R = 26.4 nm, L = 10 μm, same as 85 CNTs bundle)
R _{in}	12 kΩ	5.7 kΩ	96 Ω (VSWR = 1.92)*	69 Ω (VSWR = 1.38)*	Z _{in} = 49.4 – j1104 Ω (VSWR = 496)*
f ₀	160 GHz (L = λ ₀ /94)	160 GHz (L = λ ₀ /188)	1042 GHz (L = λ ₀ /29)	1206 GHz (L = λ ₀ /25)	1206 GHz (Not resonant)
Gain (θ = 90°)	-53 dBi	-50 dBi	-15.9 dBi	-12.5 dBi	-14.6 dBi
R _{rad}	0.0288 Ω	0.0195 Ω	0.82 Ω	1.1 Ω	0.56 Ω
Efficiency	0.00033 %	0.00032 %	0.85 %	1.59 %	1.13 %

is caused by mismatch. Note, however, that the CNT bundle monopoles resonate at more than ten times lower frequency than the Cu counterpart.

5.3. Nano Coaxial Lines

As discussed in Chapter 4, at nanoscale the CNT interconnect such as a coaxial line is a viable alternative to its Cu counterpart with respect to loss and impedance, however, both remain high. To reduce their values, a bundle composed of many individual CNTs has been considered by several groups [94, 95]. A CNT bundle comprising the inner conductor of a nano-coaxial transmission line is investigated in this section.

5.3.1. Modeling Validation

To validate baseline FEM modeling for the coaxial line with a CNT bundle, MoM analysis is utilized. A drawing of the coaxial line with the CNT bundle as a center section of the inner conductor is shown in Fig. 5.9. The radius of the inner conductor is 100 nm and the length of the coaxial line is 200 nm. Z_{c_conv} represented by (4.5) is fixed at 50Ω with the air dielectric. Twelve CNTs having the radius of 2.712 nm each and a length of 100 nm are bridging the two separated parts of the solid PEC inner conductor in the figure. Modeling validation is conducted by studying the effect of the number of CNTs on the line performance. A small number of CNTs (1, 4, and 12) are adopted for validation since an increased number of CNTs causes large memory consumption and overall computational cost becomes prohibitive. Simulations with FEM and MoM up to

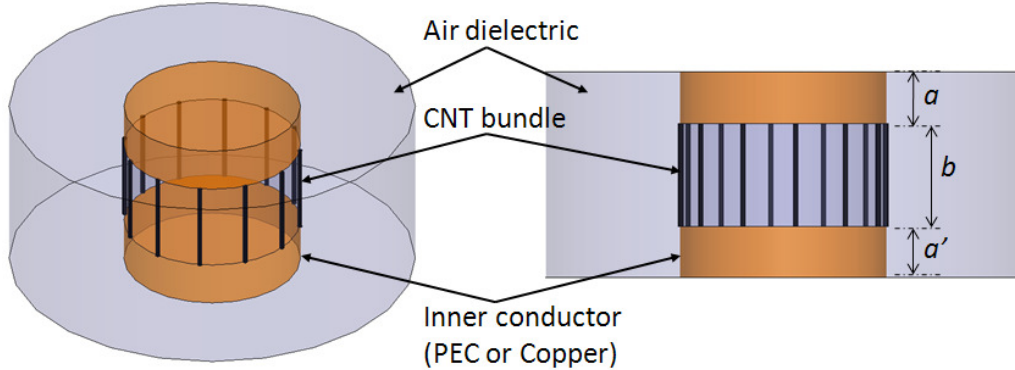


Fig. 5.9 Isometric view (left) and side view (right) of a nano-coaxial line with a CNT bundle as the center section of the inner conductor. Twelve CNTs are used in this setup to connect the two disjoint solid parts.

30 GHz are conducted. Insertion loss (IL) is computed from simulated S-parameters using (4.7) because the characteristic impedance of the coax may not be matched to the reference impedance of 50Ω and large amount of reflection may occur at the input of the line. The IL results from FEM and MoM are compared in Fig. 5.10. As seen, excellent agreement between the two methods is obtained. Also note that, as expected, the IL decreases with increased number of CNTs.

Composite coaxial lines with the Cu/CNTs inner conductor shown in Fig. 5.9 are studied next. Because of the small dimension of Cu, a smaller conductivity ($4 \times 10^7 \text{ S/m}$) than the bulk conductivity is applied [4]. Table 5.3 summarizes IL at 30 GHz for a composite coaxial topology. To compare performance of the composite coaxial line to that of the Cu coax, a 200 nm-long coax with solid Cu inner conductor is simulated, and a loss of 0.0096 dB / 200 nm is obtained. This is much smaller than the loss of the composite geometry with 108 CNTs. One can estimate that over 1000 CNTs are needed to reduce the line loss to about 0.01 dB for this configuration.

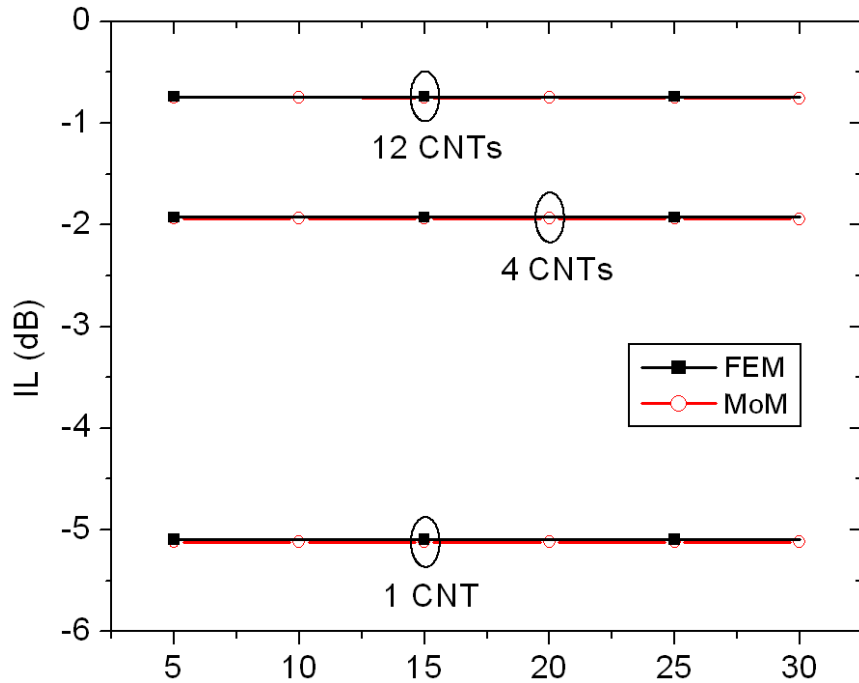


Fig. 5.10 Validation of FEM models for nano-coaxial lines with CNT bundles with different numbers of CNTs. The outer conductor is assumed to be PEC.

Table 5.3 Line loss per 200 nm of the coax with CNT bundle versus the number of CNTs at 30 GHz. The inner conductor attached to the bundle is assumed to be Cu.

Number of CNTs	1	4	12	36	108
IL (dB) / 200 nm	5.14	2.02	0.79	0.28	0.09

5.3.2. Identical Bundle and Mixed Bundle

It is estimated that the composite coaxial line with Cu/CNT bundle inner conductor needs more than 1000 CNTs to give lower loss than the Cu coax. To reduce computational cost, further investigation into the coaxial line with a CNT bundle is conducted with a smaller nano-coaxial line. The radius of the Cu inner conductor is reduced to 26 nm. Thus, the conductivity of the Cu inner conductor is also changed to 2.7×10^7 S/m [4]. If the bundle is densely packed with identical CNTs within the same

radius as the Cu inner conductor, a maximum of 61 CNTs with 2.712 nm radius can be assembled. The distance between neighboring CNTs is fixed at the lattice constant of $2R_{\text{CNT}} + 0.34$ nm, where R_{CNT} is the radius of the CNTs [98]. The entire configuration and arrangement of CNTs are shown in Fig. 5.11. If smaller CNTs with 1.356 nm radius are used, the maximum number of the CNTs in the bundle is 234. The FEM simulations are carried out for the coaxial lines with 61 CNTs with 2.712 nm radius, 234 CNTs with 1.356 nm radius, and with solid Cu inner conductor. Their performances are compared with respect to the characteristic impedance (Z_c), propagation constant ($\gamma = \alpha + j\beta$), IL, and slow-wave factor (F_{sw}) obtained from the computed S-parameters. The results at 30 GHz are summarized in Table 5.4. Note that all parameters for the coaxial lines with CNT bundles correspond to section *b* in Fig. 5.9, i.e. the coax with the CNT bundle only.

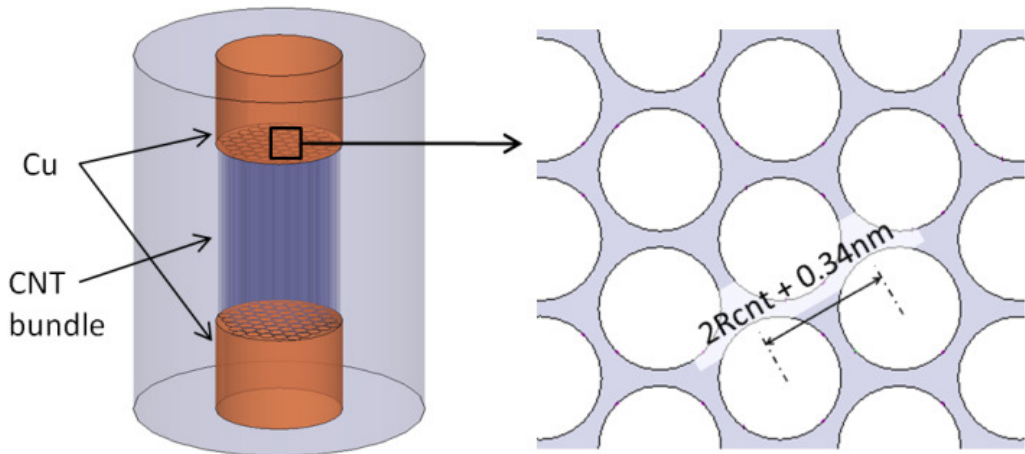


Fig. 5.11 Nano-coaxial line with a CNT bundle and solid Cu as the inner conductor (left), and the arrangement of CNTs in the bundle (right). The bundle is composed of 61 identical CNTs of 2.712 nm radius. The radius of the Cu inner conductor is 26 nm. CNTs are densely packed, therefore 61 CNTs are the maximum within the given cross-section of Cu.

Table 5.4 Performance comparison between the coaxial lines with CNT bundles and solid Cu. The solution frequency is 30 GHz.

Characteristic Parameter	Cu	CNT Bundle	
		61 CNTs (R=2.712 nm)	234 CNTs (R=1.356 nm)
$Z_c (\Omega)$	842-j840	1168-j673	580-j331
$\gamma = \alpha + j\beta$	$10629 + j10654$	$7725+j11376$	$4051+j7103$
F_{sw}	17	21	11
IL (dB) / 100 nm	0.15	0.15	0.04

The characteristic impedance and propagation constant for section b are obtained by the

ABCD matrix calculation similar to (2.1),

$$\begin{aligned} \begin{bmatrix} A & B \\ C & D \end{bmatrix}_{Total} &= \begin{bmatrix} A & B \\ C & D \end{bmatrix}_a \cdot \begin{bmatrix} A & B \\ C & D \end{bmatrix}_b \cdot \begin{bmatrix} A & B \\ C & D \end{bmatrix}_{a'} \\ &= \begin{bmatrix} A & B \\ C & D \end{bmatrix}_a \cdot \begin{bmatrix} \cosh(\gamma l) & Z_0 \sinh(\gamma l) \\ \frac{1}{Z_0} \sinh(\gamma l) & \cosh(\gamma l) \end{bmatrix} \cdot \begin{bmatrix} A & B \\ C & D \end{bmatrix}_{a'}, \end{aligned} \quad (5.1)$$

$$\begin{aligned} \begin{bmatrix} A & B \\ C & D \end{bmatrix}_b &= \begin{bmatrix} \cosh(\gamma l) & Z_0 \sinh(\gamma l) \\ \frac{1}{Z_0} \sinh(\gamma l) & \cosh(\gamma l) \end{bmatrix} \\ &= \begin{bmatrix} A & B \\ C & D \end{bmatrix}_a^{-1} \cdot \begin{bmatrix} A & B \\ C & D \end{bmatrix}_{Total} \cdot \begin{bmatrix} A & B \\ C & D \end{bmatrix}_{a'}^{-1}. \end{aligned} \quad (5.2)$$

Several observations can be made from the table. First, the characteristic impedances of the lines are complex and very high, thus presenting a significant challenge for impedance matching. Second, the speed of a wave along the line with CNT bundles

may be faster or slower than that with conventional metal (Cu, in this case). Finally, the smaller and the more CNTs are used in the bundle, the lower the impedance and line loss become.

Knowing that the metallic CNTs can be separated from an arbitrary CNT bundle that contains metallic and semiconducting CNTs [65-68], one can conceive that a CNT bundle composed of metallic CNTs with larger and smaller radii could be built by manipulation. Fig. 5.12 shows a coaxial line with the bundle composed of mixed CNTs with 2.712 nm and 0.678 nm radii. Separation between neighboring CNTs is 0.69 nm, that is, the bundle is less dense than the two given in Table 5.4. The number of CNTs is 37 for 2.712 nm and 96 for 0.678 nm radius CNTs. Computed results are shown in Table 5.5. For all parameters, the coax with the mixed bundle of two different CNTs has intermediate performance between the two lines shown in Table 5.4. Fig. 5.13 shows

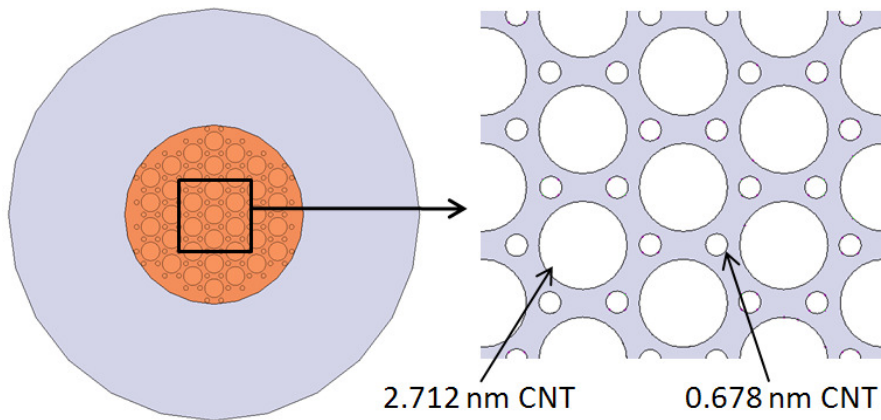


Fig. 5.12 Top view of nano-coaxial line with the CNT bundle and solid Cu as the inner conductor (left), and the arrangement of CNTs in the bundle (right). The bundle is mixed with 37 larger CNTs of 2.712 nm radius and 96 smaller CNTs of 0.687 nm radius. The radius of the Cu inner conductor is 26 nm.

Table 5.5 Performance of the coaxial line with the mixed CNT bundle. The solution frequency is 30 GHz.

Characteristic Parameters	CNT Bundle 37 CNTs (2.712 nm) + 96 CNTs (0.687 nm)
$Z_c (\Omega)$	$789 - j461$
$\gamma = \alpha + j\beta$	$5409 + j9252$
F_{sw}	15
IL (dB) / 100 nm	0.07

cross-sections of the three CNT bundles discussed in Table 5.4 and 5.5. The total surface area of all CNTs in each bundle occupies about 66% (61 CNTs), 64% (234 CNTs), and 47% (37 + 96 CNTs) of the area of the Cu inner conductor. Results indicate that the filling factor of the surface area of CNTs affects the performance of the bundle for identical CNTs consistently. That is, however, not the case for mixed radii CNTs.

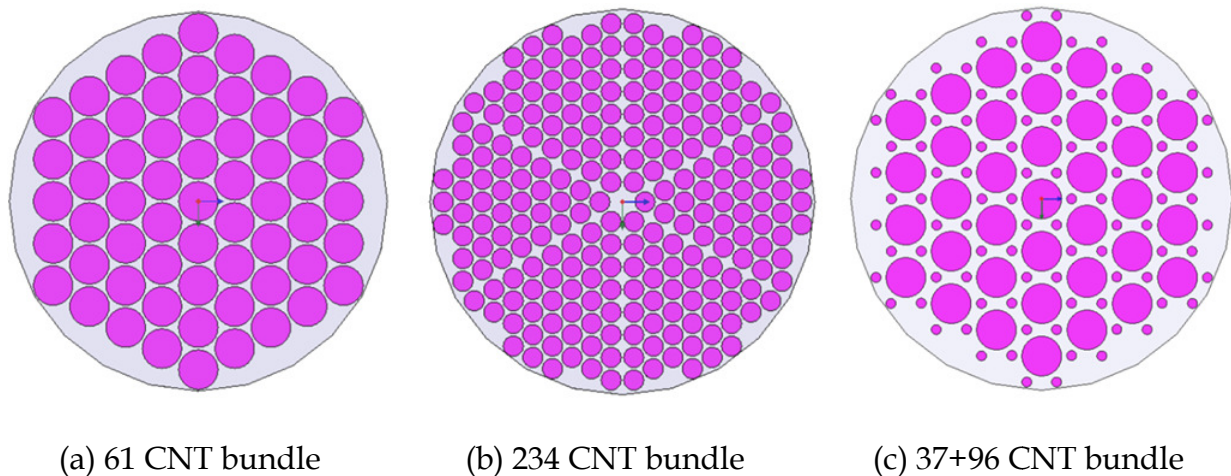


Fig. 5.13 Cross-sections of the three CNT bundles.

5.4. Single Wire Transmission Lines

The bundle of 61 CNTs of 2.712 nm radius forming a Goubau line is simulated with and without a 10 nm-thick Al_2O_3 coating. Fig. 5.14 shows the CNT bundle Goubau line with coating. Performances of the two lines are compared with those of the Cu Goubau line with 26 nm radius and 10 nm-thick Al_2O_3 coating. The characteristic impedance, propagation constant, F_{sw} , and S_{21} are summarized in Table 5.6. The simulated line length is 100 nm. As seen, the CNT bundle Goubau line has less loss than the Cu-based Goubau line. However, the impedance and F_{sw} of the CNT bundle Goubau line are slightly higher.

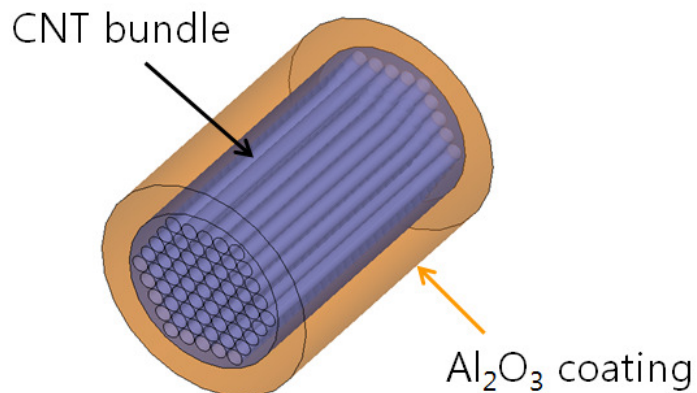


Fig. 5.14 Goubau line with a 61-CNT bundle and 10 nm-thick Al_2O_3 coating.

Table 5.6 Performance comparison between the Cu Goubau line and the CNT bundle Goubau line. The solution frequency is 30 GHz.

Characteristic Parameters	Cu (10 nm-thick Al_2O_3 Coating)	CNT Bundle of 61 CNTs	
		No Coating	10 nm-thick Al_2O_3 Coating
Z_c (k Ω)	2.25 - j2.22	3.08 - j1.78	2.98 - j1.72
$\gamma = \alpha + j\beta$	3984 + j4037	2967 + j5160	3067 + j5335
F_{sw}	6.2	8.2	8.5
S_{21} (dB) / μm	0.04	0.031	0.032

CHAPTER 6

SUMMARY, CONTRIBUTIONS, AND FUTURE WORK

This thesis presents high frequency characterization of individual metallic NWs and CNTs and CNT bundles by modeling and two-port measurements. Summary of each chapter, thesis contributions, and relevant future work are discussed herein.

6.1. Characterization of Platinum Nanowires (I) – Contact Impedance and Conductivity

Comprehensive methodology for simultaneous characterization of the contact resistance and conductivity of individual Pt NWs over broadband frequency range is developed and discussed in Chapter 2. It is shown that on-wafer multiline TRL calibration is suitable for characterization of extreme impedance devices. The finite element and method of moments based full-wave analysis are used to aid the nanometer-scale metrology for the first time. To deepen the understanding of the problem, circuit element models are also developed. Comprehensive full-wave and circuit element modeling is carried out using relevant specially developed devices with known parameters. Then, both models are utilized to determine ranges for contact resistance and conductivity of Pt NWs. It is shown that the single two-port measurement is not sufficient for the complete characterization. In order to separate the

contact resistance from NW's properties, two approaches using transmission line and lumped element-based models for Pt NWs of two different lengths are developed. Both approaches rely on two sets of measurements with NWs having different lengths. It is seen that lumped element-based models provide accurate results for both contact resistance and conductivity. The obtained contact resistance is about 50Ω , and conductivity is about $0.013\sigma_{bulk}$ for 300 nm diameter Pt NWs. It is shown that the transmission line models are more applicable for highly conductive devices with negligible contact resistance.

6.2. Characterization of Platinum Nanowires (II) – Contactless Approach

The metrology of Pt NW devices with capacitive coupling between Pt NWs and a CPW structure is discussed in Chapter 3. The coupling contacts are exploited to eliminate an issue of the contact resistance and to make a problem simpler than the one with direct contacts. Therefore, this method allows the determination of conductivity of associated NWs. Two configurations, in-slot and on-dielectric, are designed, analyzed, validated, and practically realized. The necessity of full-wave modeling is clearly demonstrated and fully utilized for both accurate metrology and sensitivity- based device under test design. Structural investigation of fabricated devices is conducted to determine the methods' accuracy and more importantly their applicability. The full-wave models are fitted to measurements to determine the conductivity of Pt NWs. Obtained value for a 340 nm diameter Pt NW is $0.014\sigma_{bulk}$ which is well correlated with the result found from direct contact methods in Chapter 2. Based on the conducted

elemental analysis, the effective dielectric constant for the dielectric layer is set to be 12 instead 4 as tabulated for SiO_2 . It is shown that contaminants alter the dielectric layer to gallium oxide (Ga_2O_3) from SiO_2 .

6.3. Characterization of Individual Carbon Nanotubes and Applications

In Chapter 4, the full-wave modeling of individual metallic SWCNTs is employed to characterize and evaluate their performance as microwave interconnects. Method of moments and finite element methods with frequency-dependent conductivity that accounts for quantum effects are developed. Comprehensive modeling and validation procedures are established for different methods' formulations and their use for analysis of CNTs. Three interconnect schemes are investigated: wireless interconnects with CNT dipoles, nano-coaxial lines with a CNT inner conductor, and CNT-based single wire lines. For each interconnect, the impedance and signal transmission are computed and compared to those of Cu-based counterparts. It is shown that CNT-based interconnects can have superior performance than Cu-based counterparts. Finally, the performance of all CNT-based interconnects are compared over up to micrometer range communication line. It is found that the single wire CNT interconnect is the best choice for shorter distances, while the wireless interconnect is the best for longer distances.

6.4. Characterization of Carbon Nanotube Bundles and Applications

To overcome fundamentally high loss and impedance of individual CNTs, several microwave interconnect configurations with a bundle of metallic SWCNTs are discussed in Chapter 5. Specifically, CNT bundle monopole antennas, nano-coaxial lines and Goubau lines are characterized. Effects of the separation of CNTs and the number of CNTs in the bundle for monopole antennas are studied. It is found that the smaller separation distance and the larger number of same length CNTs in the bundle increase the resonant frequency. Also, the gain and efficiency of the CNT bundle monopoles are significantly improved by increasing the number of CNTs in the bundle. It is shown that the CNT bundle monopole is well matched to 50Ω with 61-85 CNTs, and has higher gain and efficiency than Cu bulk wire with the same size as 85-CNT bundle. Characteristics of nano-coaxial lines are analyzed with three bundle configurations including a bundle with larger CNTs, a bundle with smaller CNTs, and a bundle with mixed CNTs having smaller and larger diameters. Their performance is compared to a Cu-based coaxial line. It is seen that the CNT based coaxial lines can have lower characteristic impedance and line loss than Cu based coaxial lines, and that the result is reinforced with decreasing the radius of the CNTs and increasing the number of CNTs. Characteristics of the CNT bundles in a Goubau line configuration are also studied and it is found that the CNT bundle Goubau lines can have lower loss and larger slow-wave factor than the Cu-based counterparts.

6.5. Original Contributions

The original contributions of this thesis are :

- Systematic approaches for modeling and measurements of metallic nanowires are developed.
- Feasibility of conventional modeling methods (full-wave and circuit) is demonstrated for modeling, analysis, and design of individual NWs.
- Suitability of conventional on-wafer multiline TRL calibration for RF measurements of nanometer-size devices is demonstrated.
- Three algorithms for extraction of contact resistance and conductivity of individual metallic NWs at high frequencies are developed: fitting method with full-wave and circuit simulations, transmission line-based approach, and lumped element physics-based approach.
- A set of calibration curves for adjusted contact resistance and conductivity of Pt NWs is developed. This may be useful in nanometer-size modeling of individual devices and systems.
- It is shown that the transmission line-based algorithm is useful for low-loss devices, however, it is inapplicable for NWs due to their inherently high loss.
- It is shown that the lumped element physics-based algorithm accurately extracts the contact impedance and conductivity of metallic NWs.
- Two contactless approaches for measurement of NW conductivity are developed: ‘in-slot’ configuration and ‘on-dielectric’ configuration. Obtained results are well correlated with those from the direct contact configurations.

- Several issues having risen from fabrication and their effects on contactless metrology are addressed. Metrology limits, accuracy, sensitivity, etc. and needs for post-fabrication elemental analysis are demonstrated.
- Comprehensive modeling approach for interconnects with individual SWCNTs is established. Wireless interconnects with CNT dipoles, ALD-based coaxial lines with CNT inner conductor, and CNT based Sommerfeld and Goubau lines are studied. Their superior performance compared to Cu-based counterparts is demonstrated. Relevant conclusions regarding their suitability versus range of transmission are made.
- Comprehensive modeling approach for CNT bundle-based interconnects is developed. CNT bundle monopoles, nano-coaxial lines with CNT bundle inner conductor, and CNT bundle-based Sommerfeld and Goubau lines are designed for low loss and 50Ω nominal impedance.

6.6. Future Work

To improve the accuracy of the contactless approach, very thin dielectric (< 10 nm) should be used, as mentioned in Section 3.3. A nm-thick alumina could be fabricated and measured. Also, the investigation of short and long term environmental effects on conductivity and contact resistance is needed. Because of their small size and contaminants, oxidation of nanoscale devices can be an issue that needs serious consideration in the future.

Metrology approaches demonstrated in Chapters 2 and 3 are developed to characterize metallic NWs by the use of modeling and measurements at high frequencies. Specifically, Pt NW's conductivity and relevant contact resistance are determined. It is believed that the developed metrology can be applied to any other metallic NW. Since the future nanoelectronic systems will utilize metallic and semiconducting NWs, the characterization of semiconducting NWs and relevant contact resistance is needed. For the semiconducting NWs, the methodologies from Chapters 2 and 3 may need to be refined, or new methods may have to be developed because material properties of semiconducting NWs depend on bias voltages. Their contact resistances at both ends of the NWs may be different, which is another issue that needs attention in the future. Once metrology for metallic and semiconducting NWs is fully developed, its use can be extended to CNTs which may be either metallic or semiconducting.

CNTs characterized in Chapters 4 and 5 have better electrical performance than conventional metals on the same length scale. However, the CNTs also have intrinsically high impedance ($6.5 \text{ k}\Omega$). Extension of the developed modeling approach to grapheme (the 2010 Nobel Prize in Physics [107]) and its applications as microwave interconnects are of great interest. While a CNT is a 1-D structure, graphene is a 2-D structure so that it may have lower impedance that can be more easily matched to 50Ω [108]. Modeling, design, and analysis of graphene are expected to be more complicated because of its anisotropy, i.e. its conductivity may be in a tensor form [109]. In order to design grapheme-based systems, methodologies for accurate characterization of

graphene need to be developed, and its interconnect applications have to be precisely characterized.

BIBLIOGRAPHY

- [1] C. Durkan, *Current at the Nanoscale: An Introduction to Nanoelectronics*. Imperial College Press, 2007.
- [2] K. Fuchs, "The conductivity of thin metallic films according to the electron theory of metals," *Proceedings of the Cambridge Philosophical Society*, vol. 34, pp. 100-108, 1938.
- [3] R. B. Dingle, "The Electrical Conductivity of Thin Wires," *Royal Society of London Proceedings Series A*, vol. 201, pp. 545-560, May, 1950.
- [4] W. Steinhogl, G. Schindler, G. Steinlesberger, M. Traving and M. Engelhardt, "Comprehensive study of the resistivity of copper wires with lateral dimensions of 100 nm and smaller," *Journal of Applied Physics*, vol. 97, pp. 023706-1-023706-7, 2005.
- [5] F. Leonard and A. A. Talin, "Electrical contacts to nanotubes and nanowires: why size matters," *ArXiv:Cond-mat/0602003v1 [Cond-Mat. Mtrl-Sci]*, pp. 1-6, Jan, 2006.
- [6] G. D. Marzi, D. Iacopino, A. J. Quinn and G. Redmond, "Probing intrinsic transport properties of single metal nanowires: Direct-write contact formation using a focused ion beam," *Journal of Applied Physics*, vol. 96, pp. 3458-3462, 2004.
- [7] M. E. Toimil Molares, E. M. Hohberger, C. Schaefflein, R. H. Blick, R. Neumann and C. Trautmann, "Electrical characterization of electrochemically grown single copper nanowires," *Applied Physics Letters*, vol. 82, pp. 2139-2141, 2003.
- [8] G. W. Hanson, "Fundamental transmitting properties of carbon nanotube antennas," *IEEE Transactions on Antennas and Propagation*, vol. 53, pp. 3426-3435, 2005.
- [9] P. Rice, T. M. Wallis, S. E. Russek and P. Kabos, "Broadband Electrical Characterization of Multiwalled Carbon Nanotubes and Contacts," *Nano Letters*, vol. 7, pp. 1086-1090, 04/01, 2007.

- [10] K. Kim, T. M. Wallis, P. Rice, C. -J. Chiang, A. Imtiaz, P. Kabos and D. S. Filipovic, "A Framework for Broadband Characterization of Individual Nanowires," *IEEE Microwave and Wireless Components Letters*, vol. 20, pp. 178-180, 2010.
- [11] U. Yogeswaran and S. Chen, "A Review on the Electrochemical Sensors and Biosensors Composed of Nanowires as Sensing Material," *Sensors*, vol. 8, pp. 290-313, 2008.
- [12] S. Fiedler, M. Zwanzig, R. Schmidt and W. Scheel, "Ch. 20 nanowires in electronics packaging," in *Nanopackaging: Nanotechnologies and Electronics Packaging*, J. E. Morris, Ed. Springer US, 2009, .
- [13] A. R. Rathmell, S. M. Bergin, Y. -. Hua, Z. Li and B. J. Wiley, "The Growth Mechanism of Copper Nanowires and Their Properties in Flexible, Transparent Conducting Films," *Adv Mater*, vol. 22, pp. 3558-3563, 2010.
- [14] S. Koo, M. D. Edelstein, Q. Li, C. A. Richter and E. M. Vogel, "Silicon nanowires as enhancement-mode Schottky barrier field-effect transistors," *Nanotechnology*, vol. 16, pp. 1482-1485(4), Sep., 2005.
- [15] R. R. Llinas, K. D. Walton, M. Nakao, I. Hunter and P. A. Anquetil, "Neuro-vascular central nervous recording/stimulating system: Using nanotechnology probes," *Journal of Nanoparticle Research*, vol. 7, pp. 111-127, 2005.
- [16] A. I. Hochbaum, R. Chen, R. D. Delgado, W. Liang, E. C. Garnett, M. Najarian, A. Majumdar and P. Yang, "Enhanced thermoelectric performance of rough silicon nanowires," *Nature*, vol. 451, pp. 163-167, 01/10, 2008.
- [17] J. J. Boland, "Flexible electronics: Within touch of artificial skin," *Nat Mater*, vol. 9, pp. 790-792, 2010.
- [18] A. F. Mayadas and M. Shatzkes, "Electrical-Resistivity Model for Polycrystalline Films: the Case of Arbitrary Reflection at External Surfaces," *Phys.Rev.B*, vol. 1, pp. 1382-1389, Feb, 1970.
- [19] J. Lin, J. P. Bird, L. Rotkina and P. A. Bennett, "Classical and quantum transport in focused-ion-beam-deposited Pt nanointerconnects," *Applied Physics Letters*, vol. 82, pp. 802-804, 2003.

- [20] L. Penate-Quesada, J. Mitra and P. Dawson, "Non-linear electronic transport in Pt nanowires deposited by focused ion beam," *Nanotechnology*, vol. 18, pp. 215203-1-215203-5, 2007.
- [21] P. A. Smith, C. D. Nordquist, T. N. Jackson, T. S. Mayer, B. R. Martin, J. Mbindyo and T. E. Mallouk, "Electric-field assisted assembly and alignment of metallic nanowires," *Applied Physics Letters*, vol. 77, pp. 1399-1401, 2000.
- [22] T. Schwamb, B. R. Burg, N. C. Schirmer and D. Poulikakos, "On the effect of the electrical contact resistance in nanodevices," *Applied Physics Letters*, vol. 92, pp. 243106-1-243106-3, 2008.
- [23] J. J. Plombon, K. P. OBrien, F. Gstrein, V. M. Dubin and Y. Jiao, "High-frequency electrical properties of individual and bundled carbon nanotubes," *Applied Physics Letters*, vol. 90, pp. 063106-063106-3, 2007.
- [24] S. C. Jun, X. M. H. Huang, S. Moon, H. J. Kim, J. Hone, Y. W. Jin and J. M. Kim, "Passive electrical properties of multi-walled carbon nanotubes up to 0.1 THz," *New Journal of Physics*, vol. 9, pp. 265-1-265-9, 2007.
- [25] M. G. Kang, J. H. Lim, S. H. Hong, D. J. Lee, S. W. Hwang, D. Whang, J. S. Hwang and D. Ahn, "Microwave Characterization of a Single Wall Carbon Nanotube Bundle," *Japanese Journal of Applied Physics*, vol. 47, pp. 4965-4968, 2008.
- [26] S. Iijima, "Helical microtubules of graphitic carbon," *Nature*, vol. 354, pp. 56-58, 11/07, 1991.
- [27] M. C. Hersam, "Progress towards monodisperse single-walled carbon nanotubes," *Nat Nano*, vol. 3, pp. 387-394, 2008.
- [28] S. Sawada and N. Hamada, "Energetics of carbon nano-tubes," *Solid State Commun.*, vol. 83, pp. 917-919, 9, 1992.
- [29] L. Qin, X. Zhao, K. Hirahara, Y. Miyamoto, Y. Ando and S. Iijima, "Materials science: The smallest carbon nanotube," *Nature*, vol. 408, pp. 50-50, 11/02, 2000.
- [30] R. Scipioni, "Is the smallest carbon nanotube (2,2) a metal or a semiconductor?" *Physica Status Solidi (b)*, vol. 244, pp. 3137-3142, 2007.

- [31] X. Wang, Q. Li, J. Xie, Z. Jin, J. Wang, Y. Li, K. Jiang and S. Fan, "Fabrication of Ultralong and Electrically Uniform Single-Walled Carbon Nanotubes on Clean Substrates," *Nano Letters*, vol. 9, pp. 3137-3141, 2009.
- [32] A. Javey, P. Qi, Q. Wang and H. Dai, "Ten- to 50-nm-long quasi-ballistic carbon nanotube devices obtained without complex lithography," *Proceedings of the National Academy of Sciences of the United States of America*, vol. 101, pp. 13408-13410, Sep., 2004.
- [33] P. L. McEuen, M. S. Fuhrer and Hongkun Park, "Single-walled carbon nanotube electronics," *Nanotechnology, IEEE Transactions on*, vol. 1, pp. 78-85, 2002.
- [34] M. Dragoman, H. L. Hartnagel, J. Tuovinen and R. Plana, "Microwave applications of carbon nanotubes," *Frequenz*, vol. 59, pp. 251-263, 2005.
- [35] G. Y. Slepyan, S. A. Maksimenko, A. Lakhtakia, O. Yevtushenko and A. V. Gusakov, "Electrodynamics of carbon nanotubes: Dynamic conductivity, impedance boundary conditions, and surface wave propagation," *Phys.Rev.B*, vol. 60, pp. 17136-17149, Dec., 1999.
- [36] T. W. Ebbesen, H. J. Lezec, H. Hiura, J. W. Bennett, H. F. Ghaemi and T. Thio, "Electrical conductivity of individual carbon nanotubes," *Nature*, vol. 382, pp. 54-56, 07/04, 1996.
- [37] H. Dai, E. W. Wong and C. M. Lieber, "Probing Electrical Transport in Nanomaterials: Conductivity of Individual Carbon Nanotubes," *Science*, vol. 272, pp. 523-526, Apr., 1996.
- [38] C. Gomez-Navarro, P. J. D. Pablo, J. Gomez-Herrero, B. Biel, F. Garcia-Vidal, A. Rubio and F. Flores, "Tuning the conductance of single-walled carbon nanotubes by ion irradiation in the Anderson localization regime," *Nat Mater*, vol. 4, pp. 534-539, 2005.
- [39] C. Lan, P. Srisungsitthisunti, P. B. Amama, T. S. Fisher, X. Xu and R. G. Reifenberger, "Measurement of metal/carbon nanotube contact resistance by adjusting contact length using laser ablation," *Nanotechnology*, vol. 19, pp. 125703, 2008.

- [40] S. C. Lim, J. H. Jang, D. J. Bae, G. H. Han, S. Lee, I. Yeo and Y. H. Lee, "Contact resistance between metal and carbon nanotube interconnects: Effect of work function and wettability," *Applied Physics Letters*, vol. 95, pp. 264103-264103-3, 2009.
- [41] L. Nougaret, G. Dambrine, S. Lepilliet, H. Happy, N. Chimot, V. Derycke and J. Bourgoin, "Gigahertz characterization of a single carbon nanotube," *Applied Physics Letters*, vol. 96, pp. 042109-042109-3, 2010.
- [42] W. Kim, A. Javey, R. Tu, J. Cao, Q. Wang and H. Dai, "Electrical contacts to carbon nanotubes down to 1 nm in diameter," *Appl. Phys. Lett.*, vol. 87, pp. 173101, 2005.
- [43] A. Bachtold, M. S. Fuhrer, S. Plyasunov, M. Forero, E. H. Anderson, A. Zettl and P. L. McEuen, "Scanned Probe Microscopy of Electronic Transport in Carbon Nanotubes," *Phys. Rev. Lett.*, vol. 84, pp. 6082-6085, Jun., 2000.
- [44] S. Salahuddin, M. Lundstrom and S. Datta, "Transport effects on signal propagation in quantum wires," *IEEE Transactions on Electron Devices*, vol. 52, pp. 1734-1742, 2005.
- [45] M. Zhang, X. Huo, P. C. H. Chan, Q. Liang and Z. K. Tang, "Radio-frequency characterization for the single-walled carbon nanotubes," *Applied Physics Letters*, vol. 88, pp. 163109-163109-3, 2006.
- [46] L. Gomez-Rojas, S. Bhattacharyya, E. Mendoza, D. C. Cox, J. M. Rosolen and S. R. P. Silva, "RF Response of Single-Walled Carbon Nanotubes," *Nano Letters*, vol. 7, pp. 2672-2675, 2007.
- [47] S. C. Jun, J. H. Choi, S. N. Cha, C. W. Baik, S. Lee, H. J. Kim, J. Hone and J. M. Kim, "Radio-frequency transmission characteristics of a multi-walled carbon nanotube," *Nanotechnology*, vol. 18, pp. 255701, 2007.
- [48] G. F. Close and H. P. Wong, "Fabrication and characterization of carbon nanotube interconnects," in *Electron Devices Meeting, 2007. IEDM 2007. IEEE International*, 2007, pp. 203-206.
- [49] A. Tselev, M. Woodson, C. Qian and J. Liu, "Microwave Impedance Spectroscopy of Dense Carbon Nanotube Bundles," *Nano Letters*, vol. 8, pp. 152-156, Jan., 2008.

- [50] G. S. Duesberg, I. Loa, M. Burghard, K. Syassen and S. Roth, "Polarized Raman Spectroscopy on Isolated Single-Wall Carbon Nanotubes," *Phys. Rev. Lett.*, vol. 85, pp. 5436-5439, Dec., 2000.
- [51] A. Jorio, A. G. Souza Filho, V. W. Brar, A. K. Swan, M. S. \Unl\ u, B. B. Goldberg, A. Righi, J. H. Hafner, C. M. Lieber, R. Saito, G. Dresselhaus and M. S. Dresselhaus, "Polarized resonant Raman study of isolated single-wall carbon nanotubes: Symmetry selection rules, dipolar and multipolar antenna effects," *Phys. Rev. B*, vol. 65, pp. 121402, Mar, 2002.
- [52] Y. Wang, K. Kempa, B. Kimball, J. B. Carlson, G. Benham, W. Z. Li, T. Kempa, J. Rybczynski, A. Herczynski and Z. F. Ren, "Receiving and transmitting light-like radio waves: Antenna effect in arrays of aligned carbon nanotubes," *Appl. Phys. Lett.*, vol. 85, pp. 2607-2609, 2004.
- [53] P. J. Burke, S. Li and Z. Yu, "Quantitative Theory of Nanowire and Nanotube Antenna Performance," *IEEE Transactions on Nanotechnology*, vol. 5, pp. 314-334, Jul., 2006.
- [54] J. Hao and G. W. Hanson, "Electromagnetic scattering from finite-length metallic carbon nanotubes in the lower IR bands," *Phys. Rev. B*, vol. 74, pp. 035119, Jul., 2006.
- [55] Y. Wang, Q. Wu, W. Shi, X. He, X. Sun and T. Gui, "Radiation Properties of Carbon Nanotubes Antenna at Terahertz/Infrared Range," *Int J Infrared Millim Waves*, vol. 29, pp. 35-42, 2008.
- [56] Y. Huang, W. Yin and Q. H. Liu, "Performance Prediction of Carbon Nanotube Bundle Dipole Antennas," *IEEE Transactions on Nanotechnology*, vol. 7, pp. 331-337, 2008.
- [57] P. Avouris, J. Appenzeller, R. Martel and S. J. Wind, "Carbon nanotube electronics," *Proceedings of the IEEE*, vol. 91, pp. 1772-1784, 2003.
- [58] M. A. El Sabbagh, S. M. El-Ghazaly and H. A. Naseem, "Carbon nanotube-based planar transmission lines," in *Microwave Symposium Digest, 2009. MTT '09. IEEE MTT-S International*, pp. 353-356, 2009.

- [59] C. Xiang, Y. Pan, X. Liu, X. Sun, X. Shi and J. Guo, "Microwave attenuation of multiwalled carbon nanotube-fused silica composites," *Applied Physics Letters*, vol. 87, pp. 123103-123103-3, 2005.
- [60] H. Xu, S. M. Anlage, L. Hu and G. Gruner, "Microwave shielding of transparent and conducting single-walled carbon nanotube films," *Appl. Phys. Lett.*, vol. 90, pp. 183119, 2007.
- [61] S. J. Kang, C. Kocabas, T. Ozel, M. Shim, N. Pimparkar, M. A. Alam, S. V. Rotkin and J. A. Rogers, "High-performance electronics using dense, perfectly aligned arrays of single-walled carbon nanotubes," *Nat Nano*, vol. 2, pp. 230-236, 2007.
- [62] K. Jensen, J. Weldon, H. Garcia and A. Zettl, "Nanotube Radio," *Nano Letters*, vol. 7, pp. 3508-3511, 2007.
- [63] Z. Shi, Y. Lian, X. Zhou, Z. Gu, Y. Zhang, S. Iijima, L. Zhou, K. T. Yue and S. Zhang, "Mass-production of single-wall carbon nanotubes by arc discharge method," *Carbon*, vol. 37, pp. 1449-1453, 1999.
- [64] Y. Ando, X. Zhao, K. Hirahara, K. Suenaga, S. Bandow and S. Iijima, "Mass production of single-wall carbon nanotubes by the arc plasma jet method," *Chemical Physics Letters*, vol. 323, pp. 580-585, 2000.
- [65] R. Krupke, F. Hennrich, H. Lohneysen and M. M. Kappes, "Separation of Metallic from Semiconducting Single-Walled Carbon Nanotubes," *Science*, vol. 301, pp. 344-347, Jul., 2003.
- [66] Z. Shen, S. Liu, S. Hou, Z. Gu and Z. Xue, "In situ splitting of carbon nanotube bundles with atomic force microscopy," *J. Phys. D*, vol. 36, pp. 2050-2053, 2003.
- [67] S. R. Lustig, A. Jagota, C. Khripin and M. Zheng, "Theory of Structure-Based Carbon Nanotube Separations by Ion-Exchange Chromatography of DNA/CNT Hybrids," *The Journal of Physical Chemistry B*, vol. 109, pp. 2559-2566, 2005.
- [68] N. Peng, Q. Zhang, J. Li and N. Liu, "Influences of ac electric field on the spatial distribution of carbon nanotubes formed between electrodes," *J. Appl. Phys.*, vol. 100, pp. 024309-1-024309-5, 2006.

- [69] A. R. Harutyunyan, G. Chen, T. M. Paronyan, E. M. Pigos, O. A. Kuznetsov, K. Hewaparakrama, S. M. Kim, D. Zakharov, E. A. Stach and G. U. Sumanasekera, "Preferential Growth of Single-Walled Carbon Nanotubes with Metallic Conductivity," *Science*, vol. 326, pp. 116-120, Oct., 2009.
- [70] ANSYS. HFSS: 3D full-wave electromagnetic field simulation. Available: <http://www.ansoft.com/>.
- [71] AWR. AWR microwave office: RF/microwave design software. Available: <http://web.awrcorp.com/>.
- [72] R. B. Marks, "A multiline method of network analyzer calibration," *IEEE Transactions on Microwave Theory and Techniques*, vol. 39, pp. 1205-1215, 1991.
- [73] P. Kabos, H. C. Reader, U. Arz and D. F. Williams, "Calibrated waveform measurement with high-impedance probes," *IEEE Transactions on Microwave Theory and Techniques*, vol. 51, pp. 530-535, 2003.
- [74] D. M. Pozar, *Microwave Engineering (3rd Edition)*. John Wiley & Sons, 2005.
- [75] Anonymous NISTcal. Available: <http://www.nist.gov/eeel/electromagnetics/related-software.cfm>.
- [76] ANSYS. Ansoft designer. Available: <http://www.ansoft.com/>.
- [77] C. A. Balanis, *Antenna Theory - Analysis and Design (3rd Edition)*. John Wiley & Sons, 2005.
- [78] D. K. Cheng, *Field and Wave Electromagnetics (2nd Edition)*. Addison-Wesley, 1989.
- [79] R. E. Matick, *Transmission Lines and Communication Networks: An Introduction to Transmission Lines, High-Frequency and High-Speed Pulse Characteristics and Applications*. IEEE Press, 1995.
- [80] K. Kim, T. M. Wallis, P. Rice, C. J. Chiang, A. Imtiaz, P. Kabos and D. S. Filipovic, "Modeling and metrology of metallic nanowires with application to microwave interconnects," in *2010 IEEE MTT-S International Microwave Symposium Digest (MTT)*, pp. 1292-1295, 2010.

- [81] C. Highstrete, M. Lee, A. A. Talin and A. L. Vance, "Microwave conductance spectra of single-walled carbon nanotube arrays," *Applied Physics Letters*, vol. 95, pp. 203111-203111-3, 2009.
- [82] S. J. Pearton, J. C. Zolper, R. J. Shul and F. Ren, "GaN: Processing, defects, and devices," *Journal of Applied Physics*, vol. 86, pp. 1-78, 1999.
- [83] T. Campbell, R. K. Kalia, A. Nakano, P. Vashishta, S. Ogata and S. Rodgers, "Dynamics of Oxidation of Aluminum Nanoclusters using Variable Charge Molecular-Dynamics Simulations on Parallel Computers," *Phys. Rev. Lett.*, vol. 82, pp. 4866-4869, Jun., 1999.
- [84] K. Banerjee and N. Srivastava, "Are carbon nanotubes the future of VLSI interconnections," in *In Proceedings of the 43 Rd Annual Conference on Design Automation (DAC'06*, pp. 809-814, 2006.
- [85] M. J. Hagmann, "Isolated carbon nanotubes as high-impedance transmission lines for microwave through terahertz frequencies," *IEEE Transactions on Nanotechnology*, vol. 4, pp. 289-296, 2005.
- [86] S. M. George, A. W. Ott and J. W. Klaus, "Surface Chemistry for Atomic Layer Growth," *J. Phys. Chem.*, vol. 100, pp. 13121-13131, 1996.
- [87] C. F. Herrmann, F. H. Fabreguette, D. S. Finch, R. Geiss and S. M. George, "Multilayer and functional coatings on carbon nanotubes using atomic layer deposition," *Applied Physics Letters*, vol. 87, pp. 123110-1-123110-3, 2005.
- [88] G. Goubau, "Surface Waves and Their Application to Transmission Lines," *J. Appl. Phys.*, vol. 21, pp. 1119-1128, 1950.
- [89] EM Software & Systems (USA) Inc. FEKO electromagnetics simulator. Available: <http://www.feko.info/>.
- [90] J. Hao and G. W. Hanson, "Infrared and Optical Properties of Carbon Nanotube Dipole Antennas," *IEEE Transactions on Nanotechnology*, vol. 5, pp. 766-775, 2006.
- [91] S. Trabelsi, A. W. Kraszewski and S. O. Nelson, "Microwave dielectric sensing of bulk density of granular materials," *Measurement Science and Technology*, vol. 12, pp. 2192-2197, 2001.

- [92] M. Wachter, M. Nagel and H. Kurz, "Frequency-dependent characterization of THz Sommerfeld wave propagation on single-wires," *Opt.Express*, vol. 13, pp. 10815-10822, 2005.
- [93] K. Kim and D. S. Filipovic, "Electromagnetic modeling of carbon nanotube interconnects," in *Antennas and Propagation Society International Symposium, 2007 IEEE*, pp. 4336-4339, 2007.
- [94] N. Srivastava and K. Banerjee, "Performance analysis of carbon nanotube interconnects for VLSI applications," in *Computer-Aided Design, 2005. ICCAD-2005. IEEE/ACM International Conference on*, pp. 383-390, 2005.
- [95] Y. Awano, "Carbon nanotube technologies for LSI via interconnects," *IEICE Trans. Electron.*, vol. E89-C, pp. 1499-1503, 2006.
- [96] M. Nihei, A. Kawabata, D. Kondo, M. Horibe, S. Sato and Y. Awano, "Electrical properties of carbon nanotube bundles for future via interconnects," *Jpn. J. Appl. Phys.*, vol. 44, pp. 1626-1628, 2005.
- [97] G. Miano and F. Villone, "An Integral Formulation for the Electrodynamics of Metallic Carbon Nanotubes Based on a Fluid Model," *IEEE Transactions on Antennas and Propagation*, vol. 54, pp. 2713-2724, 2006.
- [98] A. Thess, R. Lee, P. Nikolaev, H. Dai, P. Petit, J. Robert, C. Xu, Y. H. Lee, S. G. Kim, A. G. Rinzler, D. T. Colbert, G. E. Scuseria, D. Tomanek, J. E. Fischer and R. E. Smalley, "Crystalline Ropes of Metallic Carbon Nanotubes," *Science*, vol. 273, pp. 483-487, Jul., 1996.
- [99] M. S. Dresselhaus, G. Dresselhaus and P. Avouris, *Carbon Nanotubes: Synthesis, Structure, Properties, and Applications*. Berlin; New York: Springer, 2001.
- [100] A. Naeemi, R. Sarvari and J. D. Meindl, "Performance comparison between carbon nanotube and copper interconnects for GSI," in *Electron Devices Meeting, 2004. IEDM Technical Digest. IEEE International*, pp. 699-702, 2004.
- [101] A. Nieuwoudt and Y. Massoud, "Evaluating the impact of resistance in carbon nanotube bundles for VLSI interconnect using diameter-dependent modeling techniques," *IEEE Transactions on Electron Devices*, vol. 53, pp. 2460-2466, 2006.

- [102] C. W. Tan and Jianmin Miao, "Modeling of carbon nanotube vertical interconnects as transmission lines," in *Emerging Technologies - Nanoelectronics, 2006 IEEE Conference on*, pp. 75-78, 2006.
- [103] M. S. Sarto and A. Tamburrano, "Electromagnetic analysis of radio-frequency signal propagation along SWCN bundles," in *Nanotechnology, 2006. IEEE-NANO 2006. Sixth IEEE Conference on*, pp. 201-204, 2006.
- [104] M. S. Sarto and A. Tamburrano, "Multiconductor transmission line modeling of SWCNT bundles in common-mode excitation," in *Electromagnetic Compatibility, 2006. EMC 2006. 2006 IEEE International Symposium on*, pp. 466-471, 2006.
- [105] M. V. Shuba, S. A. Maksimenko and A. Lakhtakia, "Electromagnetic wave propagation in an almost circular bundle of closely packed metallic carbon nanotubes," *Phys.Rev.B*, vol. 76, pp. 155407-1-155407-9, Oct., 2007.
- [106] M. S. Sarto, A. Tamburrano and M. D'Amore, "New Electron-Waveguide-Based Modeling for Carbon Nanotube Interconnects," *IEEE Transactions on Nanotechnology*, vol. 8, pp. 214-225, 2009.
- [107] F. All. (2010, 10 Oct.). The 2010 nobel prize in physics - press release. Available: http://nobelprize.org/nobel_prizes/physics/laureates/2010/press.html.
- [108] G. Deligeorgis, M. Dragoman, D. Neculoiu, D. Dragoman, G. Konstantinidis, A. Cismaru and R. Plana, "Microwave propagation in graphene," *Applied Physics Letters*, vol. 95, pp. 073107-073107-3, 2009.
- [109] S. S. V Meera and Girish, "Conductivity tensor of graphene through reflection of microwave measurements," *J. Phys. D*, vol. 42, pp. 055403, 2009.

APPENDIX A

ADDITIONAL MODELING VALIDATIONS

This appendix outlines additional modeling validations not shown in the main part of the thesis. These are important to further demonstrate the validity of the results and conclusions presented herein.

A.1 ABCD Matrix Calculation

An ABCD matrix is often used for analysis of cascaded two-port networks. The conversion from S-parameters is straightforward thus further aiding its utility. The ABCD matrix is also useful to analyze a system whose ports are difficult to directly establish explicitly, e.g. a wire bundle. Once the ABCD matrices for the whole system and some sections of the system are obtained, an ABCD matrix for the other section can be characterized using (5.1). Here, for example, the characteristic impedance and propagation constant for a CPW line with a Pt NW signal line are analyzed. Two known CPW lines can be attached to both ends of the CPW line, as shown in Fig. A.1. Sections *a* and *a'* are CPW lines with a PEC signal line, and they are identical, while section *b* is a CPW line with Pt NW signal line. The conductivity of the Pt NW is assumed to be that

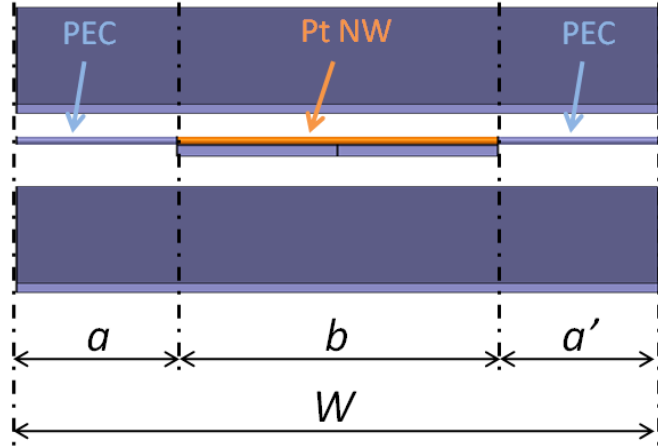


Fig. A.1 CPW line with Pt NW and PEC wire as its signal line. Characteristic impedance and propagation constant of the section b can be obtained from the S-parameters of a , a' , and W using ABCD matrix calculation.

of the bulk Pt (9.3×10^6 S/m). The ABCD matrix for the section b , $\begin{bmatrix} A & B \\ C & D \end{bmatrix}_b = \begin{bmatrix} A_b & B_b \\ C_b & D_b \end{bmatrix}$, is represented as,

$$\begin{aligned} \begin{bmatrix} A & B \\ C & D \end{bmatrix}_b &= \begin{bmatrix} \cosh(\gamma l) & Z_0 \sinh(\gamma l) \\ \frac{1}{Z_0} \sinh(\gamma l) & \cosh(\gamma l) \end{bmatrix} \\ &= \begin{bmatrix} A & B \\ C & D \end{bmatrix}_a^{-1} \cdot \begin{bmatrix} A & B \\ C & D \end{bmatrix}_W \cdot \begin{bmatrix} A & B \\ C & D \end{bmatrix}_{a'}^{-1}, \end{aligned} \quad (\text{A.1})$$

where $\begin{bmatrix} A & B \\ C & D \end{bmatrix}_a$ is the ABCD matrix for the section a , and $\begin{bmatrix} A & B \\ C & D \end{bmatrix}_W$ is the ABCD matrix for the whole structure. From (A.1), the characteristic impedance, Z_c , and propagation constant, γ for the section b can be obtained as follows,

$$Z_c = \sqrt{\frac{B_b}{C_b}}, \quad (\text{A.2})$$

$$\gamma = \frac{1}{l} \ln \left(A_b \pm \sqrt{A_b^2 - 1} \right). \quad (\text{A.3})$$

This simple example can be solved by the ABCD matrix calculation described above and direct FEM modeling. Solutions for Z_c and γ obtained using both approaches are compared in Fig. A.2, showing good agreement between the two. Therefore, ABCD matrix based calculations are applicable for the types of lines and problems of interest for this thesis.

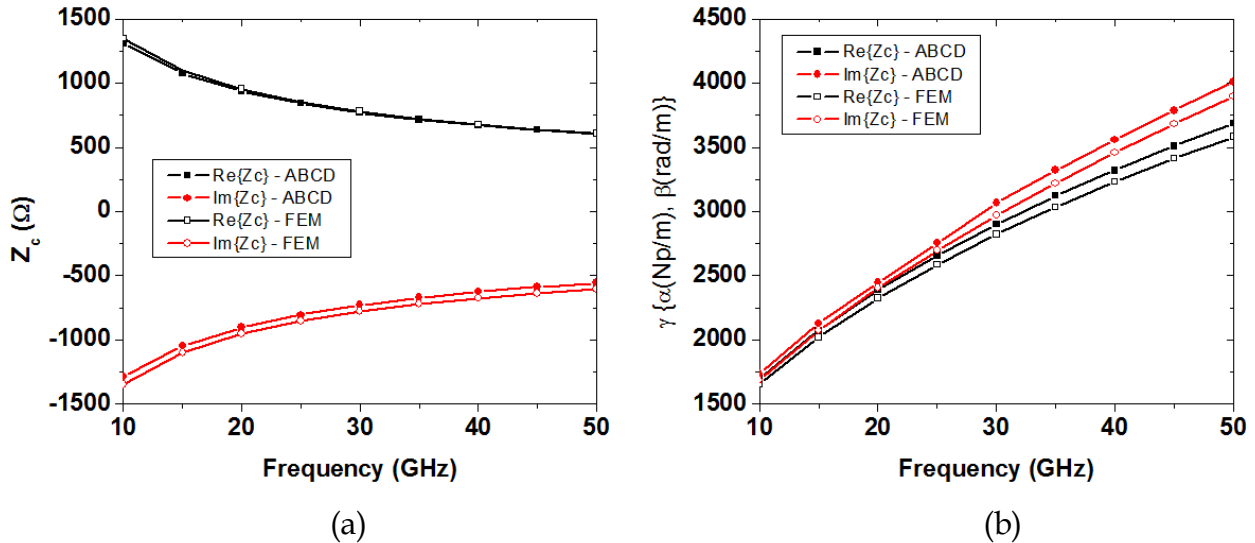


Fig. A.2 Comparison between results from ABCD matrix calculation (ABCD in the legend) and direct FEM modeling (FEM in the legend). (a) characteristic impedance, Z_c and (b) propagation constant, γ .

A.2 Method of Moments Modeling

MoM modeling implemented in AWR and used in Section 2.2.2 has an issue that the narrower end of a tapered CPW cannot be excited directly. That is, an auxiliary CPW line of a certain length needs to be added in order for a wave to propagate. To determine an appropriate excitation structure, five different geometries are examined, as shown in Fig. A.3. Their feed lines are: (a) a 25 μm -long narrow line at port 2, (b) a 325 μm -long narrow line at the port 2, (c) a 25 μm -long wide line at port 1 and narrow line at port 2, (d) a 25 μm -long wide line at port 2, and (e) 25 μm -long wide lines at both ports. To evaluate the five geometries, a CPW structure including two back-to-back tapered CPW lines is introduced as a reference shown in Fig. A.4. A length of the tapered CPW line is 75 μm . The 50 Ω ordinary CPW line has a 50 μm width and 150 μm length for the signal line and 5 μm slot width. Each of above described five

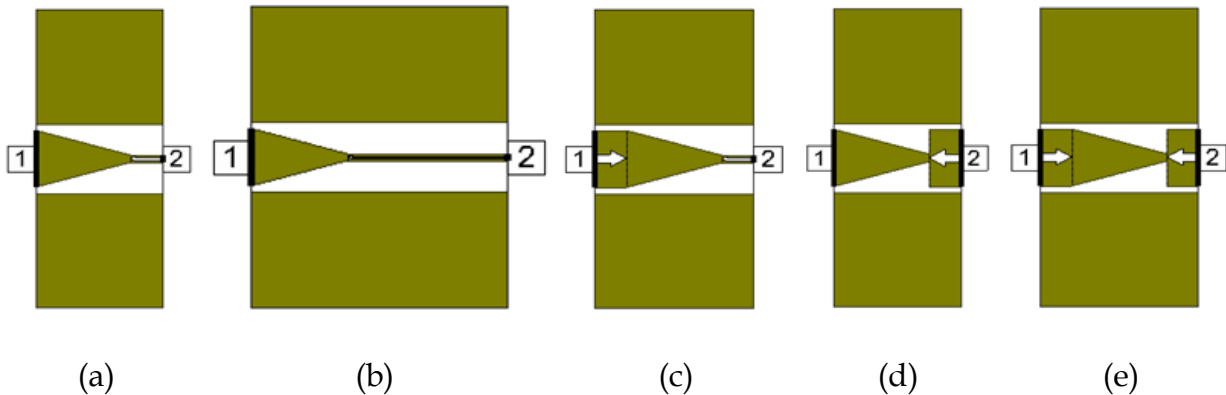


Fig. A.3 Five geometries evaluated for modeling of a tapered CPW. (a) model #1 with a 25 μm line at port 2, (b) model #2 with a 325 μm line at port 2, (c) model #3 with a 25 μm line at both ports, (d) model #4 with a 25 μm line at port 2, and (e) model #5 with a 25 μm line at both ports. A line width is the same as the width of either end of the taper.

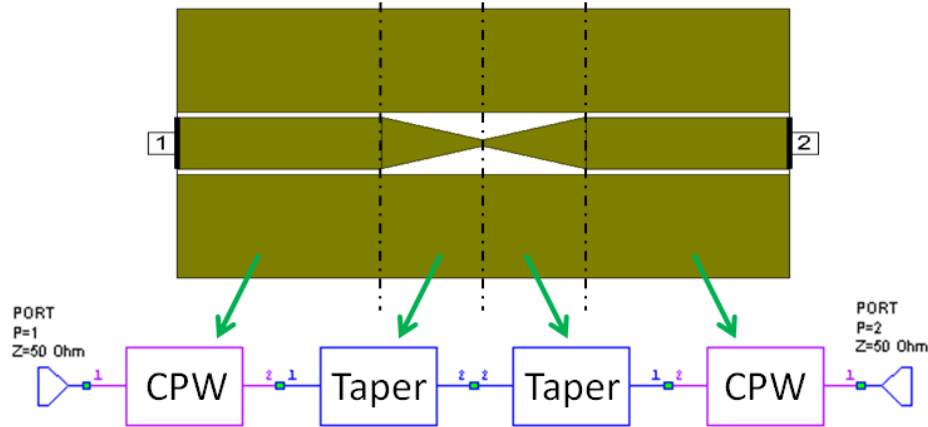


Fig. A.4 CPW structure with two back-to-back tapered CPW lines.

geometries, then, replaces the back-to-back tapered CPW lines to conduct the comparison with the reference. Simulated S-parameters for all cases are compared in Fig. A.5. As seen, although all models slightly differ from the reference structure, the model #2 (Fig. A.3 (b)) shows the best agreement in terms of performance. Therefore, the model #2 is used in Section 2.2.2.

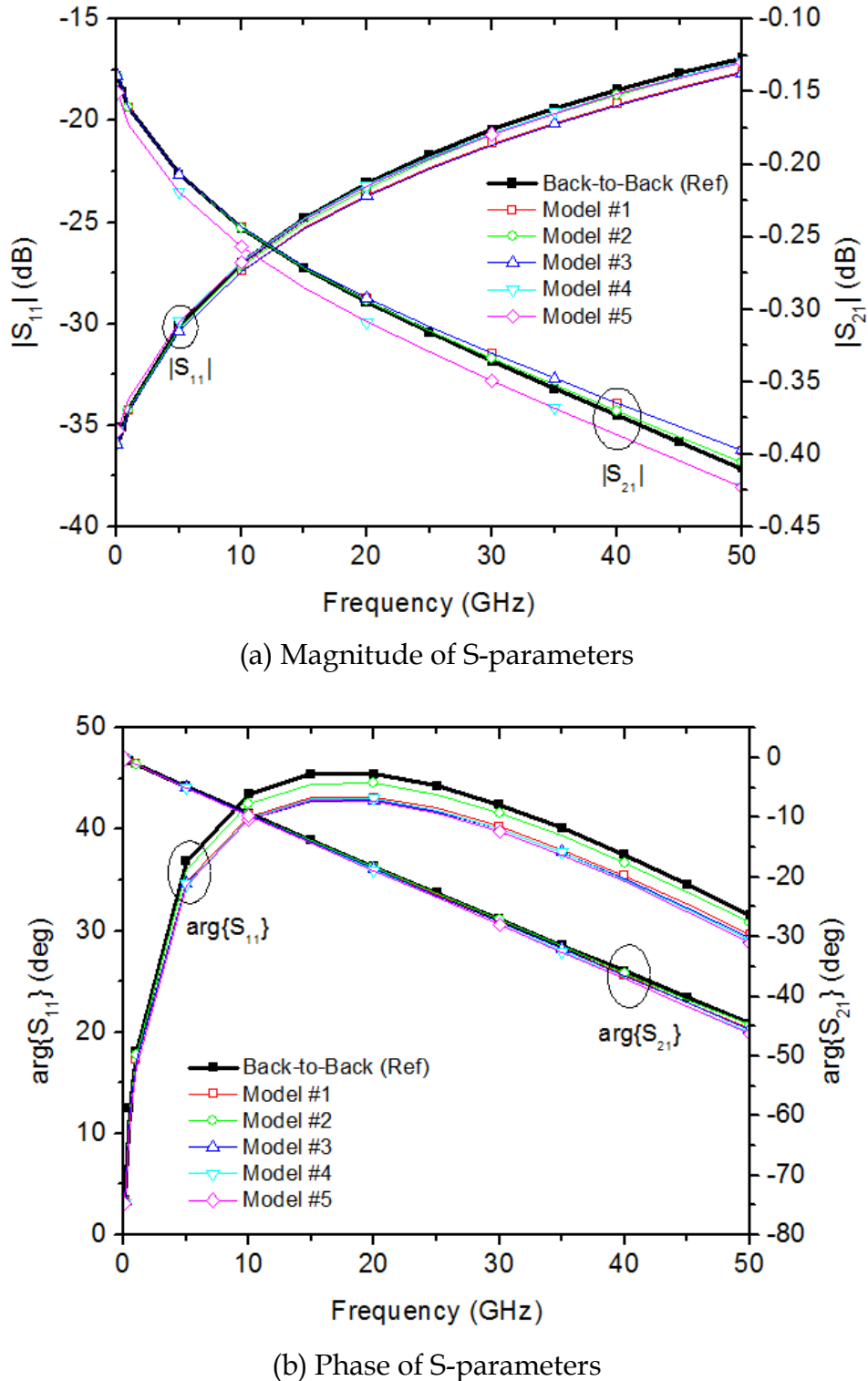


Fig. A.5 Comparison between simulated S-parameters of the CPW configuration in Fig. A.4 (Back-to-Back) and the CPW configurations where the back-to-back CPW lines are replaced by the geometries from in Fig. A.3.

APPENDIX B

GAP CAPACITANCE IN CIRCUIT MODELS

Circuit models in Chapter 2 include a gap capacitance, C_{gap} , although a CPW gap component is provided in AWR library. This appendix shows the difference between the gap capacitance and the CPW gap component. Effects of the gap capacitance on S-parameter responses are also demonstrated for high impedance devices, i.e. the device with 100 nm diameter Pt NWs.

B.1 Comparison Between Gap Capacitance and CPW Gap Component

An empty device can be modeled using a CPW gap component provided in AWR library, as shown in Fig. B.1 (a). Alternatively, the empty device can be modeled with a gap capacitance between the tapered sections, as shown in Fig. B.1 (b). This approach originates from the fact that there is coupling between the two tapered sections through the gap and a small amount of power is transferred from one port to the other. The value of C_{gap} , a static capacitance, can be estimated from the dimensions used to create the gap (gap distance, cross-sectional area of the taper ends, and material properties). As given in Section 2.2.2, computed C_{gap} is 5.3 aF. Due to the stray fields

from the top and bottom surfaces of a tapered line, as verified in full-wave simulations, the used value in modeling is 0.6 fF. This value is obtained from tuning the circuit model to fit the full-wave data.

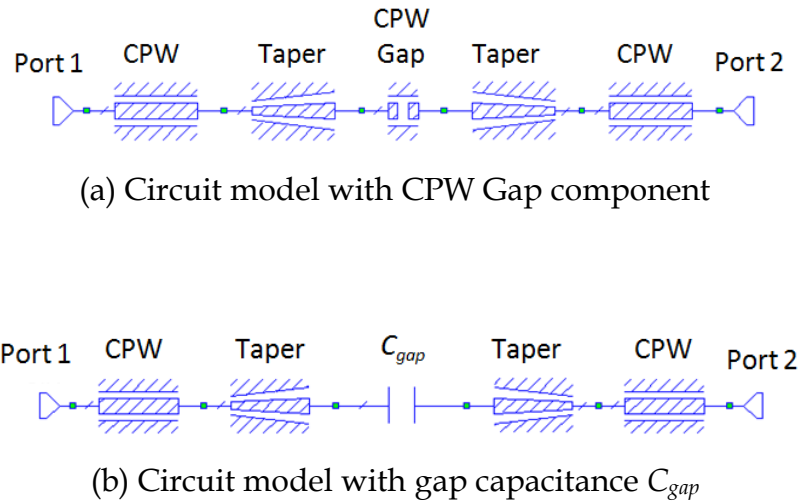


Fig. B.1 Circuit modes for empty devices (neither NW nor Au-bridge).

Simulated S-parameters for both models in Fig. B.1 are compared with measurements in Fig. B.2. As seen, their $|S_{21}|$ responses have about 11 dB difference over the whole frequency range. Circuit models are an approximation based on characteristics from one end to the other for each component (for two-port components), thus effects of the stray fields are not counted. This result shows that the modified circuit model with the gap capacitance (Fig. B.1 (b)) is more appropriate than the model based on physical dimensions (Fig. B.1 (a)) for small devices.

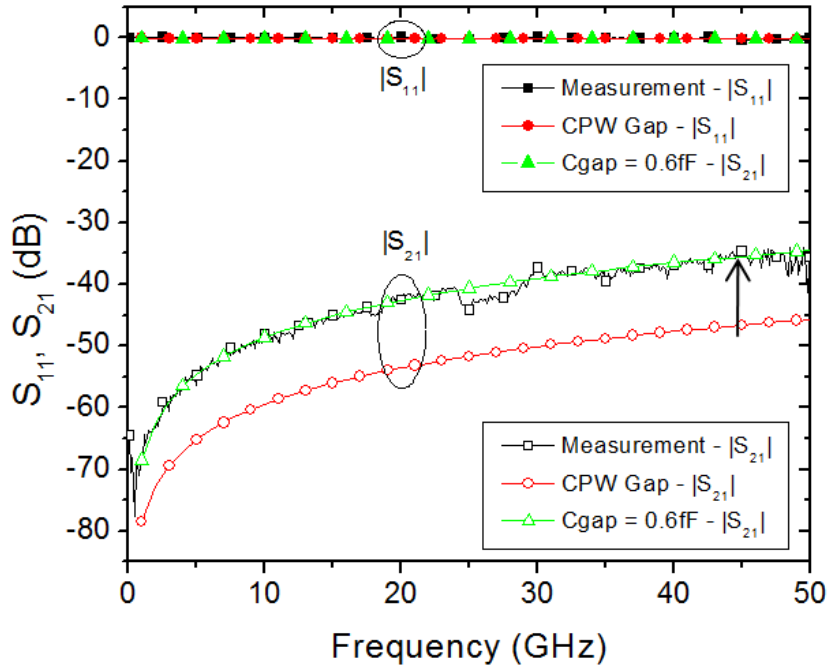


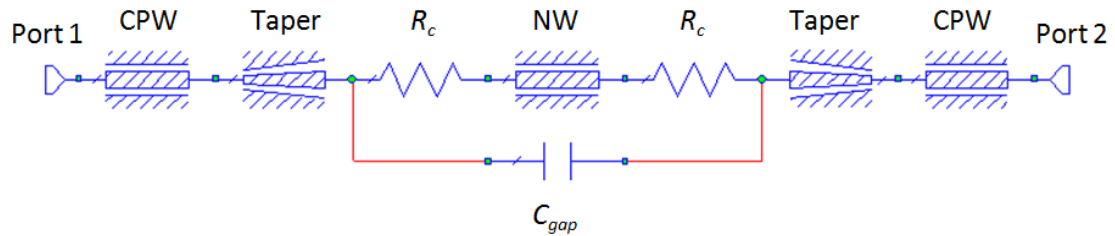
Fig. B.2 Measured and simulated S-parameters for empty devices. The devices are modeled with CPW gap component (CPW Gap in legend) and gap capacitance of 0.6 fF (Cgap = 0.6 fF in legend).

B.2 Verification with Devices Having Pt NWs

As mentioned in Section 2.2.2, the gap capacitance plays a significant role for high impedance devices. The effect of the gap capacitance can be clearly observed from simulated results for the device with 100 nm diameter Pt NWs, circuit models of which are shown in Fig. B.3. Two models are compared here: a circuit model without a gap capacitance (Fig. B.3 (a)) and a circuit model with the gap capacitance (Fig. B.3 (b)). The value of the gap capacitance is kept to be 0.6 fF. Contact resistance, R_c , of 2400 Ω is included in the models.



(a) Circuit model without gap capacitance



(b) Circuit model with gap capacitance

Fig. B.3 Circuit models for the device with 100 nm diameter Pt NWs.

Simulated S-parameters for the two models are compared with measurements in Fig. B.4. As seen, the $|S_{11}|$ responses look similar to each other. The $|S_{21}|$ of the model with the gap capacitance correlates well with measurements. Note that difference between the model with and without the gap capacitance is clearly observed in the high frequency range for $|S_{21}|$. This difference cannot be seen from the results for the device with 250 nm diameter Pt NWs (total resistance of two contact resistances and NW's resistance is about 600-700 Ω , see Table 2.1), meaning that the gap capacitance influences high impedance devices.

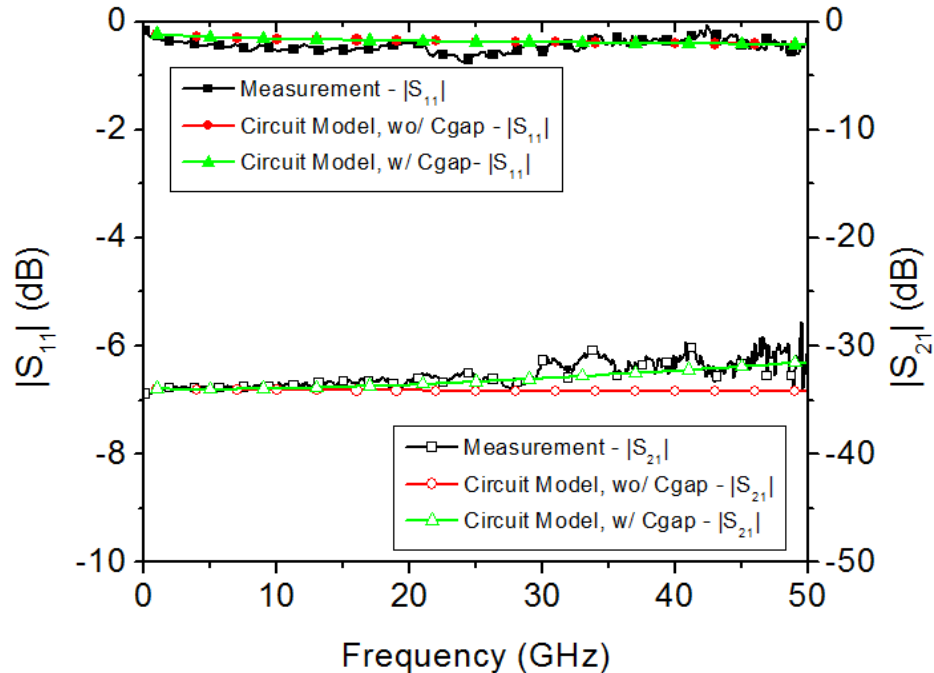


Fig. B.4 Measured and simulated S-parameters for the device with 100 nm diameter Pt NWs. The model without the gap capacitance (wo/ Cgap in legend) and that with the gap capacitance (w/ Cgap in legend) shown in Fig. B.3. are compared to verify effects of the gap capacitance for high impedance devices.

APPENDIX C

ELEMENTAL ANALYSIS RESULTS

Elemental analysis is performed by an Energy Dispersive X-ray Spectroscopy (EDS). The EDS is a chemical analysis technique used in conjunction with SEM for characterizing the elemental composition of the sample under test [1]. When the sample is bombarded by the electron beam of the SEM, electrons are ejected from the atoms comprising the sample. The resulting electron vacancies are then filled by electrons from a higher energy state, and an x-ray is emitted corresponding to the energy difference between the two electron's states. The emitted x-ray is detected to characterize the element of the sample.

The SiO₂ dielectric deposited on a Ni substrate is examined by the EDS technique for several different conditions of FIB energy from 5 kV to 20 kV in 5 kV steps. Obtained results are summarized below.

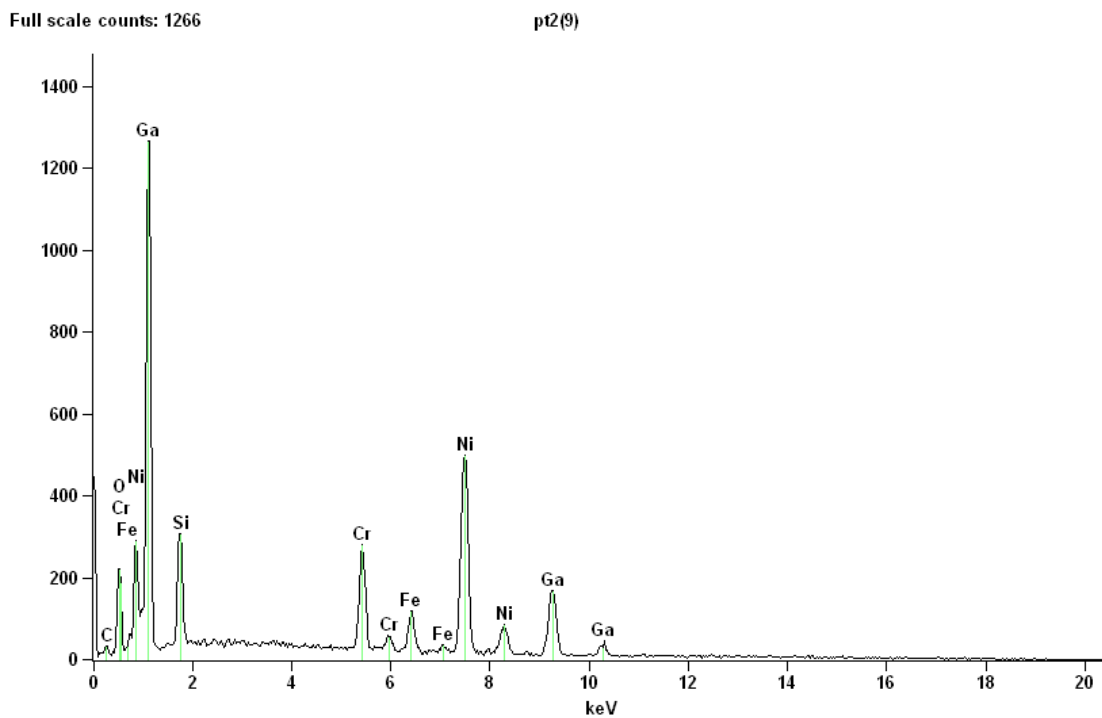


Fig. C.1 Elemental analysis spectrum for FIB SiO₂ at 20 kV.

Table C.1 Elemental analysis result for FIB SiO₂ at 20 kV.

Element Line	Net Counts	Weight %	Atom %
C K	163	10.05	28.38
O K	1672	12.12	25.67
Si K	2404	4.45	5.38
Si L	0	---	---
Cr K	3499	8.15	5.31
Cr L	0	---	---
Fe K	1479	4.31	2.62
Fe L	0	---	---
Ni K	8024	33.17	19.15
Ni L	2133	---	---
Ga K	3059	27.75	13.49
Ga L	10431	---	---
<i>Total</i>		100.00	100.00

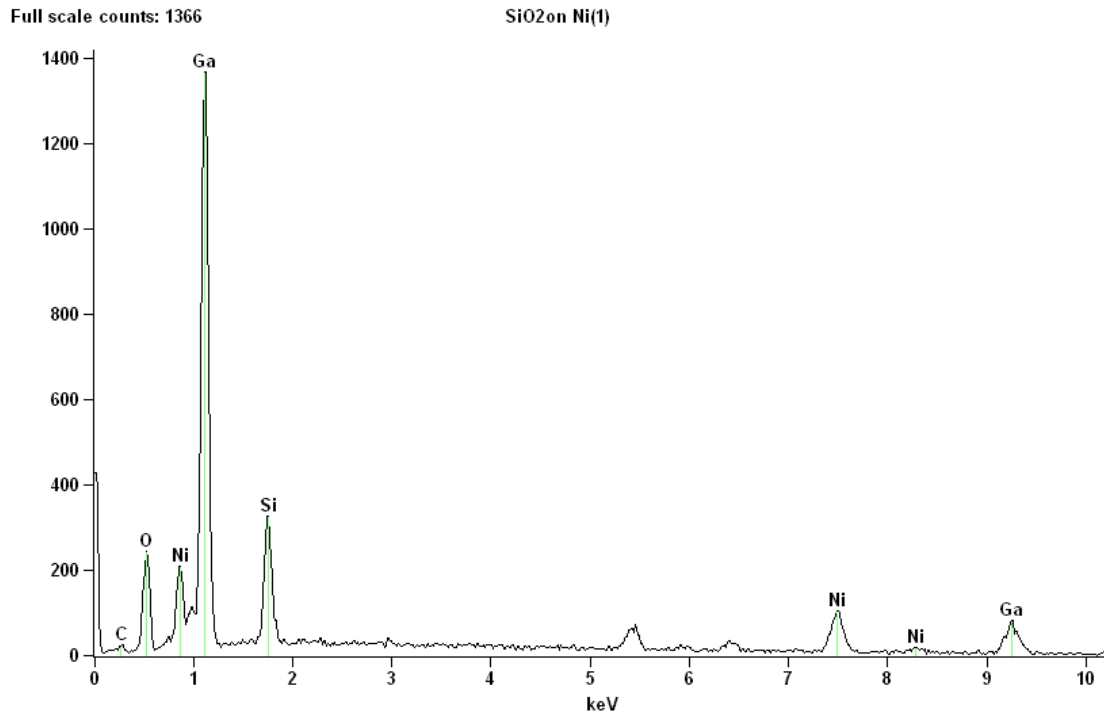


Fig. C.2 Elemental analysis spectrum for FIB SiO₂ at 15 kV.

Table C.2 Elemental analysis result for FIB SiO₂ at 15 kV.

Element Line	Net Counts	Weight %	Atom %
C K	61	4.20	14.14
O K	1593	11.98	30.32
Si K	2307	5.90	8.50
Si L	0	---	---
Ni K	1499	16.62	11.46
Ni L	1522	---	---
Ga K	1180	---	---
Ga L	10591	61.31	35.59
Total		100.00	100.00

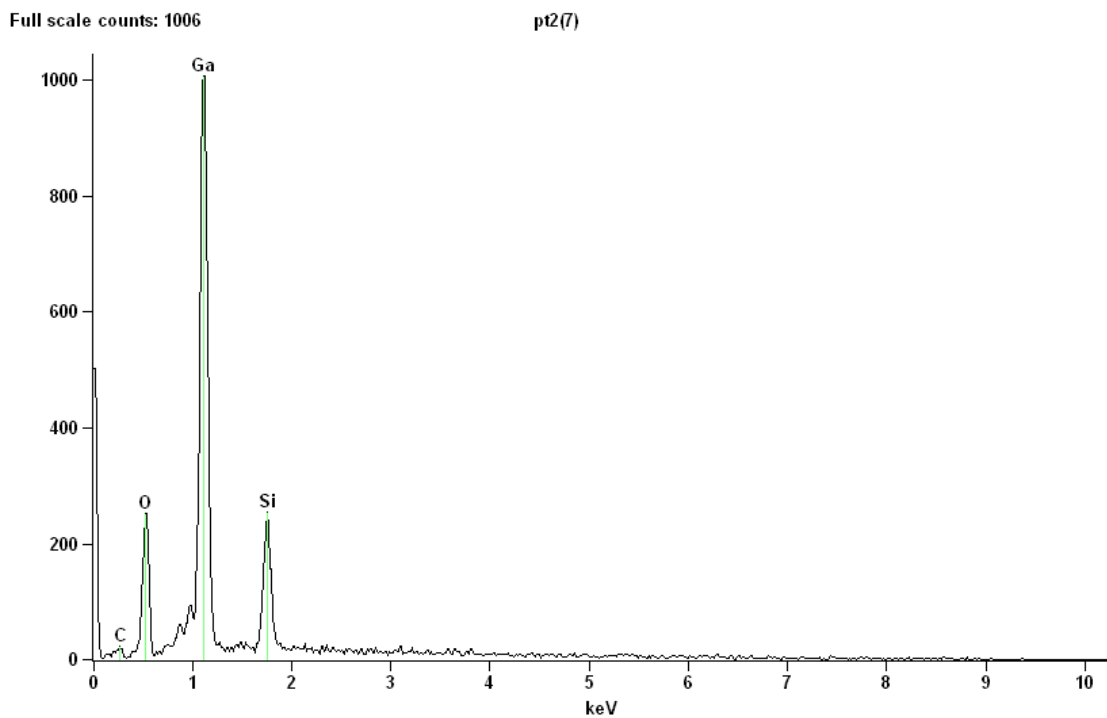


Fig. C.3 Elemental analysis spectrum for FIB SiO₂ at 10 kV.

Table C.3 Elemental analysis result for FIB SiO₂ at 10 kV.

Element Line	Net Counts	Weight %	Atom %
C K	86	6.08	17.84
O K	1637	16.54	36.43
Si K	1853	8.83	11.08
Si L	0	---	---
Ga K	0	---	---
Ga L	8012	68.54	34.64
Total		100.00	100.00

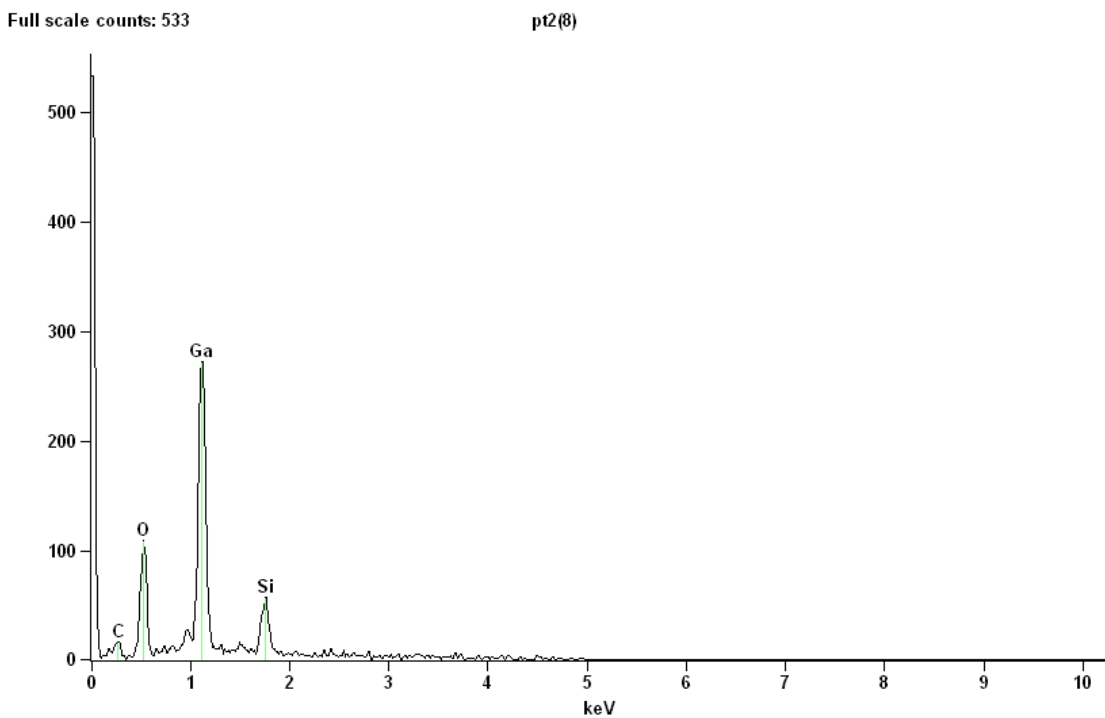


Fig. C.4 Elemental analysis spectrum for FIB SiO₂ at 5 kV.

Table C.4 Elemental analysis result for FIB SiO₂ at 5 kV.

Element Line	Net Counts	Weight %	Atom %
C K	97	7.38	21.68
O K	699	14.79	32.63
Si K	381	8.39	10.54
Si L	0	---	---
Ga L	2063	69.43	35.14
<i>Total</i>		100.00	100.00

References

- [1] Materials Evaluation and Engineering, Inc. *The Handbook of analytical methods for materials*. Available: <http://mee-inc.com/hamm.html>.